SEA SURFACE TEMPERATURE

VISIBLE/INFRARED IMAGER/RADIOMETER SUITE ALGORITHM THEORETICAL BASIS DOCUMENT

Version 3: May 2000

Yimin Ji
Philip E. Ardanuy
Donglian Sun
Shawn Miller
Quanhua Liu
Wenli Yang

William Emery, Science Team Member
University of Colorado

RAYTHEON SYSTEMS COMPANY
Information Technology and Scientific Services
4400 Forbes Boulevard
Lanham, MD 20706

SBRS Document #: Y2386

EDR: SEA SURFACE TEMPERATURE

Doc No: Y2386

Version: 3

Revision: 0

	FUNCTION	NAME	SIGNATURE	DATE
Prepared By	EDR Developer	YIMIN JI		
Approved By	Relevant IPT Lead	YIMIN JI		
Approved By	Chief Scientist	P. ARDANUY		
Released By	Program Manager	H. BLOOM		

TABLE OF CONTENTS

Raytheon

LIST OF FIGURES

Raytheon

Raytheon

LIST OF TABLES

Raytheon

GLOSSARY OF ACRONYMS

ATSR   Along Track Scanning Radiometer

AVHRR   Advanced Very High Resolution Radiometer

CMIS   Conical Scanning Microwave Imager/Sounder

CrIS   Cross-track Infrared Sounder

ECMWF   European Center for Medium-Range Weather Forecast

EDR   Environmental Data Record

EOS   Edge of Scan

GLI   Global Imager

IFOV   Instantaneous Field of View

IPO   Integrated Program Office

IR   Infrared

LOWTRAN   Low-resolution Transmission Model

MCSST   Multi-Channel Regression Method SST

MODIS   Moderate Resolution Imaging Spectroradiometer

MODTRAN   Moderate Resolution Transmission Model

NCEP   National Centers for Environment Prediction

NEDT   Noise-Equivalent Temperature Difference

NPOESS   National Polar-orbiting Operational Environmental Satellite System

OCTS   Ocean Color and Temperature Scanner

RMS   Root mean square

SBRS   Santa Barbara Remote Sensing

SST   Sea Surface Temperature

TOA   Top of the Atmosphere

TOVS   TIROS Operational Vertical Sounder

VIIRS   Visible/Infrared Imager/Radiometer Suite

ABSTRACT

This is the algorithm theoretical basis document (ATBD) for sea surface temperature (SST) retrieval from infrared (IR) signals received by the National Polar-orbiting Operational Environmental Satellite System (NPOESS) Visible/Infrared Imager/Radiometer Suite (VIIRS). SST is a VIIRS level 2 product and an input variable for other VIIRS products such as ocean currents and net heat flux.

This document describes the theoretical basis and development process of the SST algorithms, which are being developed by the NPOESS algorithm team. Two basic algorithms are discussed and evaluated in this document.

1. Atmospheric water vapor correction algorithm. This algorithm uses two or more IR-bands in atmospheric window to correct water vapor and is a heritage algorithm of AVHRR, ATSR, and MODIS. However, the VIIRS baseline algorithm combines a dual split window (3.75, 4.00, 10.8, and 12 μm) measurement to retrieve skin SST in both daytime and nighttime. The algorithm includes satellite zenith angle correction and solar correction in daytime. Currently, a high resolution radiative transfer model, historical *in situ* skin SST and atmosphere profiles are used to derive coefficients for SST calculations. The results from VIIRS testbed indicate a successful solar correction in the daytime by using a split window in mid-IR window. The SST precision in both daytime and nighttime is improved to 0.30 K from 0.5 K by using a split window in mid-IR window and a split window in far-IR window compared to the existing methods that use only LWIR bands in daytime. The SST precision of VIIRS baseline algorithm is further improved to 0.25 K by an air mass classification technique.

2. Physical retrieval: The straightforward physical method is to invert skin SSTs from VIIRS TOA radiances using a radiative transfer model. This is a highly promising method to obtain better precision, but it is limited by the operational processing time requirements. The best precision of physical retrial under perfect sensor is 0.09 K after 8 iterations.

The VIIRS SST Environmental Data Record (EDR) requires a horizontal cell size of 1 km with 0.2 K measurement accuracy and 0.5 K measurement uncertainty, which yields a precision requirement of about 0.45 K. The major error sources for VIIRS SST retrievals are atmospheric corrections and VIIRS sensor performances. Three different data sets and various algorithms were used in the VIIRS test bed to estimate the uncertainty, accuracy, and precision of VIIRS SST retrieval. These evaluations are essential to the evolution of VIIRS sensor design and algorithm design.

The results showed that the precision due to atmospheric correction is 0.3 K for a 2-band water vapor correction algorithm and 0.2 K for a 4-band algorithm. Given the VIIRS radiometer noise for IR bands, the test bed results showed a 0.45 K precision for the two-band method and a 0.3 K precision for the duel split window method.

The 0.2 K accuracy requires a calibration error less than 0.4 percent. This will require a highly qualified on-board calibration system. This document discusses the calibration issue and presents

preliminary results using various data sources. The testbed results indicated that the VIIRS sensor design has the capability to achieve the calibration requirement.

The corrections for aerosol and thin cirrus clouds, and conversions from skin SST to bulk SST, are also discussed. The presence of aerosol and thin cirrus contributes significant errors in the SST retrieval. However, after using correction algorithm, these errors can be reduced to less than 0.1 K. VIIRS aerosol and cloud products will contribute to the SST corrections.

Calibration and algorithm validation are the two keys to ensuring quality performance of the algorithm. Both pre-launch and post-launch activities are discussed in this document. The performance of the VIIRS SST algorithm will be strongly dependent on the establishment of the match-up database.

Constraints, limitations, and assumptions are discussed in this document. Major constraints for the surface temperature algorithms are instrument band selection, instrument NEDT for each band, instrument calibration, and the availability and quality of the surface calibration/validation observations.

1.0 INTRODUCTION

1.1 PURPOSE

This document identifies sources of input data and describes the theoretical basis and development process of the SST algorithm. Algorithm validation, algorithm sensitivity, constraints, limitations, and assumptions are also discussed.

1.2 SCOPE

The SST algorithms described in this document will be used routinely to retrieve both skin and bulk SSTs from VIIRS measurements. Future development efforts may result in modifications to the current operational algorithms.

The next section provides a brief overview. Descriptions of the algorithm and the development process are presented in Section 3, along with discussions of algorithm sensitivity to various physical parameters. Calibration and validation are also discussed in Section 3. Constraints, assumptions, and limitations are identified in Section 4.

1.3 VIIRS DOCUMENTS

Reference to VIIRS documents will be indicated by a number in italicized brackets, e.g., *[V-1]*.

[V-1] VIIRS Sensor Requirements Document, NPOESS IPO.

1.4 REVISIONS

This is the third version of the document, dated May 2000. The first version was dated October 1998.

2.0   EXPERIMENT OVERVIEW

2.1   OBJECTIVES OF SEA SURFACE TEMPERATURE RETRIEVALS

With about 70 percent of the Earth's surface covered by ocean, the variability of sea surface temperatures has a significant socio-economic impact. For example, slow variations of SST over the tropics and subtropics can substantially change the planetary atmospheric flow and are the dominant factors in global and regional climate changes. Variations of SSTs of less than 1 K can occur anywhere over the ocean. However, variations greater than 1 K over a large area usually occur only during El Niño events. In some El Niño events, the SST over the eastern equatorial Pacific may be 4-5 K higher than the climate mean. SST is also a good indicator of global warming. However, ground truth data over the vast oceans are limited. Therefore, satellite-based SST measurements combined with ground truth data have been the major source of high resolution SST data (Reynolds, 1988; Reynolds and Smith, 1994). Currently, the 14 km resolution weekly merged SSTs are used for operational weather forecasting in North America. Weekly merged SST products have also been used in climate simulations to understand the mechanisms of interannual and intraseasonal climate variability over Asia and America (e.g., Ji and Vernekar, 1997).

The accuracy of satellite SST determination has improved significantly since the development of radiometers with two or more atmospheric window channels within mid-IR and far-IR windows (e.g., McClain *et al*., 1983). The fundamental basis of multi-channel SST algorithms is the differential water vapor absorption in the various atmospheric window regions of the spectrum. The current satellite multi-channel SST algorithm can permit global SST retrievals on space scales of 8 km with a root mean square error < 0.7 K (McClain *et al*., 1985; Barton *et al*., 1993; Legeckis and Zhu, 1997; and May *et al*., 1998). The Moderate Resolution Imaging Spectroradiometer (MODIS) measurement accuracy requirement for SST is 0.35 K (Brown and Monnett, 1996). The current operational MCSST and the proposed MODIS SST algorithms are statistical methods. These methods, which combine the satellite observation and *in situ* observation, have proven to be very successful in producing reliable global SST data sets. The current operational SST retrieval methods are based on two windows within the 10-13 micrometer interval in the daytime and an additional window within the 3.5-4.2 micrometer interval in the nighttime. Some research studies also used water vapor information in the statistical method (e.g., Emery *et al*., 1993). Although physical retrievals have not been used for operational SST retrieval due to the large computational requirement and possible instability, they are promising methods for improving the retrieval precision. Physical retrievals need at least three bands to obtain sufficient information for the forward model.

Although it is widely accepted that satellite infrared (IR) sensors measure radiance from only the skin of the ocean, oceanographers are more interested in SSTs for the upper meters of the oceans, commonly referred to as bulk temperature (Schluessel *et al*., 1990). This interest in the bulk temperature has led to the practice of calibrating satellite-derived SSTs with *in situ* bulk SST measured by ocean buoys. The difference between skin and bulk temperatures contributes an added level of uncertainty to the satellite SST retrieval. The relationship between skin and bulk SSTs has been investigated by a number of scientists (e. g., Schluessel *et al*., 1990). Currently, the Advanced Very High Resolution Radiometer (AVHRR) SST is calibrated to bulk SST, while

the Along Track Scanning Radiometer (ATSR) measures the skin temperature (Zavody *et al.*, 1994). MODIS SST retrieval will be a follow-up to AVHRR SST algorithm (Brown, 1996).

The ATSR retrieval method is a physically based regression method. This method uses a line-by-line model to simulate the ATSR TOA radiances and incorporates *in situ* skin SSTs with the simulated radiances. This method requires accurate models and highly qualified on-board calibration, as well as very low sensor noise.

The overall scientific objective of the VIIRS SST retrievals is to provide improved measurements of both skin and bulk SST fields by using statistical and physical methods. The VIIRS SST EDR requires a global horizontal cell size of 3 km and a regional horizontal cell size of 1.3 km, with a 0.2 K measurement accuracy and a 0.5 K measurement uncertainty. These requirements exceed state-of-the-art operational results. However, these are minimum requirements from an environmental point of view. For example, a few tenths of a degree increase in global SST in a decade reflects a strong global warming trend. Over tropical oceans, atmospheric convective activities are sensitive to a small change of SSTs. The goal of VIIRS SST retrieval is to provide weekly global SST fields with 1 km horizontal resolution.

2.2 INSTRUMENT CHARACTERISTICS

The VIIRS sensor is based on the NPOESS sensor requirements and on EDR thresholds and objectives. Therefore, the following specifications of VIIRS are used only in the current version of retrieval algorithms and are subject to changes during the flowdown process.

The VIIRS mid-IR and far-IR bands must be positioned to optimize their use for SST determination. Bands in the far-IR are usually located near the maximum Earth radiance. Influences of ozone and other atmospheric absorbers must be avoided. Figure 1 shows the MODTRAN simulated radiance at the height of the satellite for the thermal infrared spectrum. There are two suitable regions for far-IR band selection: 8-9 micrometers and 10-13 micrometers. VIIRS two far-IR bands will be located in these two regions. Bands in the mid-infrared are usually located where the atmosphere is most transparent. Figure 2 shows the MODTRAN simulated atmospheric transmittance for five standard atmospheres. It shows that the 3.4-4.2 micrometer region is the most transparent atmospheric window. Two VIIRS bands will be located in this window.
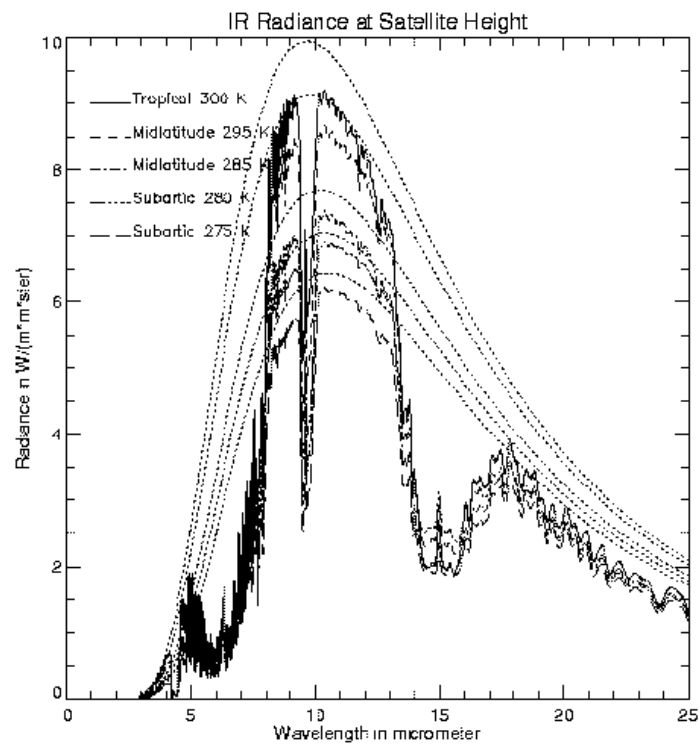
Figure 1. IR radiance at satellite height for five standard atmospheres simulated by MODTRAN.
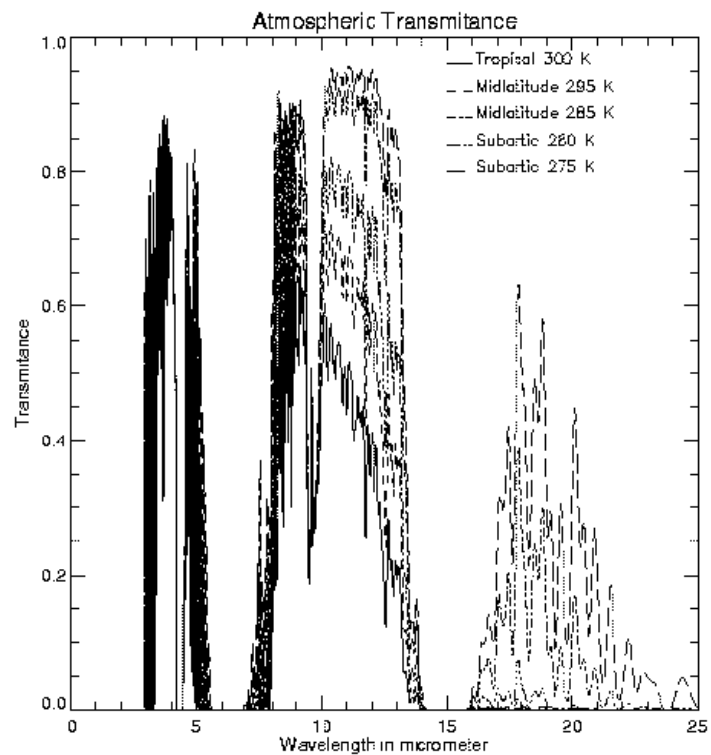
Figure 2. Atmospheric transmittances for five atmospheres.

The continuity requirement on SST derivation is also one of the factors for VIIRS band selection. Table 1 shows the bands chosen to retrieve SST for existing or proposed satellites.

Table 1. Channel Characteristics of Satellite-borne Infrared Radiometers.

VIIRS baseline		MODIS		AVHRR		ATSR		OCTS		GLI	
$\lambda \mu m$	NEDT K	$\lambda \mu m$	NEDT K	$\lambda \mu m$	NEDT K	$\lambda \mu m$	NEDT K	$\lambda \mu m$	NEDT K	$\lambda \mu m$	NEDT K
3.700	0.065	3.75	0.05	3.75	0.12	3.7	0.019	3.7	0.15	3.715	<0.15
4.050	0.078	3.96	0.07								
		4.02	0.07								
8.550	0.062	8.55	0.07					8.52	0.15	8.3	<0.1
10.763	0.038	11.03	0.05	10.5	0.12	10.8	0.028	10.8	0.15	10.8	<0.1
12.013	0.070	12.02	0.05	11.5	0.12	12	0.025	11.9	0.15	12	<0.1

To meet the VIIRS SST measurement requirements, the sensor must ensure very low radiometric noise for IR bands, especially the 10-12 micrometer window. Well-placed windows in the 3.6-4.2 micrometer will also be important. Table 2 shows the NEDT values for seven sensor noise models in the five bands. These specifications have been used to derive the final sensor design. The detailed specification of the current version of the sensor design are listed in Table 3.

Table 2. NEDT Values in Five IR Bands for Seven Sensor Noise Models

λ (μm)	$\Delta \lambda$ (μm)	NEDT(K at 300 K)/Aperture Diameter (cm)						
		Model 1 29 cm	Model 2 24 cm	Model 3 19 cm	Model 4 14 cm	Model 5 9 cm	Model 6 4 cm	Model 7 1 cm
3.700	0.180	0.12	0.14	0.18	0.26	0.47	1.71	18.31
4.050	0.155	0.10	0.12	0.15	0.22	0.38	1.31	14.50
8.55	0.300	0.03	0.03	0.04	0.07	0.15	0.7	10.39
10.763	1.000	0.04	0.06	0.08	0.13	0.30	1.43	20.88
12.013	0.950	0.05	0.07	0.10	0.17	0.38	1.85	26.92

Raytheon

Table 3a. Sensor Performance for Sea Surface Temperature

Wave-length	Band Width	GSD				Ttyp	NEDT	Onboard Aggregation Factor		On ground Aggregation Factor		Effective Algorithm GSD		Effective Algorithm NEDT
		NADIR		EOS										
		Trk	Scn	Trk	Scn			Trk	Scn	Trk	Scn	Trk	Scn	
3.700	0.180	742	262	1094	617	300	0.065	1	3	4	4	2968	3144	0.009
4.050	0.155	742	262	1094	617	300	0.078	1	3	4	4	2968	3144	0.011
11	1.000	742	262	1094	617	300	0.038	1	3	4	4	2968	3144	0.005
12.013	0.950	742	262	1094	617	300	0.070	1	3	4	4	2968	3144	0.010

Table 3b. Sensor Performance for Sea Surface Temperature

Wave-length	Band Width	GSD				Ttyp	NEDT	Onboard Aggregation Factor		On ground Aggregation Factor		Effective Algorithm GSD		Effective Algorithm NEDT
		NADIR		EOS										
		Trk	Scn	Trk	Scn			Trk	Scn	Trk	Scn	Trk	Scn	
3.700	0.180	742	262	1094	617	300	0.065	1	3	1	1	742	786	0.038
4.050	0.155	742	262	1094	617	300	0.078	1	3	1	1	742	786	0.045
11	1.000	742	262	1094	617	300	0.038	1	3	1	1	742	786	0.022
12.013	0.950	742	262	1094	617	300	0.070	1	3	1	1	742	786	0.040

2.3 SST RETRIEVAL STRATEGY

Before SST retrievals can be performed within a given region, various atmospheric and surface parameters must be determined. Here, a region is defined to be an oceanic target area of an 11 by 11 pixel array. A cloud cover mask and a snow/ice mask will be used to eliminate cloud-contaminated or snow/ice-covered pixels. The SST algorithms are run only under clear sky conditions. The following sequence of SST retrieval activities is performed on all suitable pixels within a region. First, the brightness temperatures are calculated for five mid-IR and far-IR bands. Solar zenith angle will be calculated and used to determine day or night retrieval. Skin SST will be calculated using regression equations from water vapor correction algorithm. Blended SST will be calculated using regression equations from statistical retrieval.

The skin SST will then be converted to bulk SST through the application of robust skin-bulk conversion models. The physical retrieval will utilize CMIS or CrIS atmospheric profiles. The skin-bulk conversion and physical retrieval may not be considered as operational methods at this time.

3.0   ALGORITHM DESCRIPTION

3.1   PROCESSING OUTLINE

There are two retrieval methods for sea surface temperature. The water vapor correction method is assisted initially by the establishment of global ancillary data sets and radiative transfer models. The coefficients are obtained through one time simulations and validated using ground observations. Figure 3 depicts the processing concept for SST retrieval. Figure 4 displays the current flowchart for physical retrieval. The flow charts for statistical skin SST retrieval and blended SST retrieval are similar to Figure 3 except that the coefficients are different and that the skin-bulk conversions are unnecessary for blended SST.
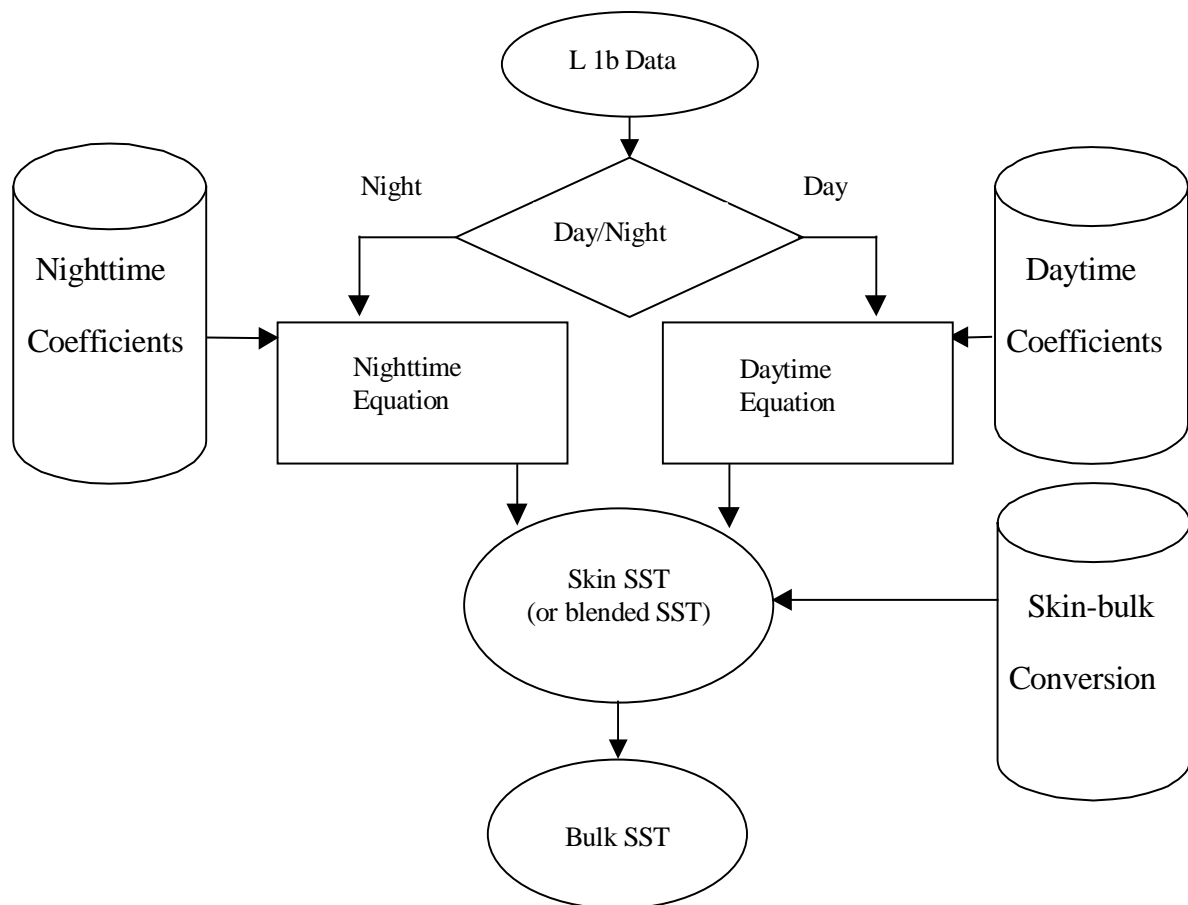
Figure 3. SST high level flowchart: Statistical Method.
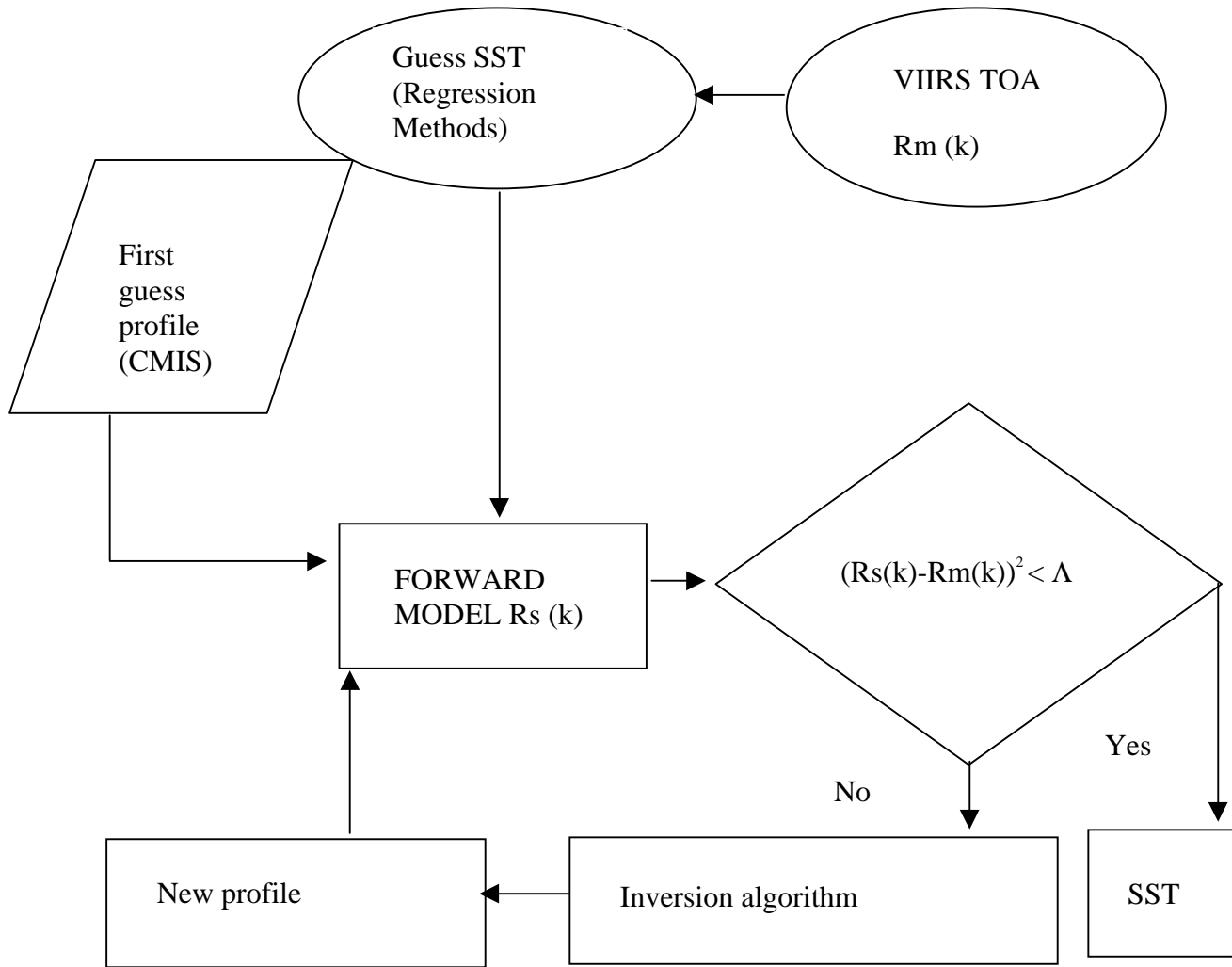
Figure 4. SST high level flowchart: Physical Retrieval.

3.2 ALGORITHM INPUT

3.2.1 VIIRS Data

Required inputs necessary for the SST retrieval from the VIIRS data stream are cloud mask, snow/ice mask, Level 1b brightness temperature, cloud optical thickness, and aerosol optical thickness and aerosol types.

3.2.2 Non-VIIRS Data

Non-VIIRS ancillary data includes land/ocean mask, observed skin and bulk SSTs, CMIS, and CrIS atmospheric profiles.

3.3 THEORETICAL DESCRIPTION OF SST RETRIEVAL

3.3.1 Physics of the Problem

In clear sky conditions, the outgoing infrared spectral radiance at the top of atmosphere can be represented by:

$$L(\lambda,\mu) = \tau(\lambda,\mu)\varepsilon(\lambda,\mu)B(\lambda,T_s) + L_a(\lambda,\mu) + L_s(\lambda,\mu,\mu_0,\varphi_0)$$
$$+ L_d(\lambda,\mu,\mu_0,\varphi_0) + L_r(\lambda,\mu,\mu_0,\varphi_0) \tag{1}$$

Where τ is the transmissivity, ε the surface spectral emissivity, B the Plank function, L_a the thermal path radiance, L_s the path radiance resulting from scattering of solar radiation. L_d is the solar radiance and L_r the solar diffuse radiation and atmospheric thermal radiation reflected by the surface. λ is the wavelength. $\mu = \cos(\theta)$, $\mu_o = \cos(\psi)$, where θ is the satellite zenith angle, ψ the solar zenith angle. φ_o is azimuth angle.

The wavelength is the wavelength center of a narrow interval because there is no way to measure the exact monochromatic signal as a continuous function of wavelength by satellite sensors. Equation 1 can be used in the 3-14 *μm* range. It requires complete calculations of the atmospheric radiative transfer to determine the values of all terms on the right side. This equation has been used in many atmospheric radiation models including LOWTRAN (Kneizys *et al*., 1983), MODTRAN (Berk *et al*., 1987), and MOSART (Cornette *et al*., 1994). The inversion of Equation 1 is not easy if the atmospheric conditions are unknown. In our physical retrieval method, we must either use the historical data, or the CrIS and CMIS profiles as first guesses. The accuracy of the inversion will depend on the number of interactions. The physical retrieval will be discussed in Section 3.3.2.

In order to infer the surface information, we should choose window channels with no or little atmospheric contribution. As shown in Figure 1, the wavelength between 3.5–4.2 micron, 8–9 micron, and 10–13 micron are some typical atmospheric windows. For a perfect window, the total atmospheric transmittance $\tau_0(\lambda \ \mu)$ should be 1.0, the transmittance weighting function should be 0. However, as indicated in Figure 2, the transmittances at these windows are not 1.0 and are functions of atmospheric profiles. The main absorber for these windows is atmospheric water vapor.

In order to evaluate the water vapor contribution to various window channels, simulations were performed using 5139 profiles offered by the IPO (Integrated Program Office) over sea surface under clear sky conditions with MODTRAN 3.7. The following five window bands are simulated: 3.75 μm, 10.8 μm (AVHRR channel 4), 12 μm (AVHRR channel 5), and two new VIIRS bands, 4.005 μm and 8.55 μm. Figure 5a shows the water vapor as a function of SST derived from these profiles. It shows that the atmospheric water vapors are concentrated over warmer SST above 285K.

Figure 5b shows transmittance as a function of surface skin temperature. It indicates that the transmittances decrease significantly for 10.8 and 12 μm, as well as 8.55 μm channels as SST becoming warmer (285–310 K). Which explains why most existing split window algorithms

using only 11 and 12 μm channels have larger errors at the warmer temperature above 285K. The transmittances for the Shortwave Infrared (SWIR) channels, 3.75 μm and 4.005 μm, are less sensitive to the surface skin temperature and are closer to 1.0 compared to those of LWIR channels. From this aspect, SWIR 3.75 μm and 4.005 μm channels are better window channels than the LWIR 11, 12, and 8.55 micron channels. The most stable channel is 4.005 microns. Figure 5c shows the transmittance vs. precipitable water distribution, it shows that the transmittance at the 4.005 micron channel changes very little with the column water vapor amount. While the transmittance at 3.75 micron channel has a linear relationship with the precipitable water, the transmittances at 11, 12, and 8.55 microns decrease significantly as the water vapor increases and the relationship is also not linear. These results suggest that the SWIR window channels be needed to retrieve warmer surface temperatures.
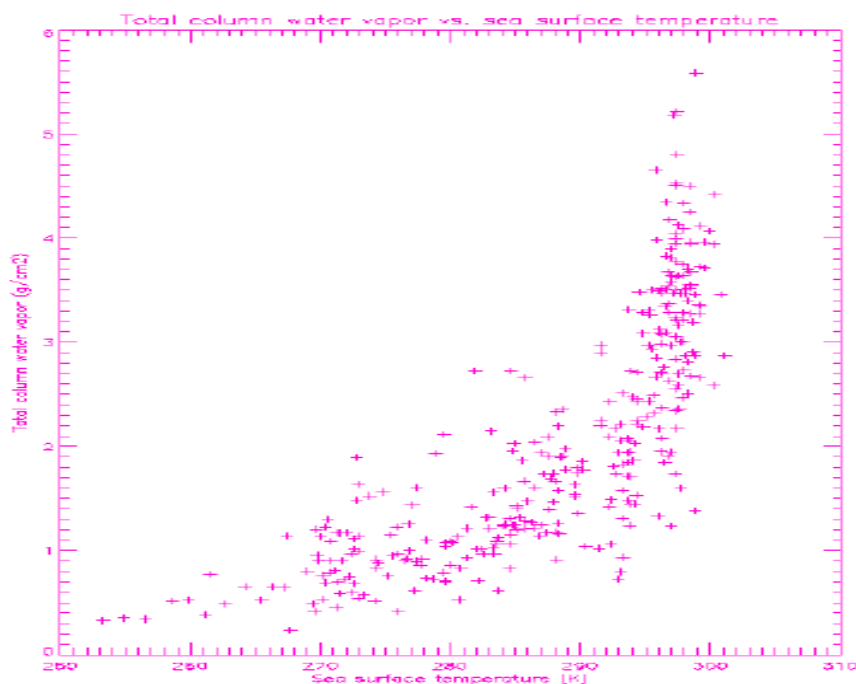
Figure 5a. Water vapor vs. sea surface temperature distribution.

Raytheon
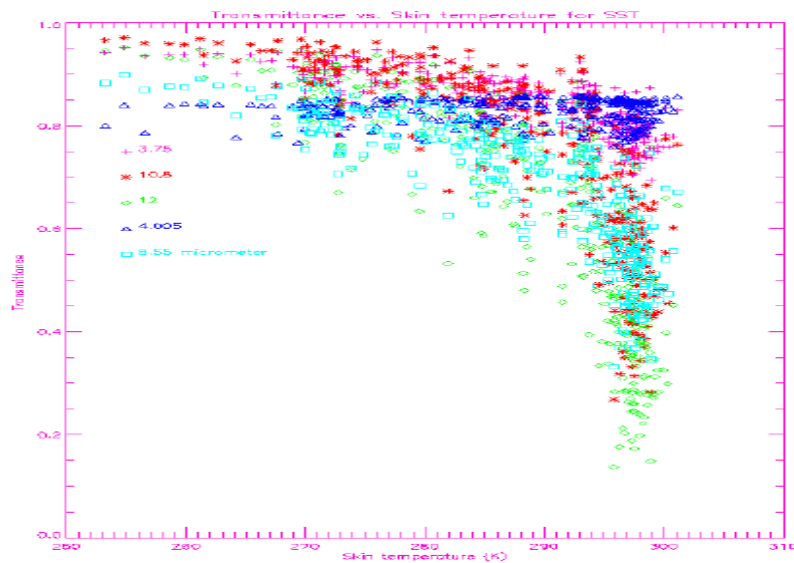
Figure 5b. Transmittance vs. SST.
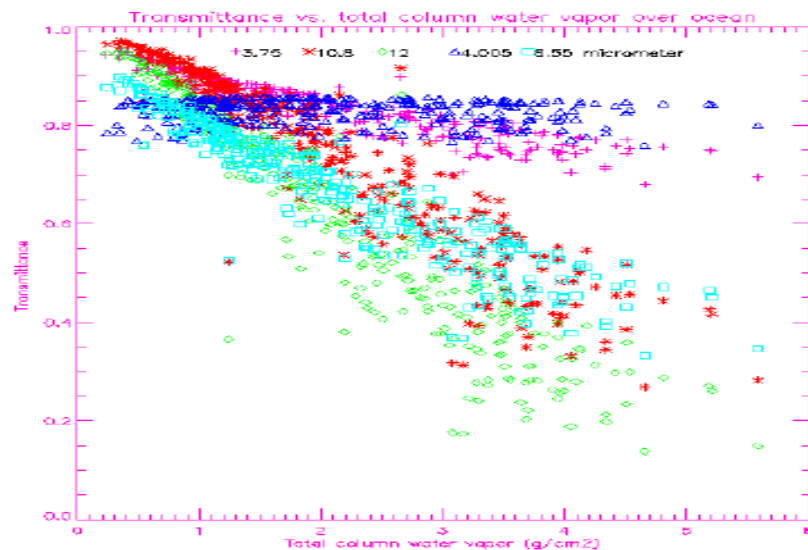
Figure 5c. Transmittance vs. total column water vapor over ocean.

However, as shown in Figure 5d, the temperature deficits (T_s-T_b) at IR window channels 11, 12, and 8.55 microns are very stable, while the surface temperature can be much lower than the brightness temperature at SWIR channels 3.75 and 4.005 microns in daytime, sometimes by more than 10 degrees. This is because in the daytime, the SWIR channel contains both reflected solar radiation and radiation emitted by the surface and the atmosphere. Therefore, the solar contamination on SWIR channels must be corrected. The solar correction can be done only under the condition that two or more SWIR bands are existing.
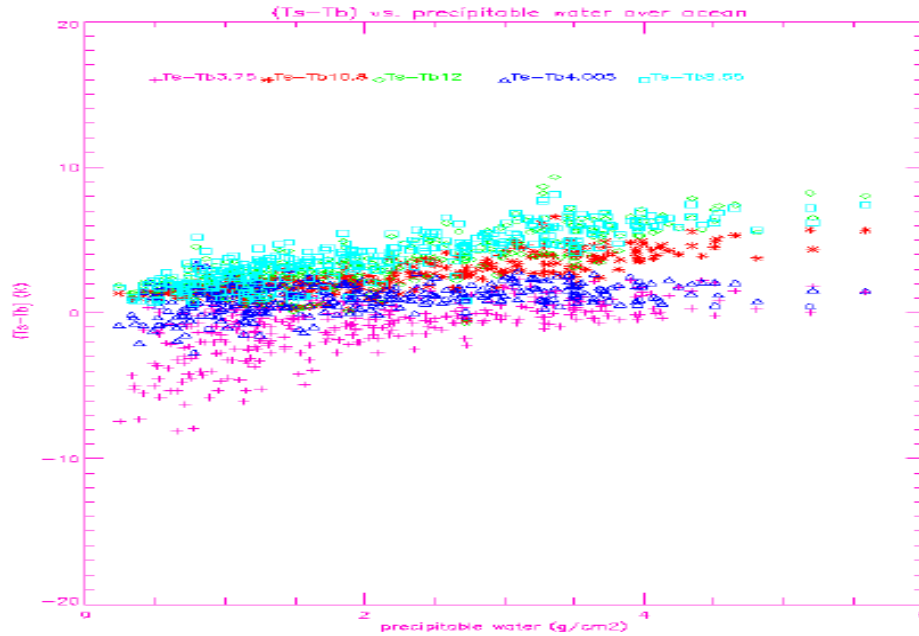
Figure 5d. Temperature deficits (T_s-T_b) vs. total column water vapor distribution.

It has been noted that satellite infrared radiance can be corrected straightforwardly for atmospheric absorption in the atmospheric window spectrum by utilizing a split window technique. In the following discussion, we outline a theoretical basis for the split window method. In the far-IR window, this method can be extended to multi-band methods.

For far-IR bands, L_d, L_s and L_r are negligible. Therefore, only the first two terms on the right side of the above equation are important. In this case, if we ignore the change of emissivity over the ocean, the radiance error introduced by the atmosphere ΔL can be represented by:

$$
\begin{aligned}
\Delta L &= B(\lambda, T_s) - L(\lambda, \mu) = B(\lambda, T_s) - \tau(\lambda, \mu)B(\lambda, T_s) - L_a(\lambda, \mu) \\
&= - \int_1^{\tau(\lambda,\mu)} B(\lambda, T_s)d\tau(\lambda, \mu, p) + \int_1^{\tau(\lambda,\mu)} B(\lambda, T_p)d\tau(\lambda, \mu, p) \\
&= - \int_1^{\tau(\lambda,\mu)} (B(\lambda, T_s) - B(\lambda, T_p))d\tau(\lambda, \mu, p)
\end{aligned}
\tag{2}
$$

From the Planck function we find:

$$
\Delta L = \frac{\partial B}{\partial T}\Delta T = \frac{\partial B}{\partial T}(T_s - T_\lambda)
\tag{3}
$$

For an optically thin gas the following approximations can be made:

$$
d\tau = d\{\exp(-k_\lambda L)\} = k_\lambda dl
\tag{4}
$$

where k_λ is the absorption coefficient and l is the optical path-length. If we assume that the Planck function is adequately represented by a first order Taylor series expansion in each channel window, then:

$$B(\lambda, T_s) - B(\lambda, T_p) = \left.\frac{\partial B(\lambda, T_p)}{\partial T}\right|_{T_s} (T_p - T_s) \tag{5}$$

Substituting Equations 3, 4, 5 into Equation 2, we obtain:

$$T_s - T_\lambda = k_\lambda \int_1^\tau (T_s - T_p) dl \tag{6}$$

Therefore, if we pick two spectral regions of the atmosphere, we will have two linear equations with different k_λ to solve simultaneously.

For example, if we consider the two channels as $\lambda=1$ and $\lambda=2$, then we obtain:

$$T_s - T_1 = -(T_s - T_2)k_1 / k_2 \tag{7}$$

or

$$T_s - T_1 = -(T_2 - T_1)k_1 / (k_2 - k_1) \tag{8}$$

Therefore the SST can be represented as:

$$T_s = c_0 + c_1 T_1 + c_2 T_2 \tag{9}$$

In general, this can be written as:

$$T_s = C T_b \tag{10}$$

The coefficient vector **C**, which relates observed brightness temperatures to SST, is determined using regression methods by solving:

$$C = Y X^T (X X^T + kI)^{-1} \tag{11}$$

The **Y** matrix contains a large number of training SSTs and the **X** matrix contains brightness temperatures from VIIRS far-IR and mid-IR channels. In general, the **X** matrix may include nonlinear terms.

Figure 6 shows that the relationship between temperature deficits of AVHRR channel 4 and channel 5 is linear. The brightness temperatures from channel 4 are higher than those from channel 5. The differences between SST and brightness temperature are larger than 1 K and can be as large as 16 K. The large differences may be due to cirrus or aerosol.
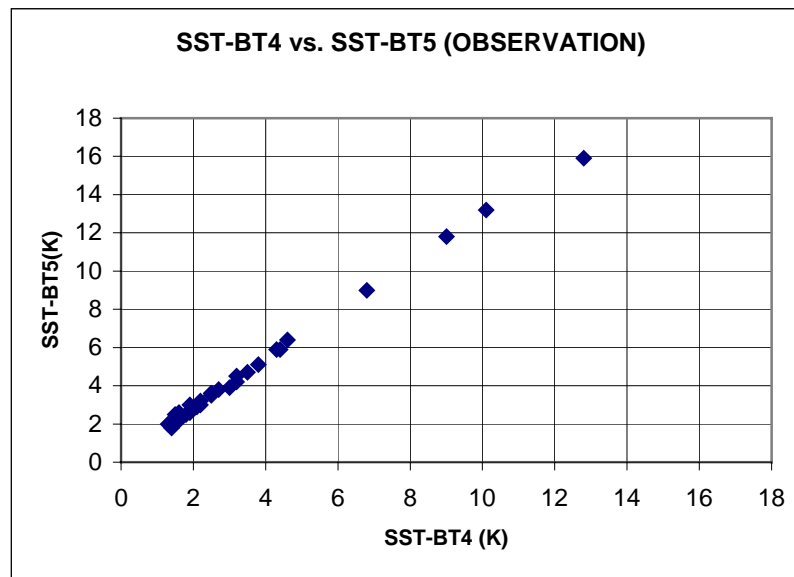
Figure 6. The relationship between temperature deficits at AVHRR channel 4 and channel 5 from observations.

Figure 7 is similar to Figure 6, but the data comes from the simulation of a transmittance model (Barton *et al*., 1993). The maximum temperature deficit, approximately 10 K, is smaller than the observed deficits. The relationship is also linear. Compared to observed brightness temperatures, the model simulations showed a bias of 0.95 K at channel 4 and 1.36 K at channel 5.

Figure 8 is similar to Figure 7, except that the data are obtained from MODTRAN simulations, and the maximum temperature deficit, approximately 10 K, is also smaller than observed deficits. The relationship is also linear. Compared to observed brightness temperatures, the MODTRAN simulations showed a bias of 0.51 K at channel 4 and 0.37 K at channel 5. The model error is much smaller in the MODTRAN simulation than that in Barton's transmittance model simulations. The large bias is caused by a few exceptional pixels. The temperature deficits of these pixels are larger than 10 K. By excluding these pixels and calibrating the simulation to observations, the differences can be reduced to < 0.1 K.
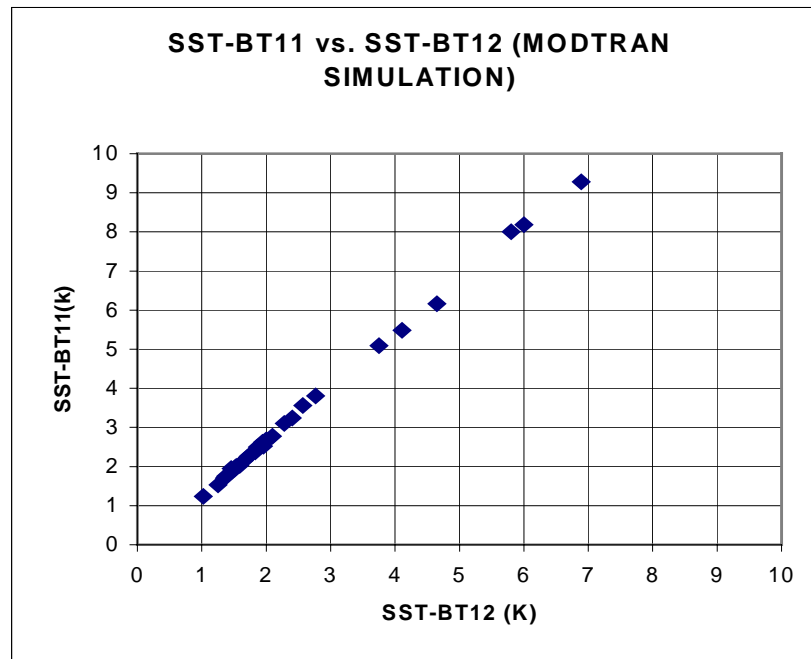
Figure 7. The relationship between temperature deficits at AVHRR channel 4 and channel 5 from simulation of a transmittance model.
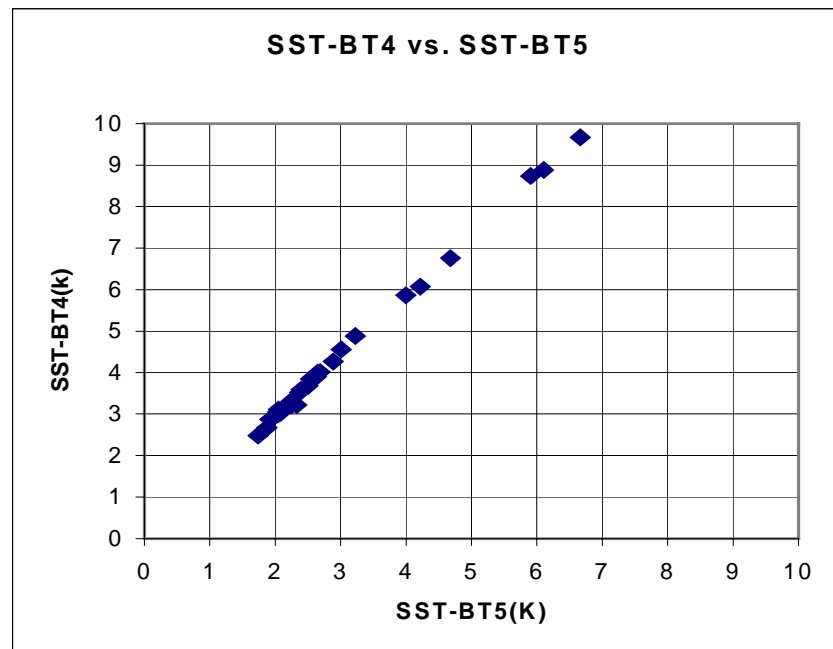
Figure 8. The relationship between temperature deficits at AVHRR channel 4 and channel 5 from MODTRAN simulations.

These results suggest that the SST retrieval is basically a linear problem. We have tried high-order nonlinear regression methods and neural network methods. The improvements are very limited and insignificant. Currently, the SST uncertainties for both linear and nonlinear regression algorithms are about 0.6 ~ 0.7 K. Figure 9 shows the split window SST precision as a function of sensor noise levels and different polynomial orders. This figure concluded that the higher order (higher than 3) nonlinear methods do not improve or deteriorate the results, in general, for lower noise data and can deteriorate the results significantly for very noisy data.
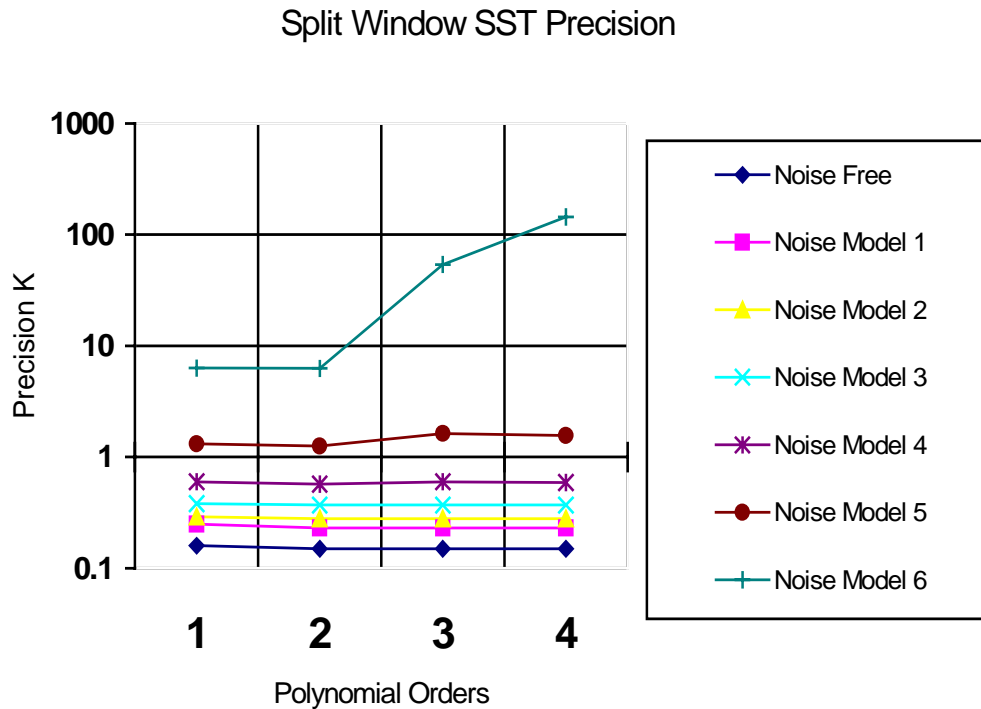
Figure 9. SST precision as a function of noise models and polynomial orders.

In general, the emissivity is uniform for SST. Therefore, Equation 1 can be solved numerically to retrieve T_s (SST) if the atmospheric profiles are known. However, it is very difficult and computationally consuming to solve Equation 1 unless we know exact atmospheric profiles. This is highly unlikely in the near future.

3.3.2   Mathematical Description of the Algorithm

3.3.2.1 Regression Methods

The baseline VIIRS SST algorithm is based on regression methods. Traditional statistical regression methods for satellite SST retrieval are linear or nonlinear multi-channel regression methods (MCSST). Another statistical method is the neural network method. There are also other options for statistical methods, such as water vapor methods (Emery *et al*., 1994). Because the SST changes slowly with time, the statistical method has a great advantage to reach high accuracy if high quality *in situ* data are available. The ATSR-like physical retrieval is also a regression method. The difference between MCSST and ATSR SST is that the MCSST matches

the TOA radiances with bulk SST, while ATSR SST retrieval is based on model simulations and retrieved skin SSTs. The following equations may be used for both MCSST, and ATSR-like SST retrieval. However the physics of the two methods are different. These equations may also be used for statistical retrieval of skin SSTs. In that case we need a global system to provide *in situ* skin SSTs.

The following regression methods are used in VIIRS SST retrieval testbed to derive the final algorithm and to drive the sensor design:

Daytime:

Split window (10.8 + 12 µm bands) nonlinear: (Modified from AVHRR operational, May *et al*., 1998)

$$SST = a_0 + a_1 T_{11} + a_2(T_{11} - T_{12}) + a_3(\sec(z) - 1) + a_4(T_{11} - T_{12})^2 \tag{12}$$

Triple window (10.8, 12, 8.55 µm bands) nonlinear: (new)

$$SST = a_0 + a_1 T_{11} + a_2(T_{8.55} - T_{12}) + a_3(\sec(z) - 1) + a_4(T_{11} - T_{12})^2 + a_5(T_{11} - T_{8.55})^2 \tag{13}$$

Quad (10.8, 12, 3.7,4.05 µm bands) algorithm: (new)

$$SST = a_0 + a_1 T_{11} + a_2 T_{12} + a_3(\sec(z) - 1) + a_4 T_{3.7} + a_5 T_{4.0} + a_6 T_{3.7} \cos(zs)$$
$$+ a_7 T_{4.0} \cos(zs) + a_8(T_{11} - T_{12})^2 \tag{14}$$

Five bands (10.8, 12, 3.7,4.05,8.55 µm bands) algorithm: (new)

$$SST = a_0 + a_1 T_{11} + a_2 T_{12} + a_3(\sec(z) - 1) + a_4 T_{3.7} + a_5 T_{4.0} + a_6 T_{3.7} \cos(zs)$$
$$+ a_7 T_{4.0} \cos(zs) + a_8 T_{8.55} + a_9(T_{11} - T_{12})^2 \tag{15}$$

Water vapor algorithm: (Emery *et al*., 1994)

$$SST = a_0 + a_1 T_{11} + a_2(T_{11} - T_{12}) + a_3(\sec(z) - 1) + a_4 * wat \tag{16}$$

Where *z* is the satellite zenith angle at the Earth's surface, ranging from 0° to 53°. *zs* is the solar zenith angle (0° to 80° as daytime). *wat* is the total column water. The temperatures T_{11}, T_{12}, T_{10}, $T_{4.0}$, and $T_{8.55}$ correspond to the 10.8, 12, 3.7, 4.05, and 8.55 *µm* bands respectively.

Nighttime:

Split window (10.8 + 12 µm bands) nonlinear: (Modified from AVHRR operational, May *et al*., 1998)

$$SST = a_0 + a_1 T_{11} + a_2 (T_{11} - T_{12}) + a_3 (\sec(z) - 1) + a_4 (T_{11} - T_{12})^2 \tag{17}$$

Triple window (10.8, 12, 3.7 μm bands) nonlinear: (Modified from AVHRR nighttime retrieval, May *et al.*, 1998)

$$SST = a_0 + a_1 T_{11} + a_2 (T_{3.7} - T_{12}) + a_3 (\sec(z) - 1) + a_4 (T_{11} - T_{12})^2 + a_5 (T_{11} - T_{3.7})^2 \tag{18}$$

Triple window (10.8, 12, 8.55 μm bands) nonlinear: (new)

$$SST = a_0 + a_1 T_{11} + a_2 (T_{8.55} - T_{12}) + a_3 (\sec(z) - 1) + a_4 (T_{11} - T_{12})^2 + a_5 (T_{11} - T_{8.55})^2 \tag{19}$$

Quad (10.8, 12, 3.7, 4.05 μm bands) algorithm: (new)

$$SST = a_0 + a_1 T_{11} + a_2 T_{12} + a_3 (\sec(z) - 1) + a_4 T_{3.7} + a_5 T_{4.0} + a_6 T_{3.7}^{\ 2} + a_7 T_{4.0}^{\ 2} + a_8 (T_{11} - T_{12})^2 \tag{20}$$

Five bands (10.8, 12, 3.7, 4.05, 8.55 μm bands) algorithm: (new)

$$SST = a_0 + a_1 T_{11} + a_2 T_{12} + a_3 (\sec(z) - 1) + a_4 T_{3.7} + a_5 T_{4.0} + a_6 T_{8.55} + a_7 (T_{11} - T_{12})^2 \tag{21}$$

Water vapor algorithm: (Emery *et al.*, 1994)

$$SST = a_0 + a_1 T_{11} + a_2 (T_{11} - T_{12}) + a_3 (\sec(z) - 1) + a_4 * wat \tag{22}$$

where z is the satellite zenith angle at the earth's surface, ranging from 0° to 53°, *wat* is the total column water. The temperatures T_{11}, T_{12}, $T_{3.7}$, $T_{4.0}$, and $T_{8.55}$ correspond to the 10.8, 12, 3.7, 4.05, and 8.55 *μm* bands respectively.

Only a few of these equations will be used in the VIIRS SST retrieval. This will depend on the final design of the VIIRS instrument. Our current algorithm uses equation 14 for daytime retrieval and equation 20 for nighttime retrieval (duel split window algorithm). Equations 12 and 17 (single split window algorithm) are back-up algorithm when sun glint occurs. Section 3.4 presents part of the VIIRS flowdown results. As discussed in above section, the higher order polynomial terms and neural network do not improve the results. Therefore, only second order polynomial terms are used in the VIIRS algorithm. In order to improve uncertainty and accuracy, the SST field will be stratified into a few groups, and regression equations will be derived for each group.

3.3.2.2 Improvement to the baseline quad (or dual split window) algorithm

The quad algorithm by using 10.8, 12, 3.7 and 4.05 μm defined ad (14) for daytime and (20) as nighttime is our **baseline algorithm**. Under certain conditions when mid-IR measurements are unavailable, such as solar glint event, the split window algorithm (equations (12) and (17)) will

be used as back-up algorithm. Figure 10 shows a sun glint case in the TRMM observation. TRMM VIRS 3.75 micron and visible 0.66micron band radiances significantly increase in solar glint area. The sun glint has negligible effect on far-IR measurements.
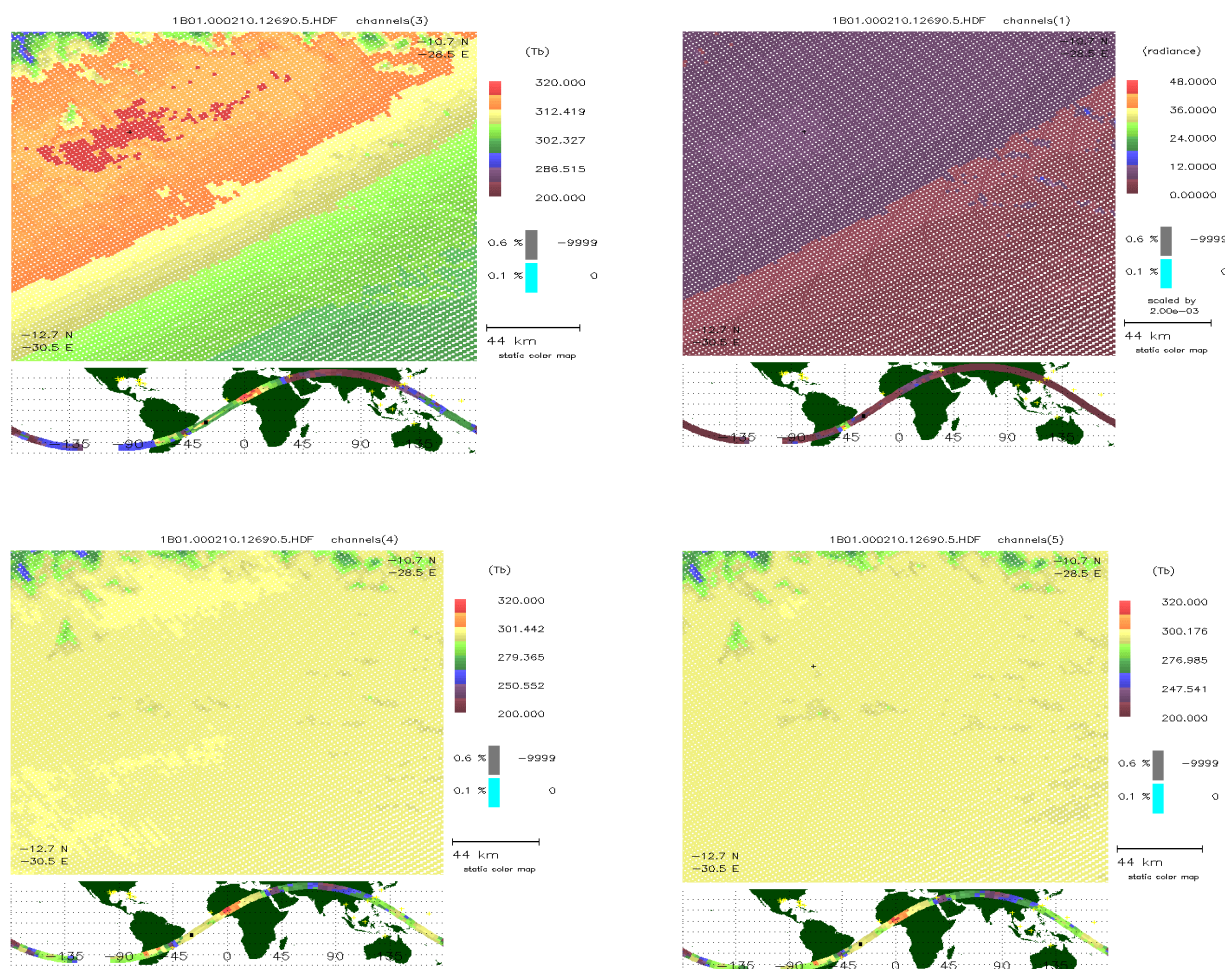
Figure 10 TRMM VIRS channel 3 brightness temperature (3.75 micron), channel 1 (0.66 micron) reflectance, Channel 4 (11 micron) brightness temperature, and channel 5 (12 micron) brightness temperature.

The baseline algorithm is improved by separating algorithm into two categories at threshold 11 µm brightness temperature 282K. Therefore, in the improved algorithm, there are a total of 2 sets of regression coefficients in both daytime and nighttime. In this way, quad algorithm can work well at both warm and cold temperatures. As indicated in the quad algorithm coefficients, 11µm brightness temperature plays the major role at colder temperatures, while 4.05µm brightness temperature plays the major role at warmer temperature.

Analysis of the global SST retrieval error has demonstrated that larger errors may associated with air mass attribute. In order to reduce the error, an air mass classification technique was introduced to the VIIRS SST retrieval to. The following diagram shows the flow process of this

method. In this method, the total precipitable water (TPW) is used as a decision tool for classification, but not as parameter in the SST equation, such that the error in TPW will not contribute significantly to the SST retrieval.
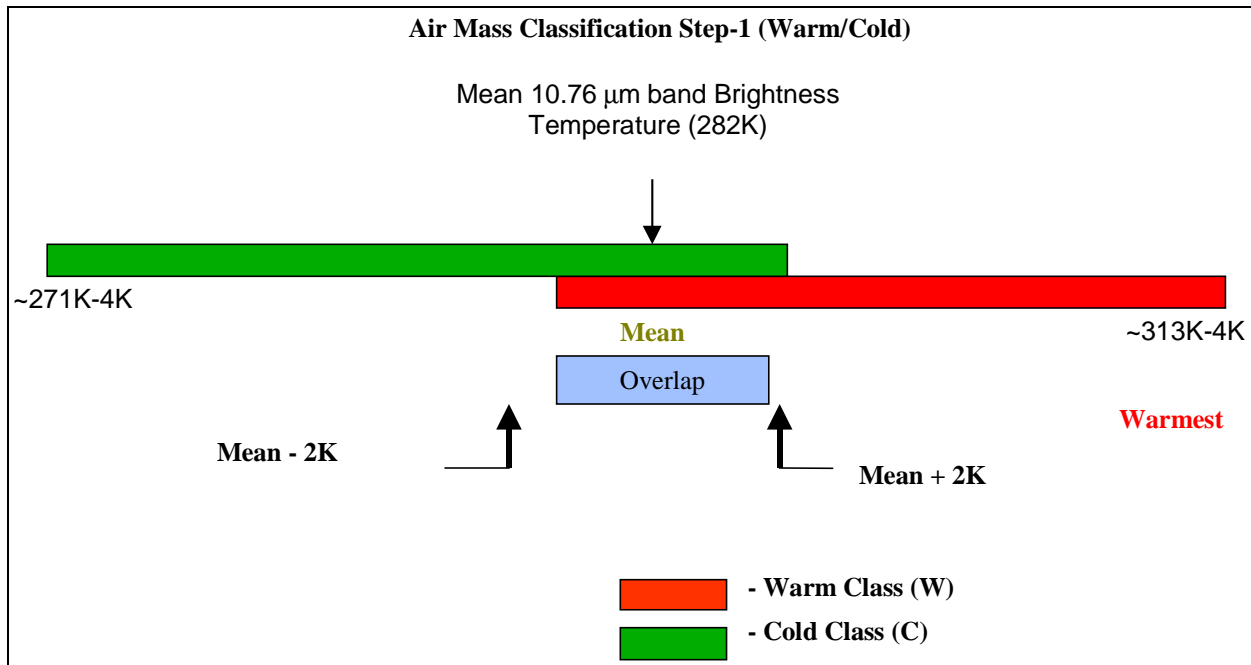
Figure 11a. Air mass classification diagram – step 1 (warm/cold)
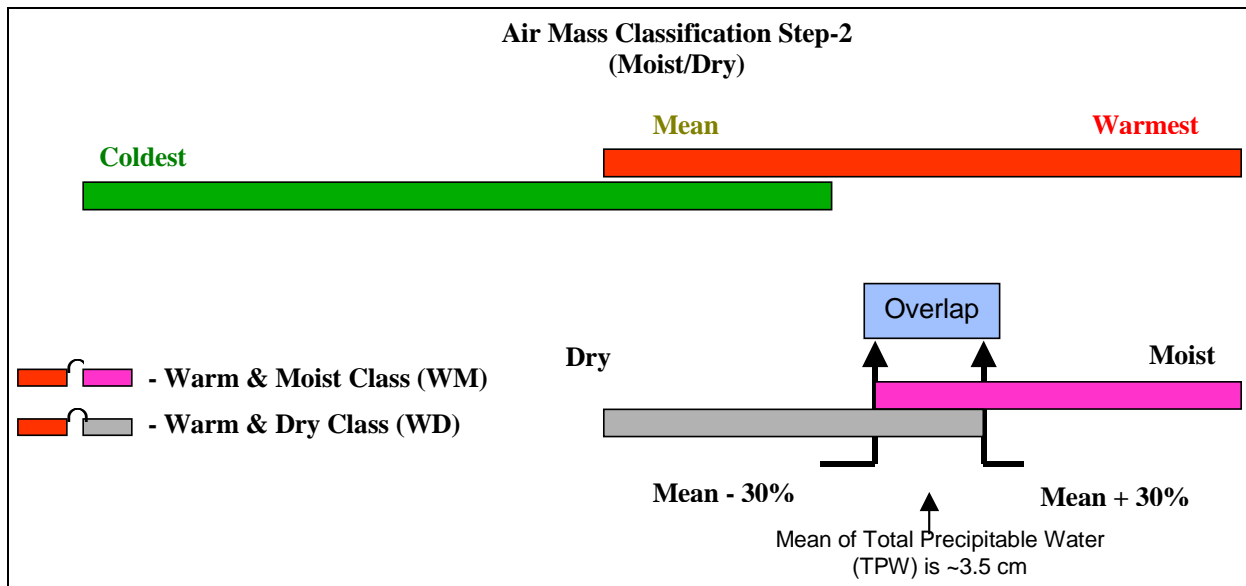
Figure 11b. Air mass classification diagram –step 2 (moist/dry)

3.3.2.3 Physical Methods

The advantages of regression methods are simplicity and speed. In addition, stable calibration error is tolerable. With the split-IR windows, the uncertainty is about 0.7 K. By using an additional window channel at 3.7 μm, the uncertainty can be improved at nighttime. At daytime the band at 3.7 μm is affected by solar radiation.

More accurate sea surface temperatures are required for the study of the climate. The accuracy of the ocean currents, which are derived from IR radiometric data, depends strongly on the accuracy of the sea surface temperature field. An accuracy of 0.2 K is required to meet the application for the turbulent exchange of energy between the atmosphere and ocean.

Physical inversion methods have been applied for the retrieval of temperature and moisture profiles from sounding data such as TOVS (Susskind *et al.*, 1983). The method has not been applied to image data yet. Image data has an advantage of higher spatial resolution and lower sensor noise. It is reasonable to consider development of an efficient method using the VIIRS data.

Satellite measured radiance is a function of the atmospheric profiles and surface properties. For the IR window and water vapor channels, the radiance over oceans at the top of the atmosphere is mainly a function of the sea surface temperature and the temperature and moisture profiles. One can choose a few channels (e.g., 3 channels) for which only the main structures of the temperature and moisture profiles are required to obtain sea surface temperature. The main structure for the mixing ratio $q(p)$ of water vapor may be described by a power law (Smith, 1966; Liu *et al.*, 1991):

$$q(p) = g(\alpha+1)W / p_0 (p / p_0)^{\alpha} \tag{23}$$

where g is the acceleration of gravity, W is total column water vapor, p is the atmospheric pressure, and p_0 the atmospheric pressure at the surface. The satellite-measured radiance at channel k in be approximately expressed as:

$$\begin{aligned} R_k &= f_k(W, T_s, \alpha) + \varepsilon'(k) \\ &= R_k^0 + \frac{\partial f_k}{\partial W}\Delta W + \frac{\partial f_k}{\partial T_s}\Delta T_s + \frac{\partial f_k}{\partial \alpha}\Delta \alpha + \varepsilon(k) \end{aligned} \tag{24}$$

where $\varepsilon(k)$ is the total error due to the above assumption and the sensor noise, R_k^0 is the radiance for the present atmospheric state, and T_s is sea surface temperature. By applying three channels, one can have three equations. Thus, an inversion equation can be written as:

$$\Delta P = \left[AA^T + \varepsilon \right]^{-1} A^T \Delta R \tag{25}$$

where:

$$\Delta\mathbf{P} = \begin{bmatrix} \Delta W \\ \Delta T_s \\ \Delta\alpha \end{bmatrix}, \ \Delta\mathbf{R} = \begin{bmatrix} R_1 - R_1^0 \\ R_2 - R_2^0 \\ R_3 - R_3^0 \end{bmatrix}, \ \mathbf{A} = \begin{bmatrix} \dfrac{\partial f_1}{\partial W} & \dfrac{\partial f_1}{\partial T_s} & \dfrac{\partial f_1}{\partial\alpha} \\ \dfrac{\partial f_2}{\partial W} & \dfrac{\partial f_2}{\partial T_s} & \dfrac{\partial f_2}{\partial\alpha} \\ \dfrac{\partial f_3}{\partial W} & \dfrac{\partial f_3}{\partial T_s} & \dfrac{\partial f_3}{\partial\alpha} \end{bmatrix} \tag{26}$$

$\mathbf{A^T}$ is the transpose of matrix $\mathbf{A}$, and ε is an error matrix.

3.3.3 Archived Algorithm Output

Brightness temperatures at pixel level are computed for all VIIRS mid-IR and far-IR bands for all satellite viewing angles. The best SST estimates and cloud index are archived.

3.3.4 Variance and Uncertainty Estimate

The SST retrieval uncertainty is determined by two factors: atmospheric correction and sensor performance. The best atmospheric correction error is about 0.3 K (Mutlow *et al*., 1994) at nadir viewing using a traditional split window technique. There are a number of error sources in sensor design. Among them, sensor noise, calibration error, geo-location, and band-to-band registration are the apparent error sources for SST retrieval. Since calibration does not contribute to retrieval precision, we will consider sensor noise first. If the NEDT values are about 0.1 K for split windows, the precision at nadir due to atmospheric correction and sensor noise will be typically 0.5 K. The error will be much larger at large satellite viewing angles. Figure 12 shows the change of retrieval precision with satellite viewing angle for the split window case. The precision is < 0.5 K near nadir, but much larger at large viewing angles. This figure shows that the precision can be improved by aggregation. However, the aggregation only improves precision due to sensor noise. In this experiment, the error due to atmospheric correction is about 0.4 K at nadir.

Figure 13 is similar to Figure 12, except it is for the nighttime triple window case. The best precision is about 0.3 K at nadir and 0.25 K after aggregation.

Three data sets were used to estimate the SST retrieval uncertainty and to evolve VIIRS SST algorithm and sensor design. The first is a data set of 299 global observations of skin SST with radiosonde atmospheric profiles and coincident satellite passes (Emery *et al*., 1994) plus 6 standard atmosphere profiles and surface temperatures. The second data set is a global snapshot of surface temperature at 2.5° x 2.5° resolution supplied by NCEP (Kalnay et al, 1996), with matching atmospheric profiles. The third data set is a 1.3 km resolution surface temperature scene derived from AVHRR 1b data.

Raytheon

Nighttime SST Precision
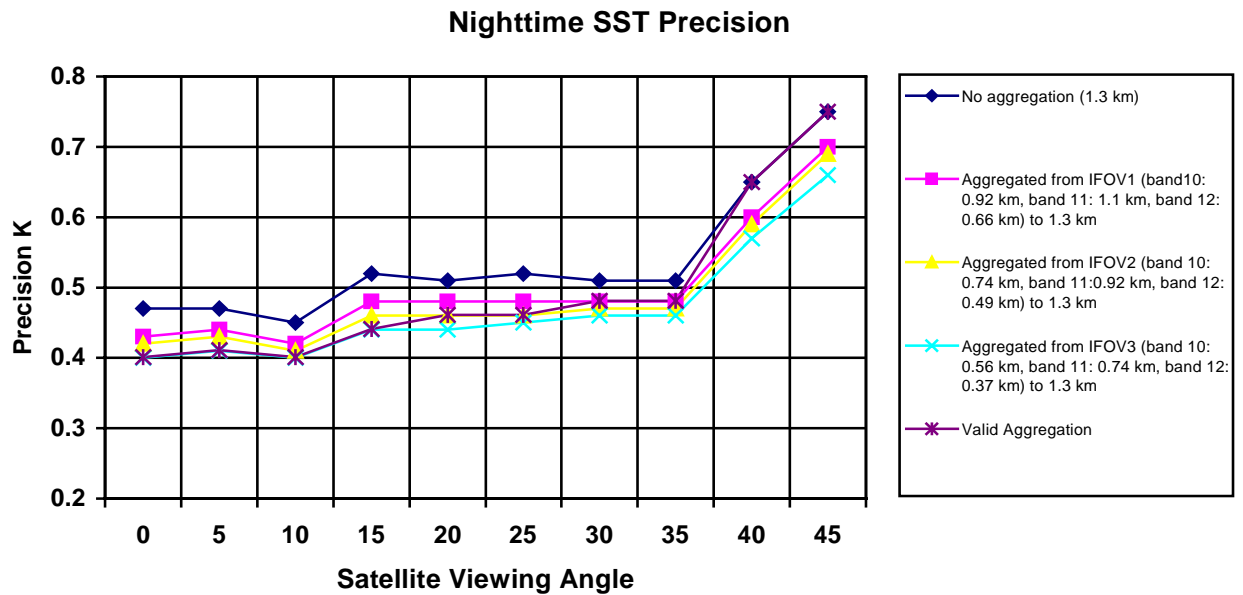
Figure 12. Changes of precision with satellite viewing angles: Split Window.

Nighttime SST Precision
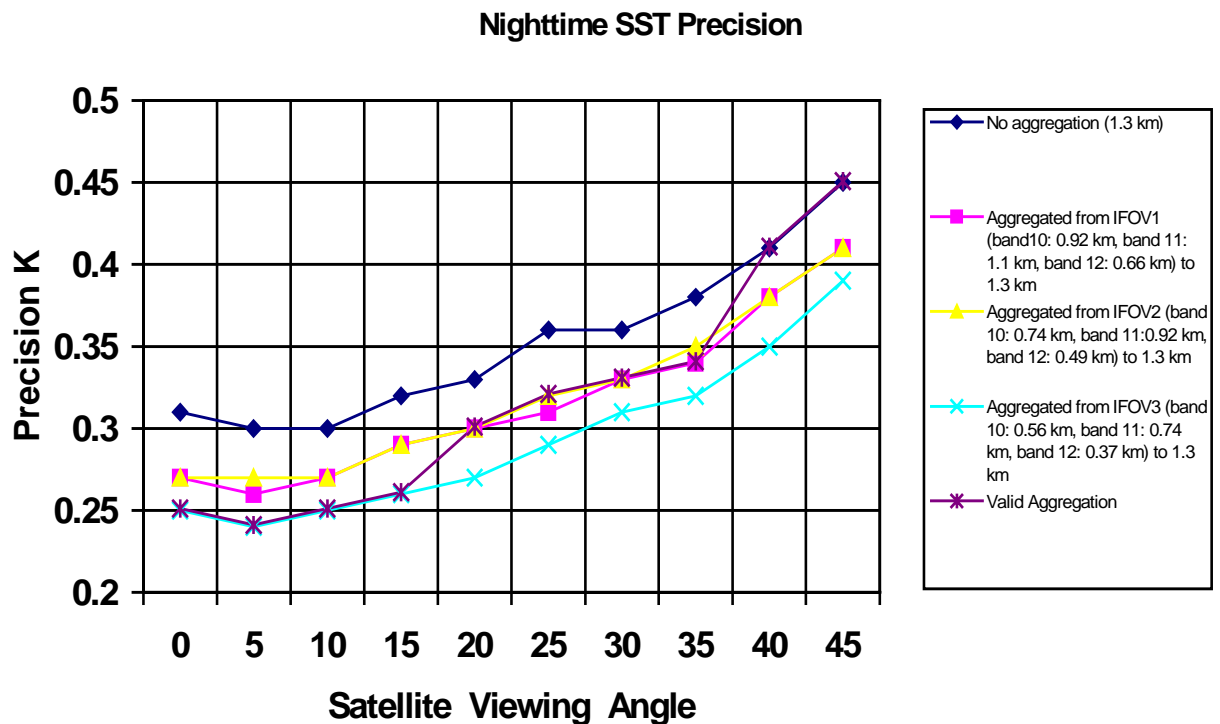
Figure 13. Changes of precision with satellite viewing angles: Triple Window.

In Figure 14, panel (b) shows the range of 299 SSTs. Simulations were performed for nighttime and daytime. The NEDT values are 0.08 K for the 11 μm band, 0.1 K for the 12 μm band, and 0.15 K for the 3.75 μm band. The differences between observed and retrieved SSTs are shown in panel b. The uncertainty for daytime (split window) retrieval is 0.5 K and for nighttime (triple window) retrievals is 0.3 K. The maximum uncertainty is about 1 K. Calibration errors were not considered in this example.
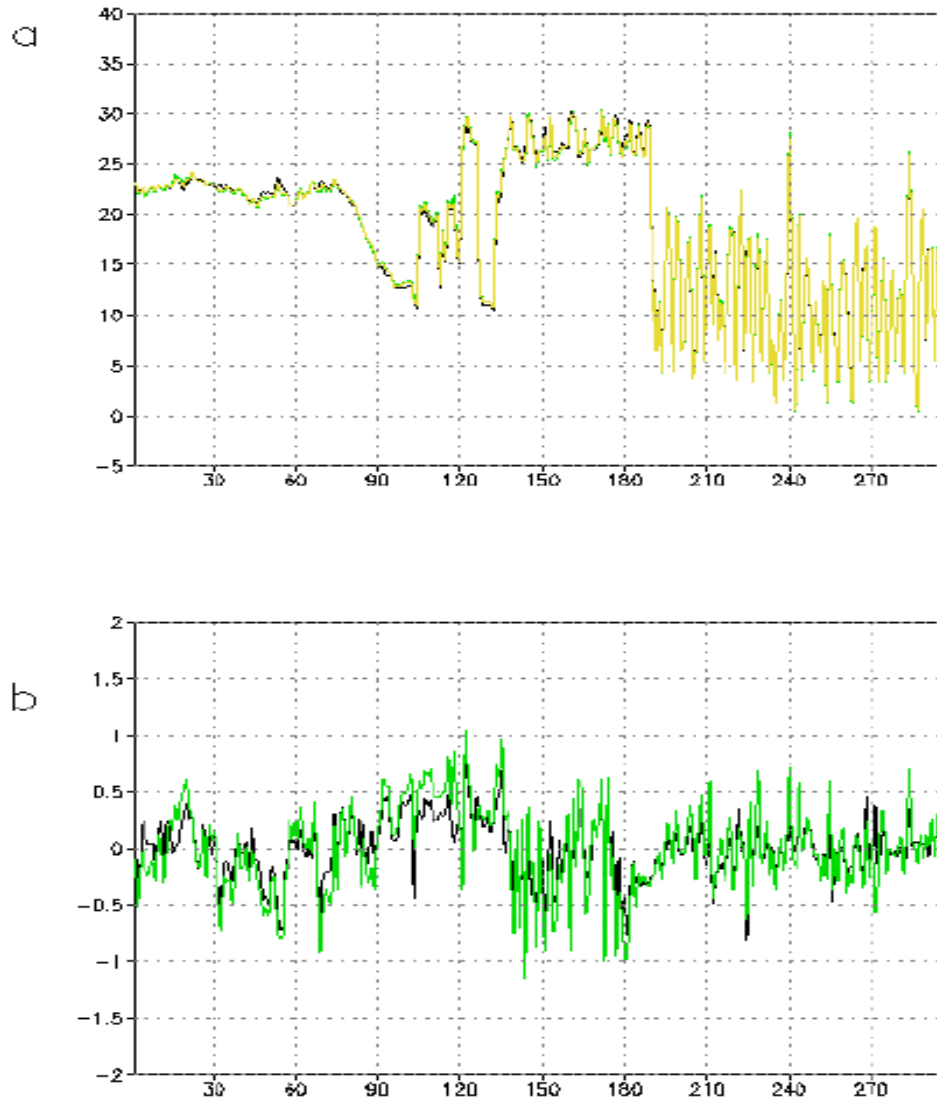
Figure 14. (a) Range of the 299 ship-observed SSTs. (b) Difference between true SST and retrieved SST. Green line: daytime. Black line: nighttime.

Figure 15 shows the SST uncertainty as a function of satellite viewing angles and SST values derived from the first data set for 6 algorithms. In order to simulate the daytime radiance, 400 simulations were performed for each pixel, reflecting different satellite viewing angles, solar zenith angles and azimuth angles. Half of the data were randomly picked as training data, others as testing data. Sensor noises are applied to both training and testing data. Absolute radiometric errors (0.4%) were applied only to testing data. In the two-channel calculation, 10.8 and 12 μm, the uncertainty is > 0.5 K for SSTs higher than 290 K. Larger uncertainties occur for warm SST and larger viewing angles. The uncertainty is < 0.5 K for viewing angles < 40° and temperatures < 290 K. Water vapor algorithm improves the uncertainty for warm SSTs and large satellite viewing angles, but there is no improvement for cold SSTs and small viewing angles. The three-channel algorithm (8.55, 10.8 and 12 μm) improves the uncertainty only for warm SSTs. The four-channel and five-channel algorithms improve the retrieval uncertainty for most SSTs and zenith angles except very low SSTs. The performance of the four-channel algorithm becomes worse when the SSTs are very cold. We speculate that the atmosphere over these surfaces is dry. Adding more bands does not provide more information for atmospheric correction, while the sensor noise at mid-IR is large at low SSTs. However, in reality, the number of pixels at low SST (270-275 K) is small and the error can be reduced by our improved air mass classification technique as discussed in the later sections in this document.

Figure 16 shows the accuracy as a function of satellite viewing angles and temperature values. The accuracy is better for warm SSTs and smaller satellite zenith angles than that for cold SSTs. There are two sources that contribute to the accuracy, atmospheric correction and absolute radiometric error. In this case, the absolute radiometric error is 0.2 percent of 300 K radiance for each channel. The relative radiometric error is larger at low SST. Another explanation is that the sampling number at SSTs < 275 K is much smaller than the total sampling number.

Figure 17 shows the precision as a function of satellite viewing angles and temperature values. The precision of the four-channel and five-channel algorithms is smaller than 0.4 K overall. For most of the SST field, the precision is < 0.3 K. The precision of the two-channel algorithm is > 0.45 K for high SSTs and large satellite viewing angles.

In Figure 18, panel (a) shows the global snapshot SST field at 00Z July 1, 1993 and panel (b) shows the retrieved SST. Panel (c) is the difference between retrieved and observed SSTs. The RMS error is 0.45 K at the 0.1 K instrument noise level. The maximum error is 1.67 K.

Figure 19 shows the uncertainty as a function of satellite viewing angles and SST values. The pattern of each panel is similar to that in Figure 17, but the results are better.

Figure 20 is accuracy distribution as a function of zenith angle and SST values. Larger mean errors occur for lower SSTs and larger viewing angles for four-channel and five-channel algorithms. For the two-channel algorithm, the largest error occurs in the mid SST range.

Figure 21 shows the precision distribution as a function of zenith angle and SST values. In this simulation, the precision is better than that derived from the radiosonde data set.
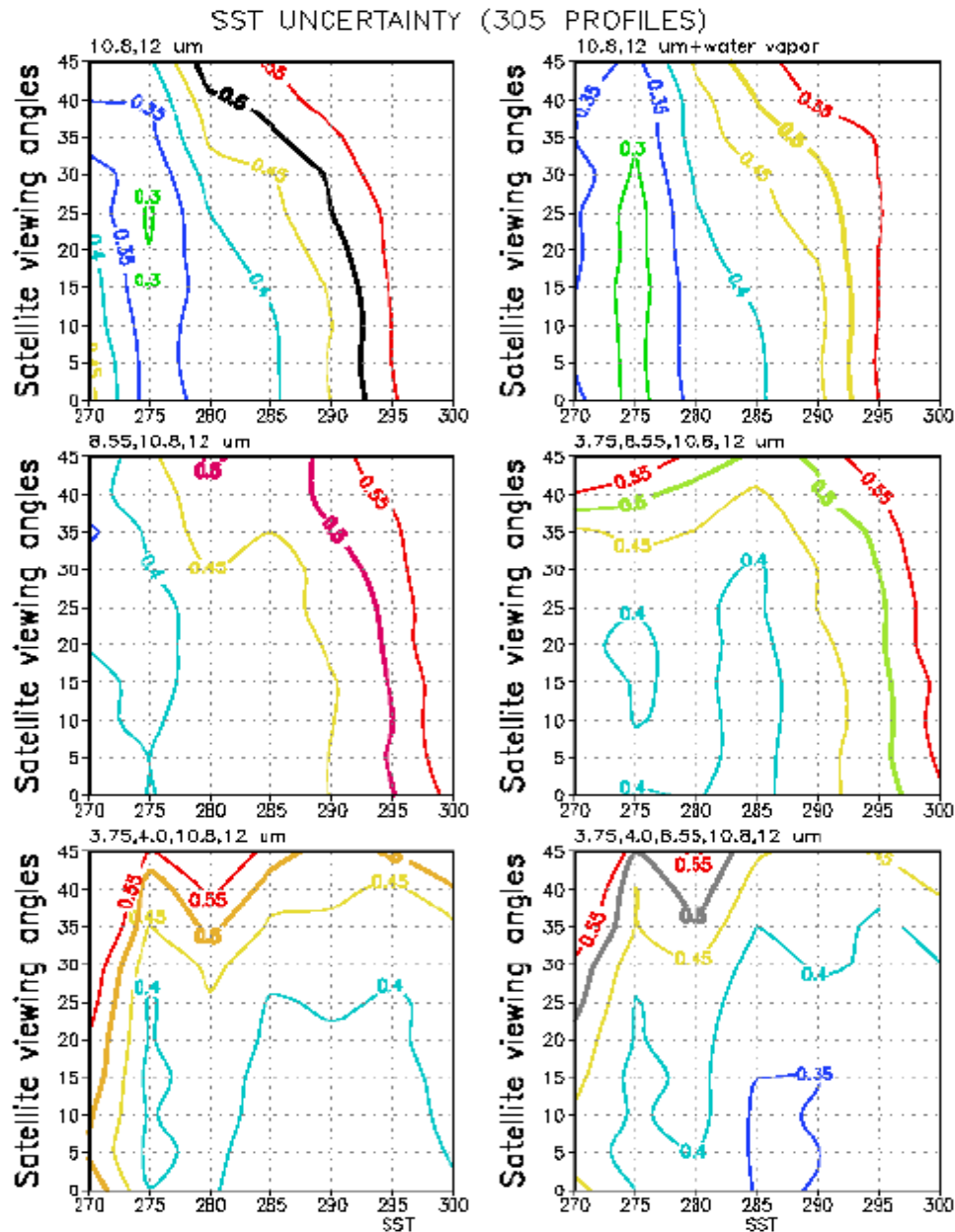
Figure 15. Uncertainty derived from radiosonde data set. There are 121,170 samples. The samples for seven SST categories from 270-275 K to 300-305 K are 240; 1,160; 1,120; 2,200; 2,120; 3,917; and 1,360.

Raytheon
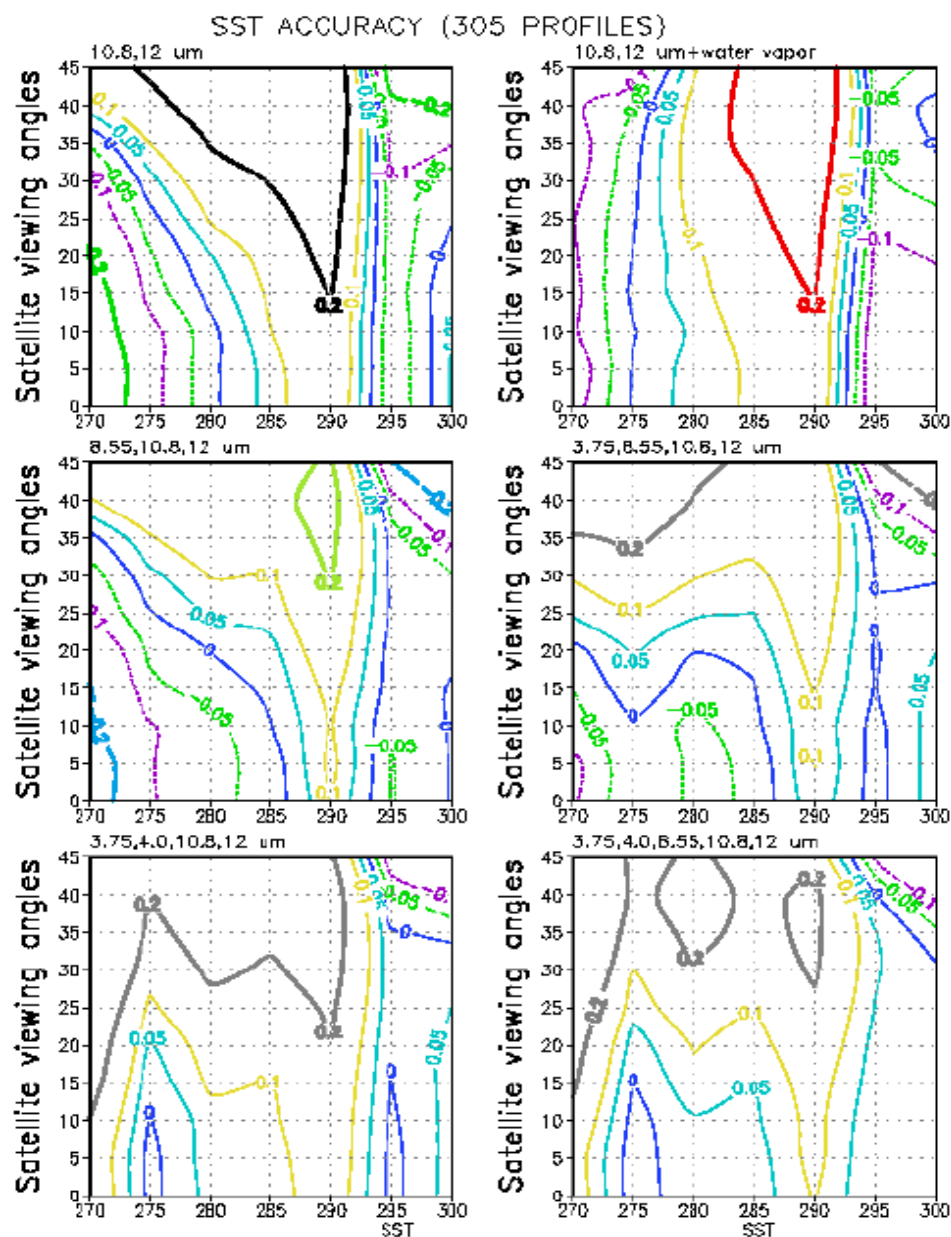
Figure 16. Accuracy derived from radiosonde data set. There are 121,170 samples. The samples for seven SST categories from 270-275 K to 300-305 K are 240; 1,160; 1,120; 2,200; 2,120; 3,917; and 1,360.
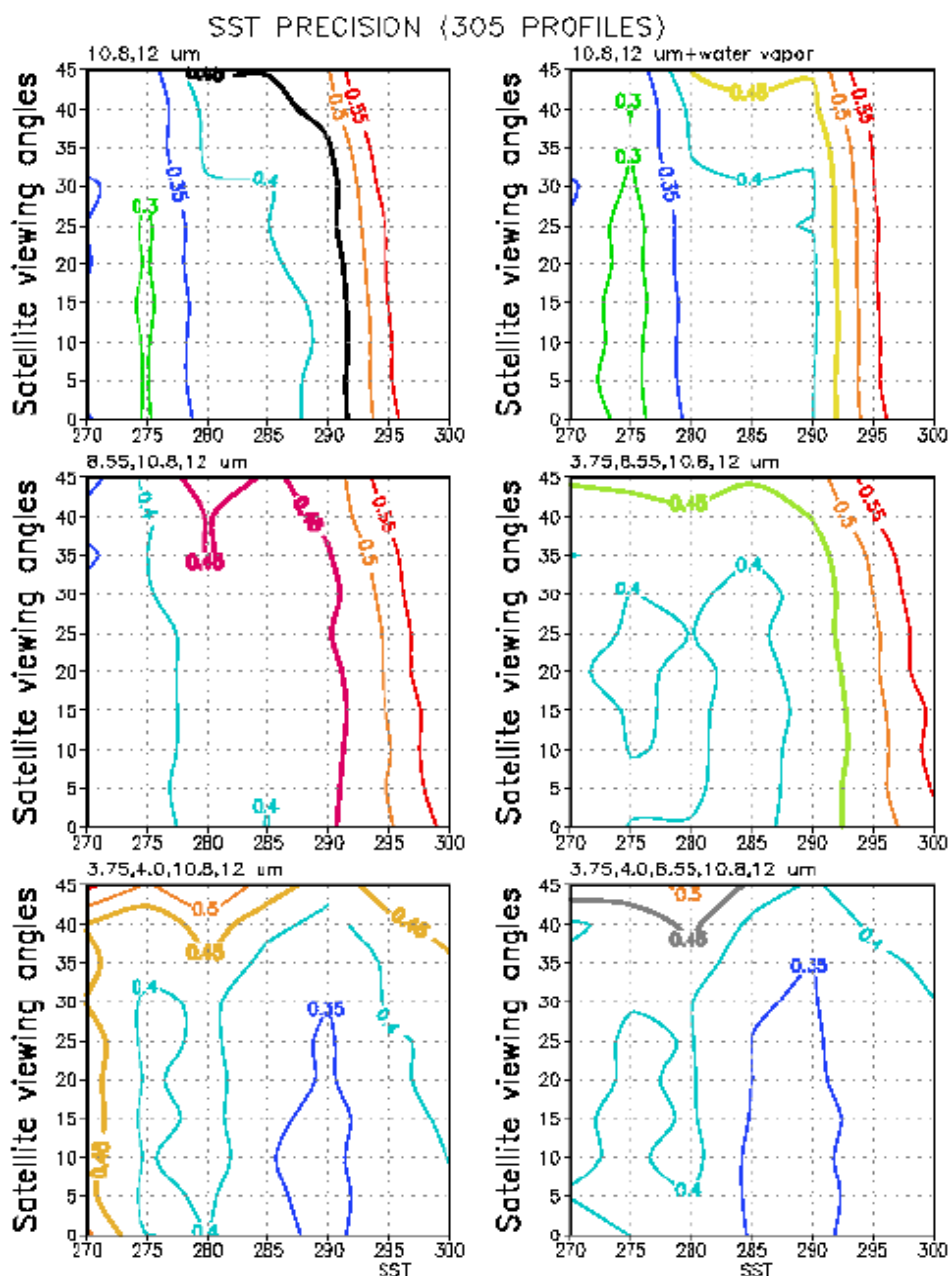
Figure 17. Precision derived from radiosonde data set. There are 121,170 samples. The samples for seven SST categories from 270-275 K to 300-305 K are 240; 1,160; 1,120; 2,200; 2,120; 3,917; and 1,360.
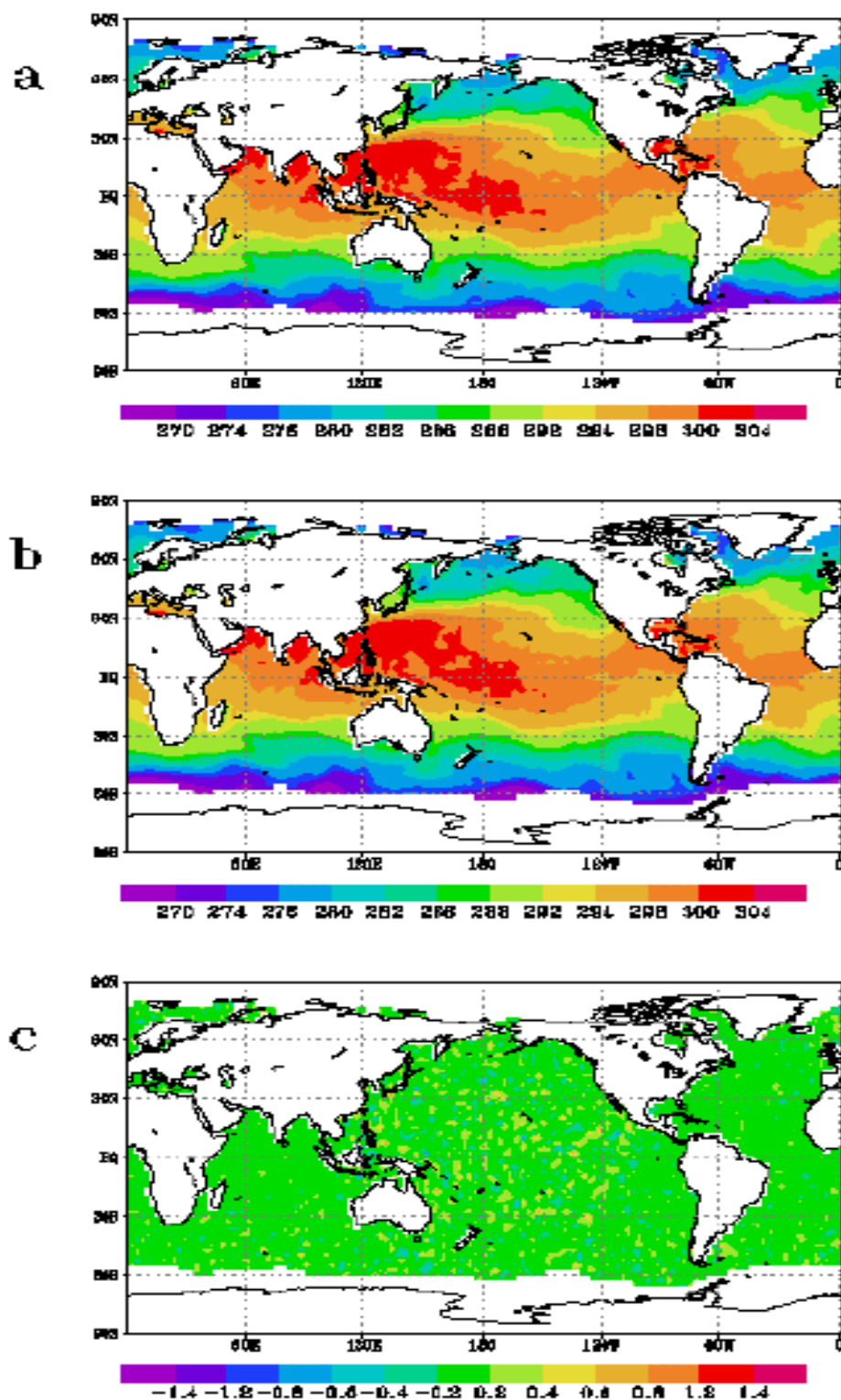
Figure 18. a. Global SST. b. Retrieved SST. c. The difference between global and retrieved SSTs.
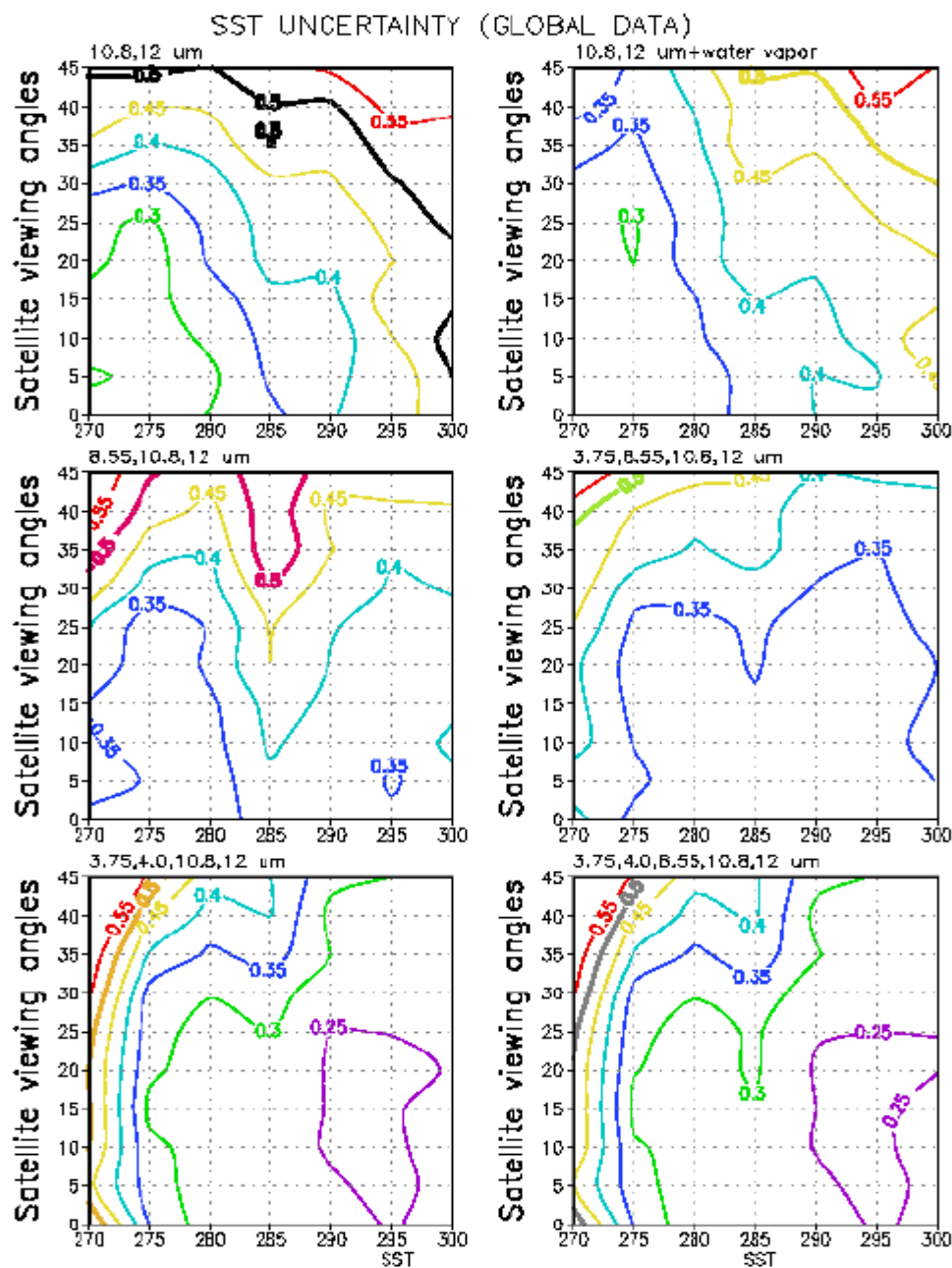
Figure 19. Uncertainty derived from the global data set. There are 26,590 samples. The samples for seven SST categories from 270-275 K to 300-305 K are 100, 343, 405, 310, 318, 910, and 265.
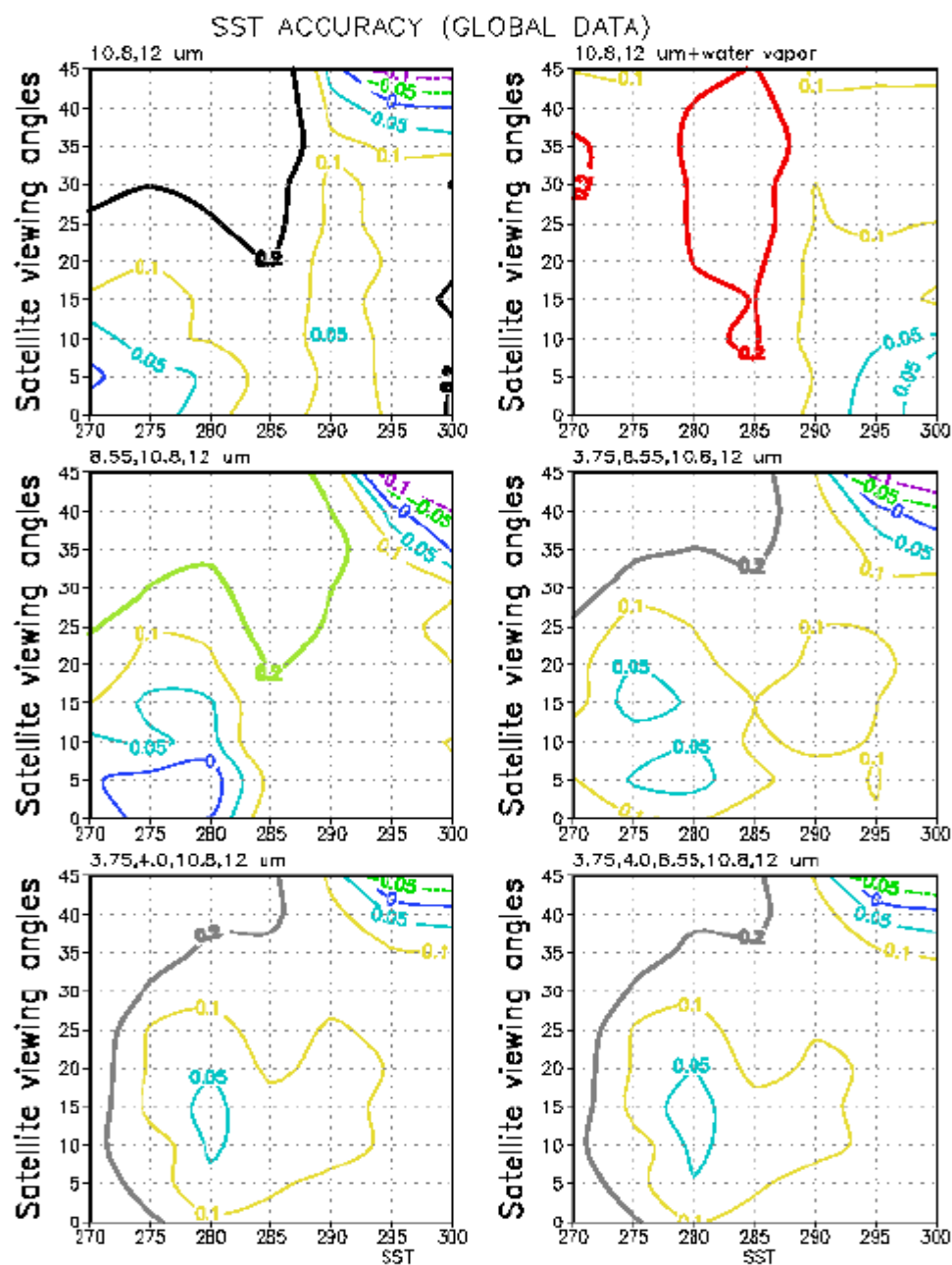
Figure 20. Accuracy derived from the global data set. There are 26,590 samples.The samples for seven SST categories from 270-275 K to 300-305 K are 100, 343, 405, 310, 318, 910, and 265.
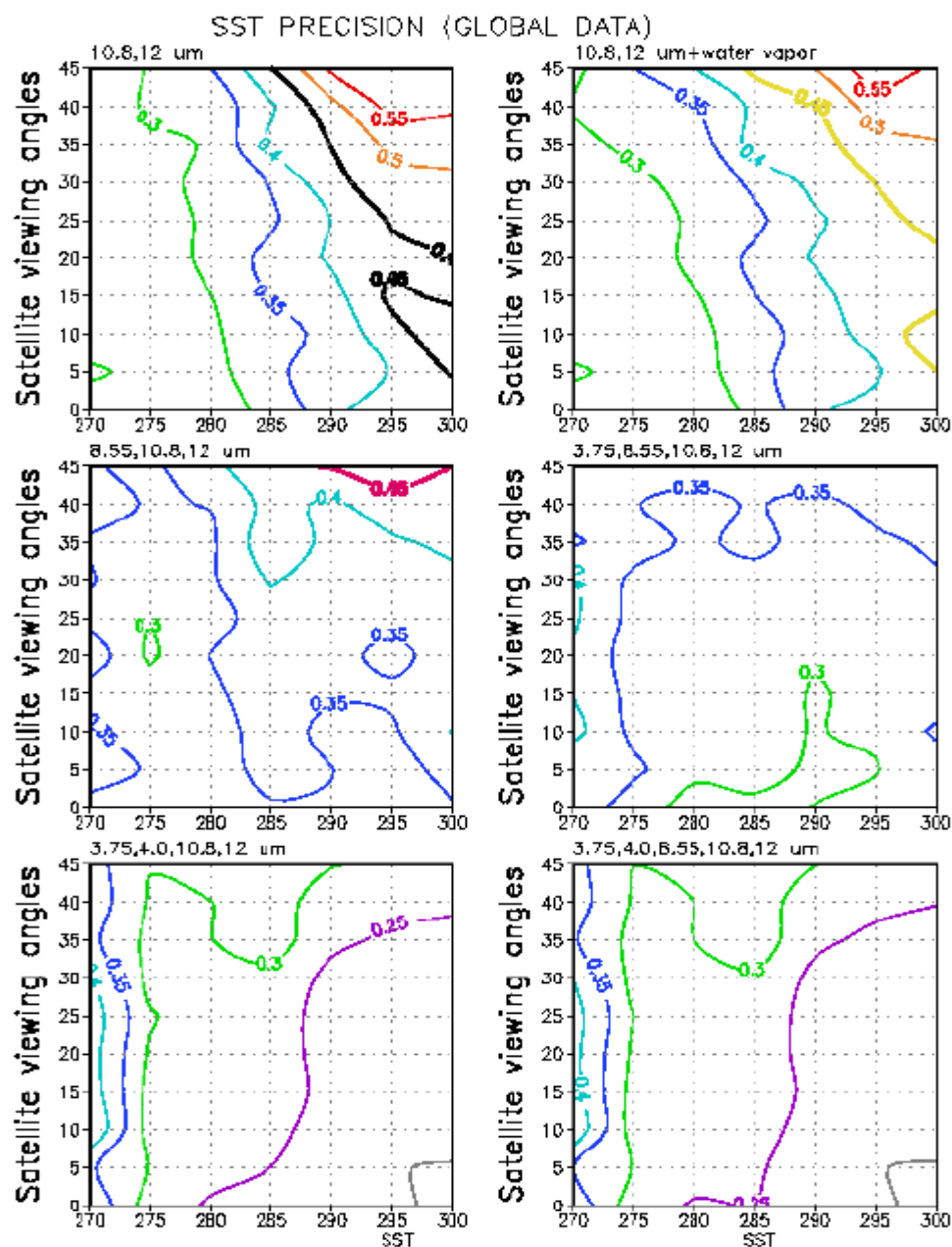
Figure 21. Precision derived from the global data set. There are 26,590 samples. The samples for seven SST categories from 270-275 K to 300-305 K are 100, 343, 405, 310, 318, 910, and 265.

In Figure 22, panel (a) is a 1 km resolution SST scene off the Florida coast which is derived from AVHRR 1B data. Two methods were used to retrieve SSTs. One uses 25 percent of the data as training data to retrieve the SST. The RMS error is 0.3 K from the split window algorithm. Because this simulation only included nine atmospheric profiles, the atmospheric correction error is underestimated. The other uses equations derived from the global snapshot SST to retrieve the high resolution SST. The uncertainty is 0.45 K for the split window and 0.28 K for the triple window algorithm.

In conclusion, the SST uncertainties are approximately 0.5 K for the split window algorithm and 0.3 K for the dual split window algorithm. The simulation with the radiosonde data set generates the worst uncertainty and may be closer to reality than the other simulations.

3.3.4.2 Output from the improved baseline algorithm

Figure 23 shows the SST retrieval error comparison between VIIRS baseline algorithm and improved algorithm with air mass classification. With air mass classification method, the maximum error is reduced to 0.8K from 1.67K. The maximum errors along the California coast and South Africa coast are reduced significantly. The precision for the original baseline algorithm with daytime and nighttime classification is 0.21K. It is improved to 0.17 K using an additional warm and cold classification, and to 0.17K if moist and dry classification is added.

3.3.4.3 Output from the physical retrieval

The physical retrieval algorithm is currently under development. At this time only a case study has been carried out. A radiosonde profile with an inversion of water vapor is chosen to test the physical retrieval algorithm. It can be seen from Figure 24 that both sea surface temperature and radiance converge to the given truth with the number of iterations increasing. Statistical results are carried out by introducing Gaussian-distributed random sensor noises of sensor model 3 (see Figure 25).

In this test, the errors in the forward model have not been considered. The forward model error was discussed in Section 3.1.1. It is expected that the forward model will be improved in the future.
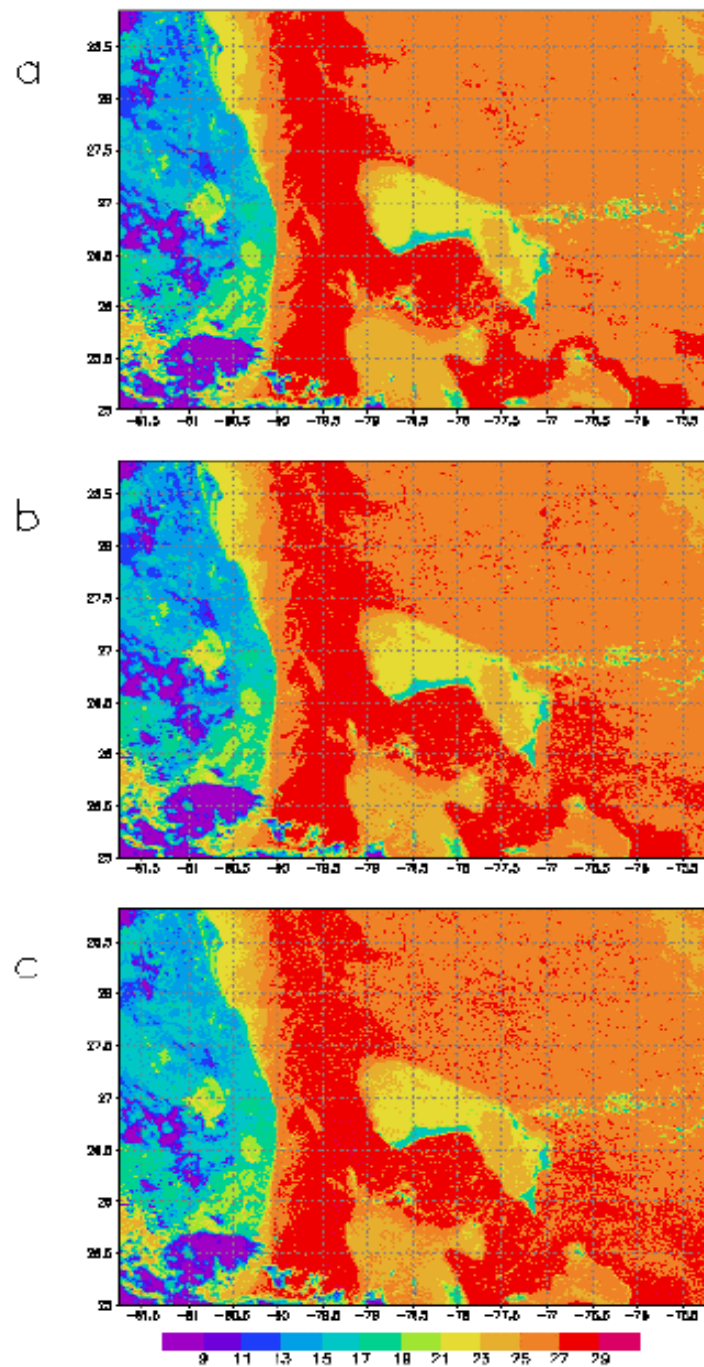
Figure 22. a. Observed 1 km SST. b. Retrieved SST using equation derived from 25 percent of the observed data. c. Retrieved SST using equation derived from global data. The noise was added by using the SBRS sensor noise model 3.
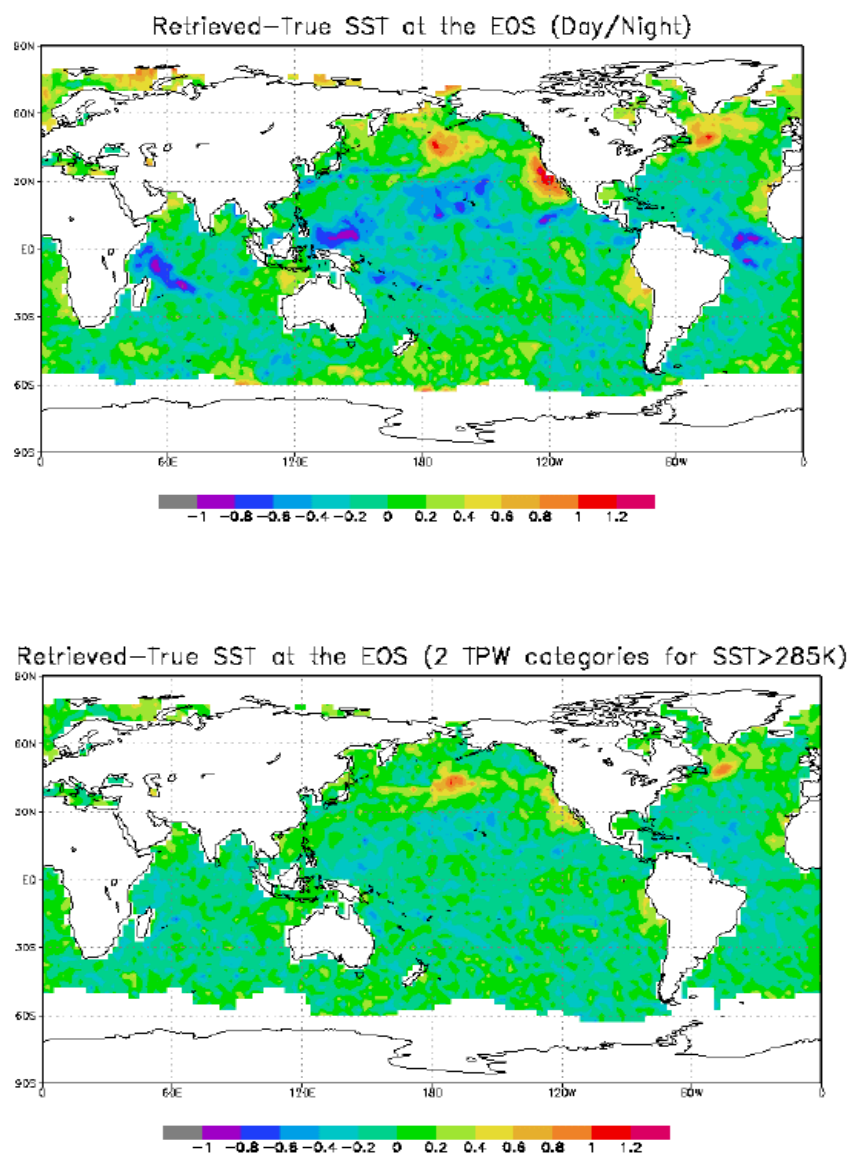
Figure 23. SST bias comparison between baseline algorithm and improved algorithm with air mass classification
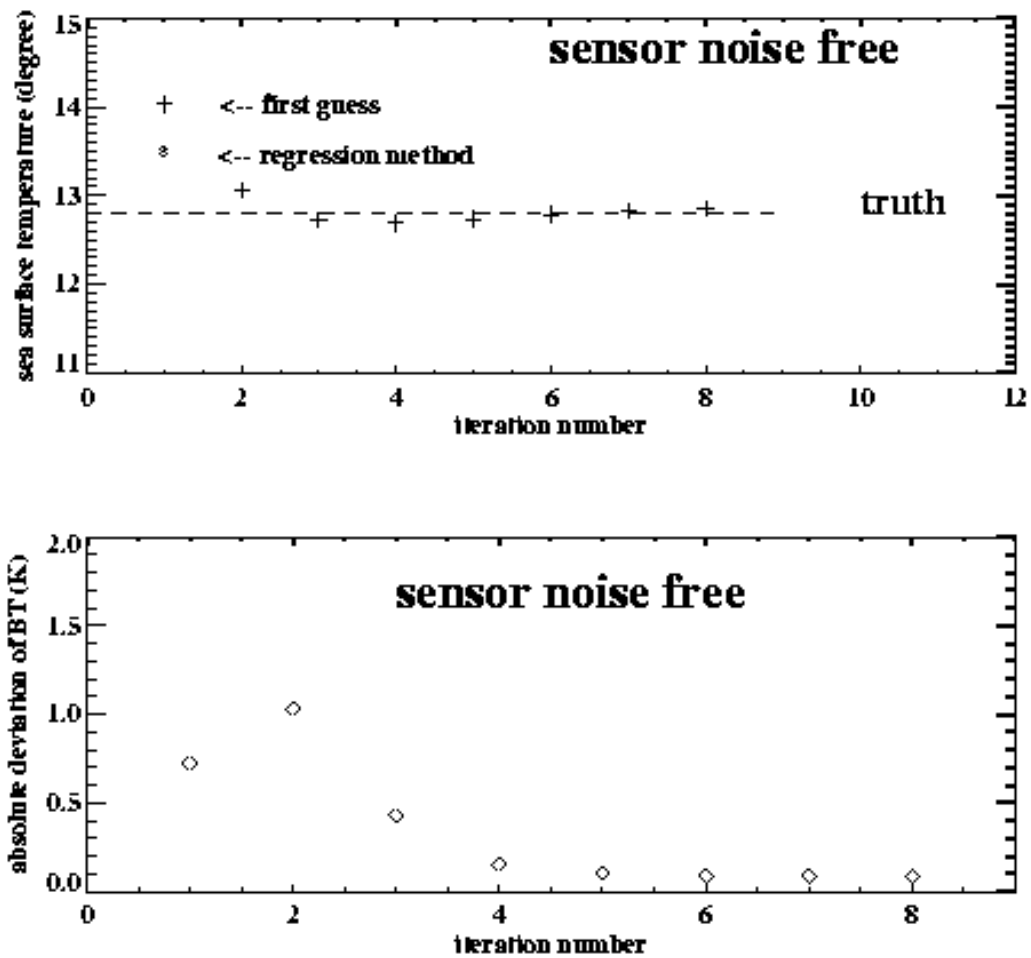
Figure 24. Variations of retrieved sea surface temperature (upper panel) and absolute deviation of the brightness temperature (bottom panel) with iteration number.
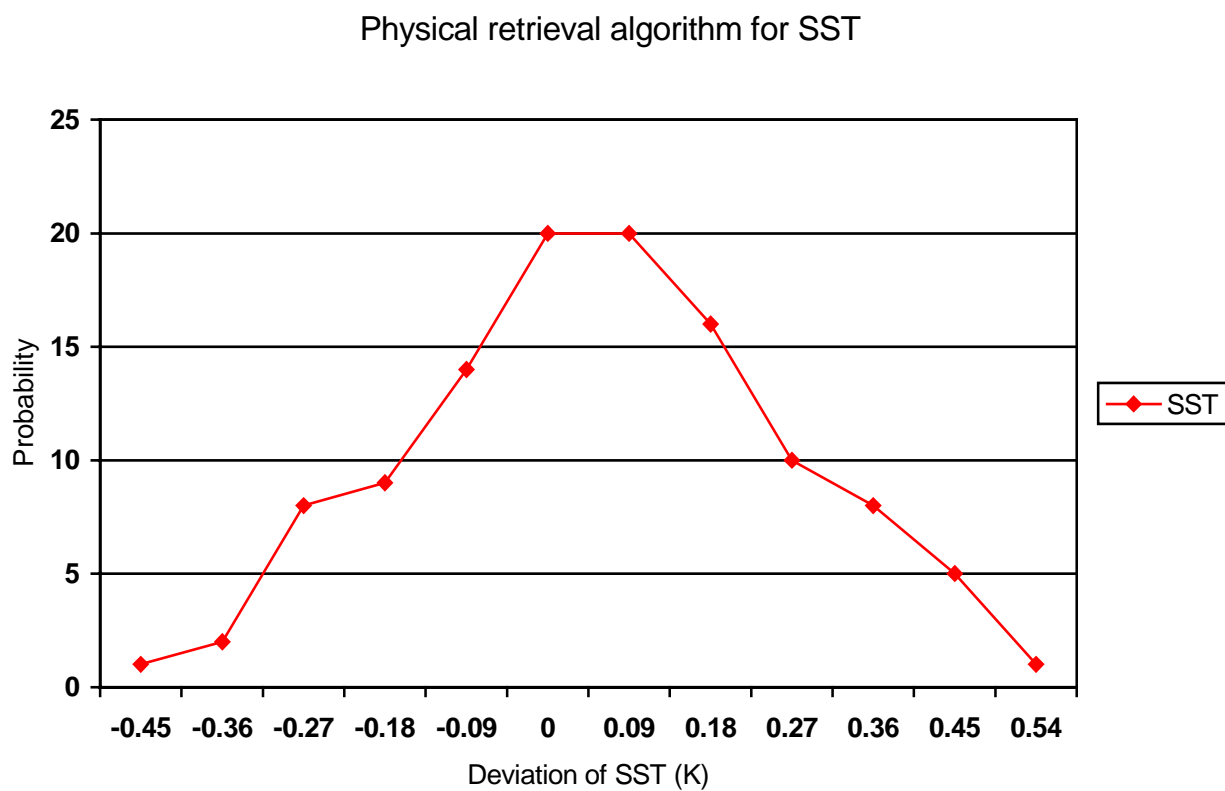
Figure 25. Error distribution of the retrieved sea surface temperature. Here, accuracy is 0.1 K, precision is 0.2 K, and uncertainty is 0.23 K.

3.4 ALGORITHM SENSITIVITY STUDIES

3.4.1 Band Center, Sensor Noise and Water Vapor

3.4.1.1 Band Centers' Effect

Before multi-channel thermal IR measurements were available, McClain (1979) reviewed the methods of deriving SST from single window measurements. Empirical corrections had been generally unsatisfactory even if the moisture information from atmospheric sounders on the same spacecraft was used. The RMS error is above 1.5 K in general for single window algorithm. The current operational SST algorithm uses 2 thermal bands for daytime retrieval and three thermal bands for nighttime retrieval. The RMS error for the 2-band algorithm is about 0.5-0.6 K and for the 3-band algorithm is about 0.4-0.5 K globally relative to global drifting-buoy SST measurements (May et al, 1996). The current operational SST retrieval methods calibrate the satellite measurement with the buoy SST. This method may not be adequate since buoys measure bulk SSTs while the satellite measures skin SST. The current operational SST algorithm may not meet the NPOESS SST threshold requirement. It is expected that the RMS error will be much larger than the 0.5 K requirement for pixels with large satellite zenith angle. This document summarizes the flowdown of the SRD requirements for the VIIRS SST to the VIIRS IR band selection. The baseline bands for VIIRS SST algorithm are VIIRS band numbers 10, 11, and 12. These are similar to the current operational bands. In research, we studied the influence of adding two more thermal bands to the algorithm. One is the 4.005 μm band. This band, together with three baseline bands comprises a dual split window structure. It is expected that this system will eliminate the solar contamination in daytime and also provide better precision on nighttime. Another is the 8.55 μm band. This band may be useful to detect thin cirrus and to improve the algorithm in daytime using the physical retrieval method. Both bands are now included in the current VIIRS sensor design.

The two baseline far-IR bands are located between 10 μm to 13 μm. The following analysis examines whether the centers of the two bands are properly located. We chose 250 global representative radiosonde profiles and skin SSTs to perform the simulation. Aerosol, MTF, band-to-band registration, and other effects are not considered. Figure 26 shows the SST precision of split window algorithm for various band combinations. The first band is fixed at 10.8 μm. The band width is 1 μm. The results that showed the worst precision were when the two bands overlapped. The best results are from where the second band is located between 11.8 μm to 12.1 μm. This indicates that the VIIRS baseline bands are adequately located.

2-band SST Precision vs Band center (the first band center at 10.8 micrometer)
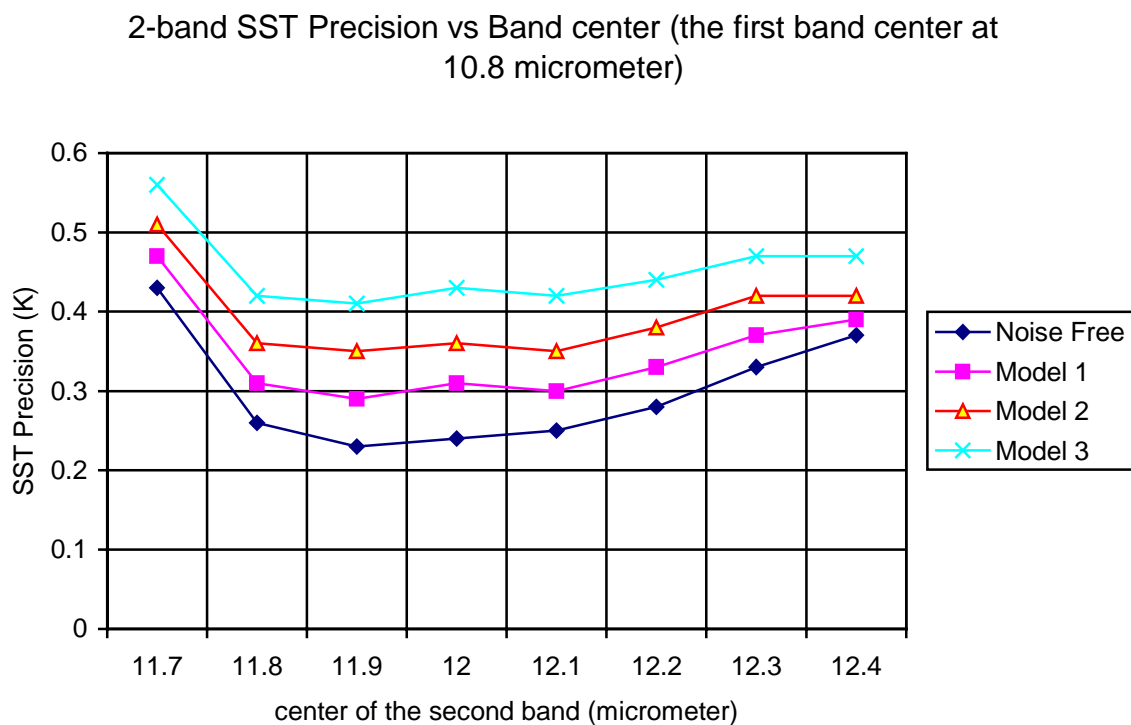
Figure 26. SST precision as a function of the band center. The first band is centered at 10.8 micrometer.

The algorithm used in this study is a non-linear algorithm. This algorithm provides better atmospheric correction. However, the sensor noise is amplified. Table 4 shows the comparison of contributions to errors from sensor noise and atmospheric correction.

Table 4. Comparisons of the Split Window SST Precision

Noise Model	NEDT (K)		Sensor Contribution to precision (K)	Atmosphere correction to precision (K)	Total Precision (K)
	10.8 µm band	12 µm band			
Noise Free	0.	0.	0.	0.25	0.25
Model 1	0.04	0.05	0.18	0.25	0.31
Model 2	0.06	0.07	0.27	0.25	0.37
Model 3	0.08	0.10	0.35	0.25	0.43

Figure 27 shows the results of the 4-band solution at nighttime. The position of the second band does not make a substantial difference. The results are much improved compared to the two-band solutions. Due to the narrow spectrum of the mid-IR window, there is not much room to move these bands around.

4-band SST Precision vs Band center (the other band centers at 3.75, 4.0,10.8 micrometer)
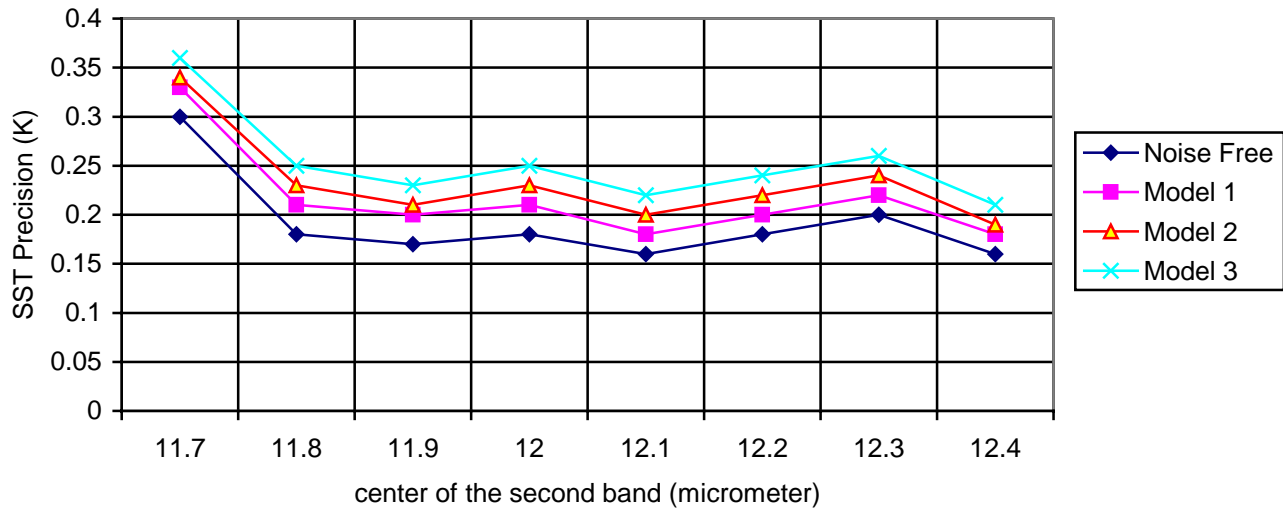
Figure 27. 4-band SST precision as a function of band centers.
Only the center of band number 12 changes.

This algorithm provide better atmospheric correction, and the sensor noise is not amplified. Table 5 shows the comparison of contributions to errors from sensor noise and atmospheric corrections.

Table 5. Comparisons of the 4-band SST Precision

Noise Model	NEDT (K)				Sensor Contribution to precision (K)	Atmosphere correction to precision (K)	Total Precision (K)
	3.75 μm band	4.005 μm band	10.8 μm band	12 μm band			
Noise Free	0.	0.	0.	0.	0.	0.18	0.18
Model 1	0.12	0.10	0.04	0.05	0.11	0.18	0.21
Model 2	0.14	0.12	0.06	0.07	0.15	0.18	0.23
Model 3	0.18	0.15	0.08	0.10	0.18	0.18	0.25

Raytheon

3.4.1.2 Sensor Noise's Effect

Radiosonde Data

The first investigation is to understand the traditional split window algorithm. An advantage of the split window algorithm is that the far-IR bands are almost unaffected by the solar radiation, and therefore can be used in both daytime and nighttime. Historically, the split window has been able to retrieve SST at a precision of about 0.5 K globally. This means approximately half of the global split-window SSTs have a precision worse than 0.5 K. We have performed retrievals on test data sets that have varying sensor noise, from 0 K to about 0.1 K. Figure 28 shows the results. The thick line is the threshold value. The results showed that the split window algorithm failed to meet the precision threshold for pixels with warm SST and large satellite zenith angles, even for the noise free case.

Figure 28. 2-band SST precision as function of satellite viewing angle and SST range.
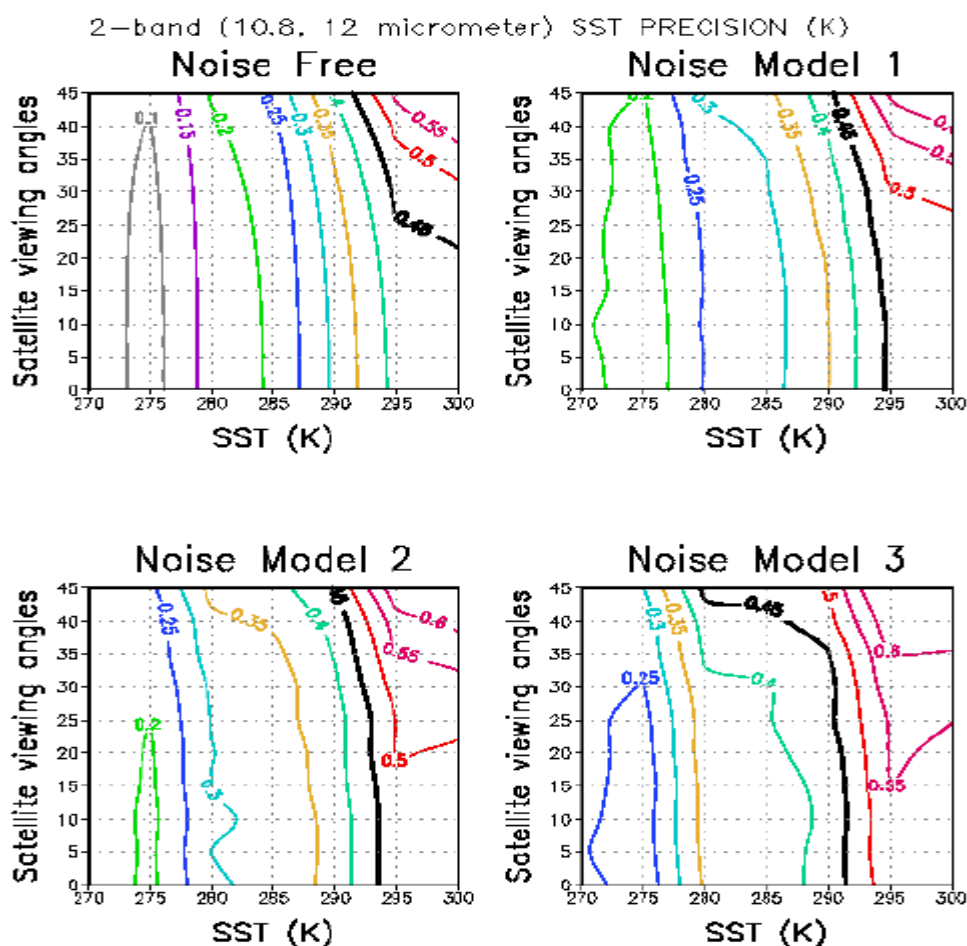
Attempts have been made to use water vapor information from sounding sensors on the same platform, as an additional source to retrieve SST (e.g., Emery *et al*., 1994). The purpose of this study is to optimize the use of the split window algorithm. The major issue is that the split window is unable to correct for the residual water vapor accurately. It is hoped that the added water vapor information may compensate the split-window deficit on water vapor correction. However, the error in water vapor retrieval is usually very large. Our testbed results indicated that the improvement of water vapor algorithm decreases as error in water vapor increases. A 10% water vapor error will offset all improvements.

Since the split window and water vapor algorithms are unable to meet the requirement, an additional band during daytime will be needed. The first consideration is the 8.55 μm band. This band is expected to improve the thin cirrus detection and also enhance the water vapor correction. This band is almost not affected by the solar radiation. However, the testbed results show little improvement when this band is added.

It is unlikely the SST retrieval will meet the threshold for all categories using only far-IR bands even if the sensor is near perfect.

The next step was to look at the SWIR bands. The atmosphere is transparent in the near-IR bands and may present a better correction for water vapor. Unfortunately, the mid-IR bands are contaminated by the solar radiation. Historically, the mid-IR bands are used to retrieve SST only at night.

In order to use a split window algorithm in the SWIR window, a solar radiation correction was implemented in the SST algorithm. The results are shown in Figure 29. The dual split window (3.75, 4.0, 10.8 and 12 μm) can significantly improve the retrieval. The results show that the dual split window algorithm may meet the threshold requirement at anytime, and over any range, with a few exceptions at the edge of scan for sensor model 3. As discussed in section 3.3.1, the SWIR bands, especially the 4.05 μm band, are not sensitive to atmospheric precipitable water. This explains why the quad algorithm outperformed the split window algorithm over tropical oceans.
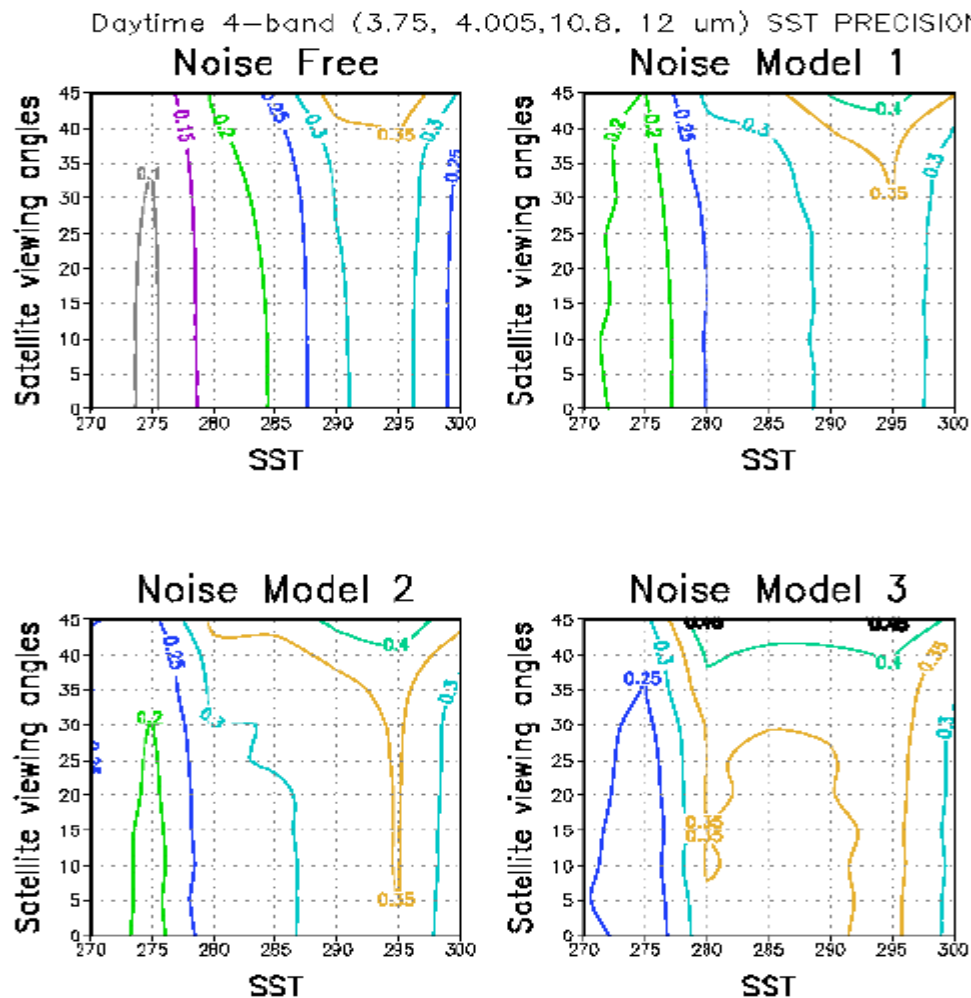
**Figure 29. 4-band (3.75, 4.005, 10.8, 12 μm) daytime SST precision
as function of satellite viewing angle and SST range.**

Global Data

The global data set includes atmospheric profiles and surface temperatures. This data set has only 17 levels of the atmosphere and the fields are smoothed. Less vertical structure may present a better SST precision in the algorithm.

Figure 30 shows the precision as a function of satellite viewing angles and temperature values for the two channel (10.8 and 12 μm) algorithm. The results are better than that derived from the radiosonde data set, although the algorithm still cannot meet the threshold for pixels with large satellite viewing angle and with sensor noise models 2 and 3.
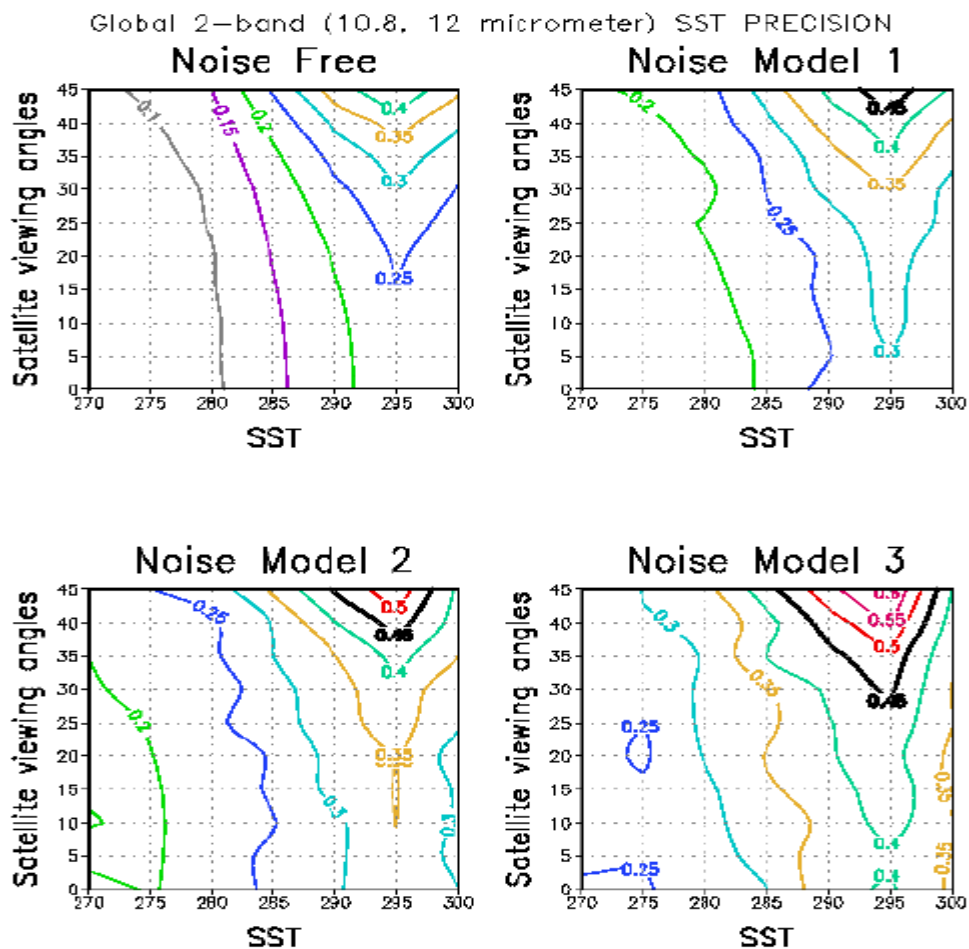
Figure 30. 2-band (10.8, 12 μm) SST precision as function of satellite viewing angle and SST range.

While the four-band algorithm may meet the threshold requirement with little margin left, the dual split window method exhibits much improved results (Figure 31). The precision is usually less than 0.3 K in the dual split window algorithm for sensor noise model 3.
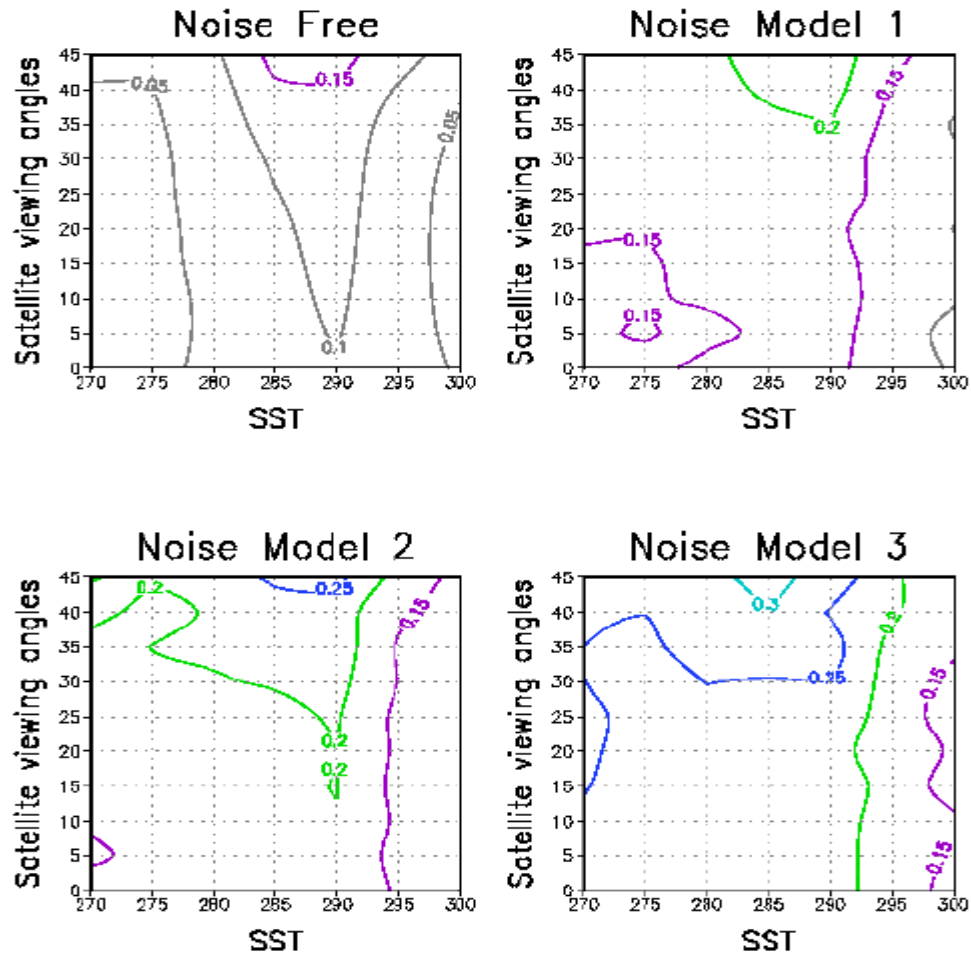
**Figure 31. 4-band (3.75, 4.005, 10.8, 12 μm) daytime SST precision
as function of satellite viewing angle and SST range.**

The solar correction using a split window in mid-IR seems effective in the algorithm. In both data sets, the results are much better compared to the use of only one mid-IR band in daytime. Figure 32 shows the nighttime dual split window results. The results are better than the daytime retrieval (Figure 31) but not substantially. The results are significantly better than the split window algorithm (Figure 30).
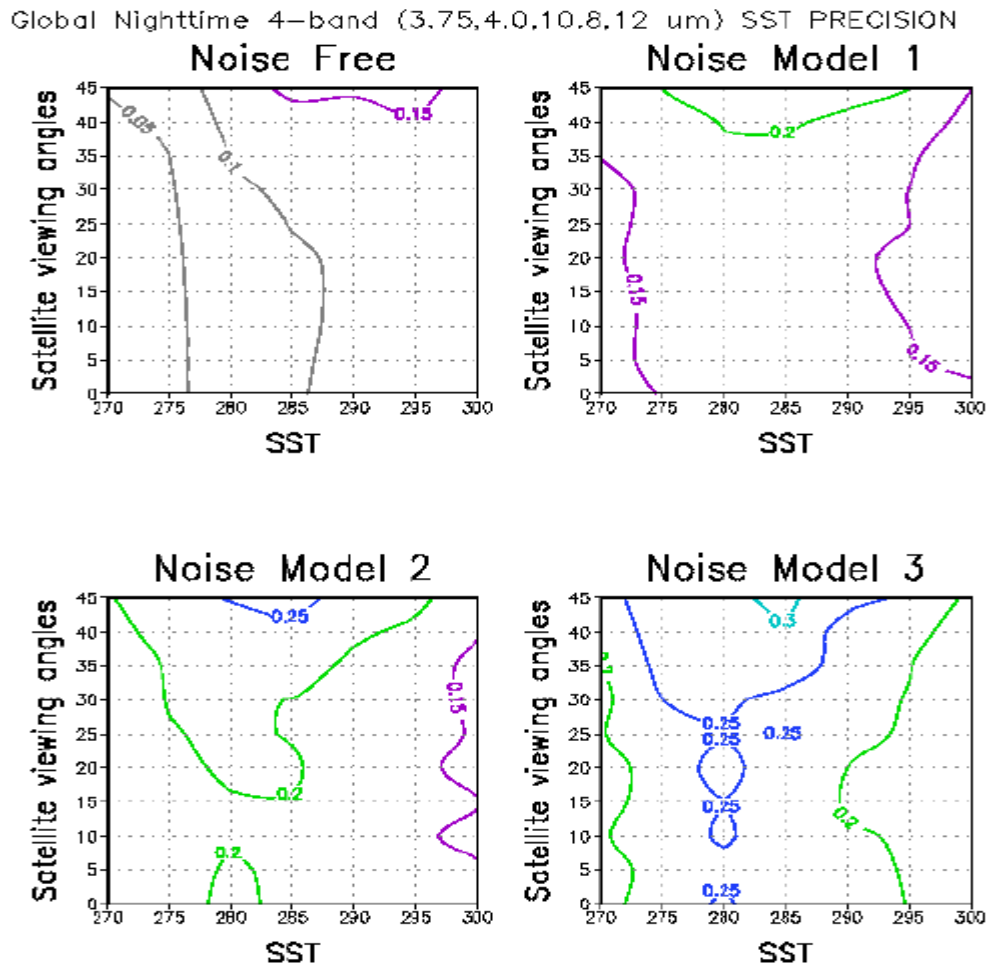
**Figure 32. 4-band (3.75, 4.005, 10.8, 12 μm) nighttime SST precision
as function of satellite viewing angle and SST range.**

3.4.1.3. Water Vapor effect

Figure 33 and 34 compared the SST retrieved error including precision, accuracy and uncertainty among the split window algorithm and VIIRS baseline dual split window algorithm. It was demonstrated that the SST precision is greater than the threshold 0.45 K if total column water vapor above 4.2 cm. However, the dual split window algorithm can meet the threshold at all total column water vapor range.
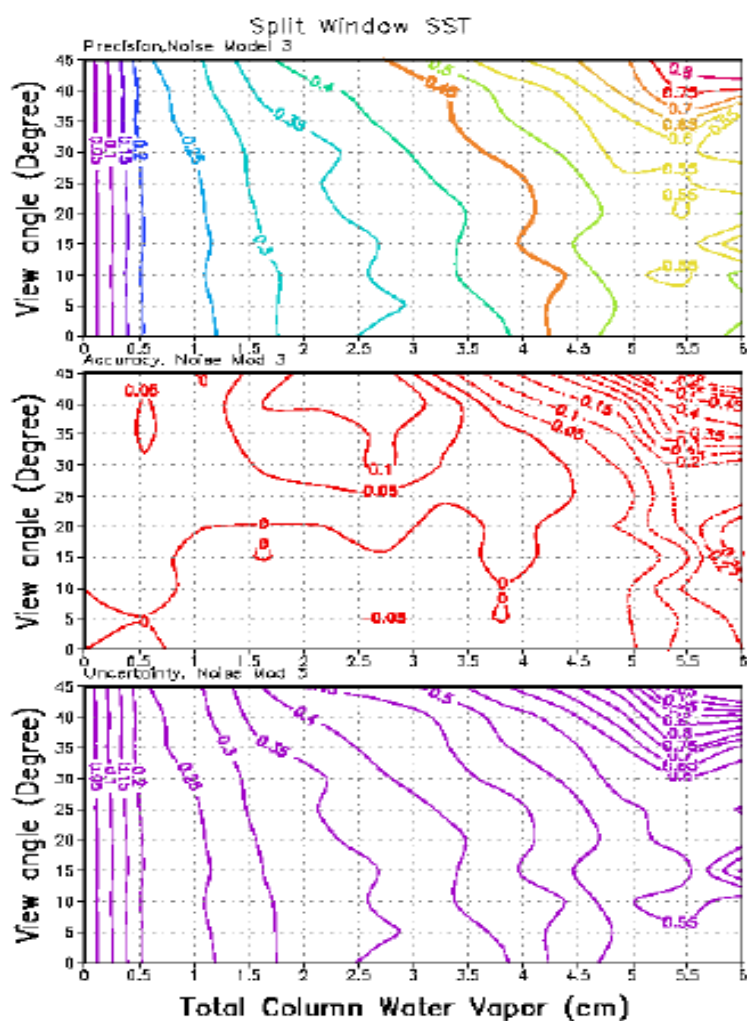
Figure 33. The SST retrieval error distribution vs. sensor viewing angle and total column water vapor for sensor noise model 3 from the split window algorithm. Upper Panel (Precision), Middle (Accuracy), Bottom (uncertainty).
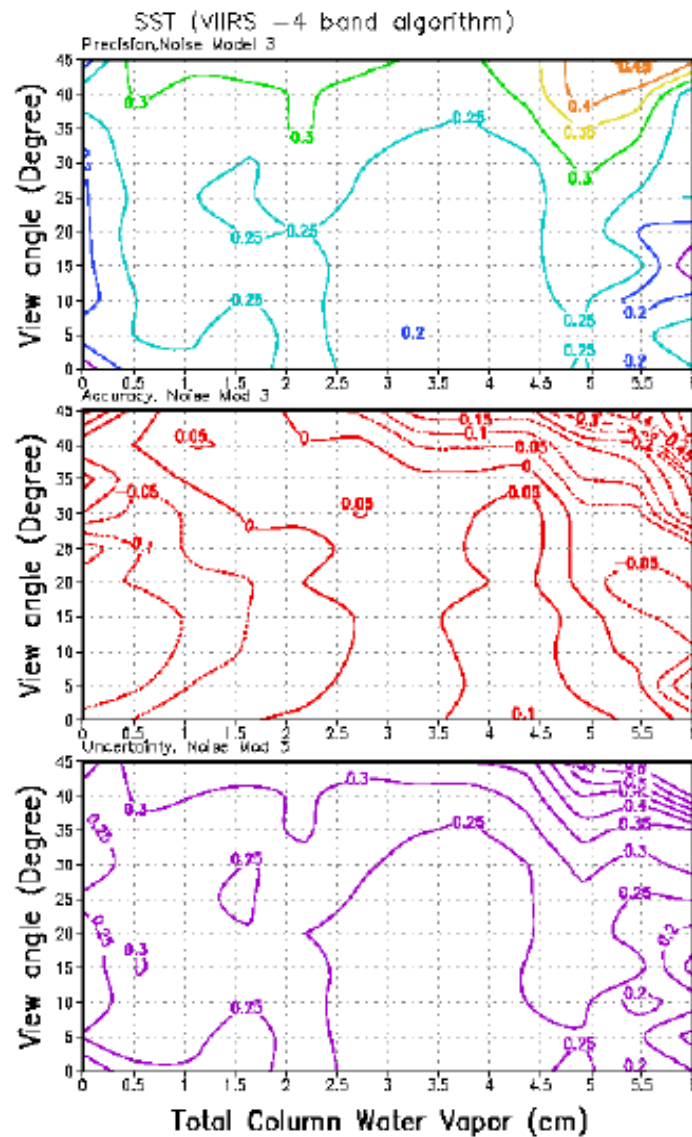
Figure 34. The SST retrieval error distribution vs. sensor viewing angle and total column water vapor for sensor noise model 3 from our baseline dual split window algorithm. Upper Panel (Precision), Middle (Accuracy), Bottom (uncertainty).

3.4.2 Calibration Errors

In order to investigate the algorithm accuracy requirement relevant to the mean radiometric error in the sensor, we added mean errors to the simulated radiances and performed the split-window algorithm and quad algorithm. Figure 35(a) shows the accuracy (split window) change with the mean error added to the radiance for each band. The data is from global observations. In order to meet the 0.2 K accuracy, the calibration error for the 11 and 12 micrometer bands needs to be less than 0.2 percent. However, if the error in the two bands are correlated, the requirement may be relaxed to 0.4%. Figure 35 (b) is similar to Figure 35 (a), but for quad algorithm. The conclusion is similar to the split window algorithm.

Split Window SST Accuracy v.s. Calibration errors
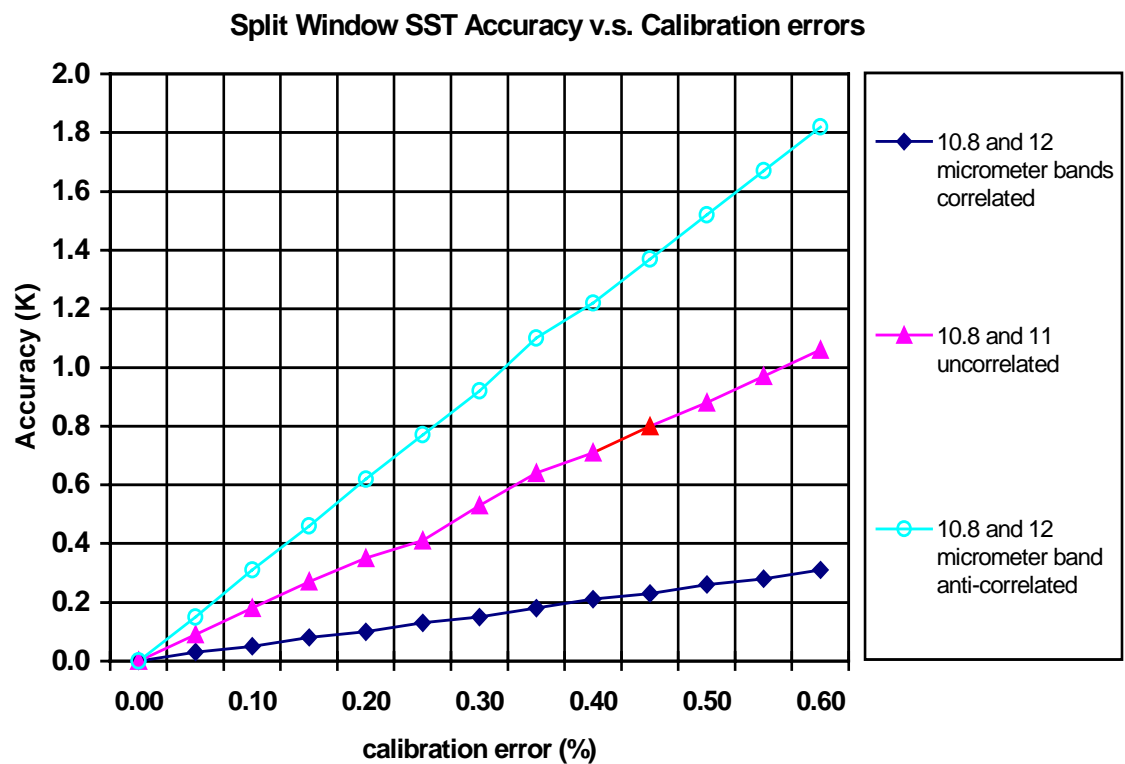
Figure 35a. Split window SST accuracy relevant to calibration error. There were 299 skin SST and atmospheric profiles used in this simulation. The original simulations were used as the training data set. The calibration errors were added to the original data set and the new data set was used as test data.

4-band SST Accuracy v.s. Calibration errors
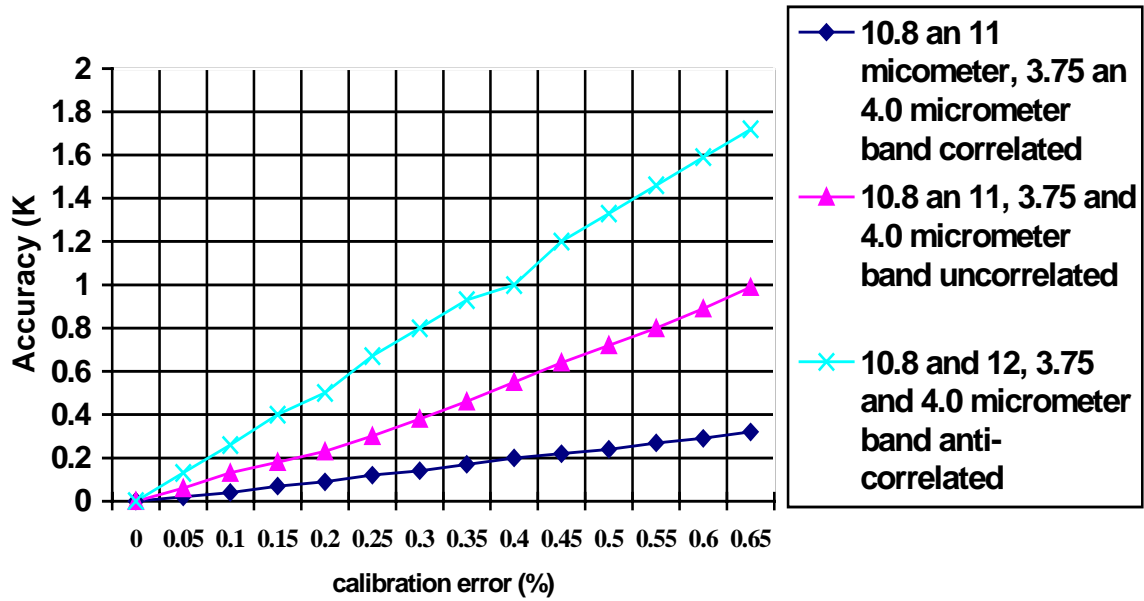
Figure 35b. Quad SST accuracy relevant to calibration error. There were 299 skin SST and atmospheric profiles used in this simulation. The original simulations were used as the training data set. The calibration errors were added to the original data set and the new data set was used as test data. b) quad algorithm.

Raytheon

The preliminary analysis of VIIRS radiance uncertainty was provided by J. Young at SBRS and G. Godden at PAI. Table 6 shows the fractional radiance uncertainty derived by Young and Table 7 shows the converted scene temperature uncertainty.

Table 6. VIIRS Fractional Radiance Uncertainty

Temp (K)	VIIRS Bands (µm)				
	3.75	4.005	8.55	10.8	12
260	.0083	.0071	.0046	.0031	.0031
270	.0079	.0067	.0045	.0031	.0031
280	.0074	.0064	.0044	.0031	.0031
290	.007	.0061	.0044	.0031	.0031
300	.0067	.0058	.0043	.003	.0031
310	.0064	.0055	.0043	.003	.003
320	.0061	.0053	.0043	.003	.003

Table 7. Scene Temperature Uncertainty

Temp (K)	VIIRS Bands (µm)				
	3.75	4.005	8.55	10.8	12
260	0.15	0.13	0.18	0.16	0.18
270	0.15	0.14	0.19	0.17	0.19
280	0.15	0.14	0.21	0.18	0.2
290	0.15	0.14	0.22	0.19	0.21
300	0.16	0.14	0.23	0.2	0.22
310	0.16	0.15	0.24	0.22	0.24
320	0.16	0.15	0.26	0.23	0.25

An example of Godden's analysis (for band 11, $\rho_{ev} = 0.01$) is shown in Figure 36. It indicates various error sources that contribute to the uncertainty of the VIIRS radiances, such as the variability of RVS (Response Versus Scan Angle), the band center, the black body temperature, etc. Figure 37 shows the variation of ρ_{ev} as a function of AOI for 10.8 µm band. The data set used in this test is NCEP global data set. One quarter of the data were used as training data, and the rest as testing data. The radiometric errors were added only to the test data. The viewing angles vary from -45° to 45°, corresponding to AOI from 25° to 65°.
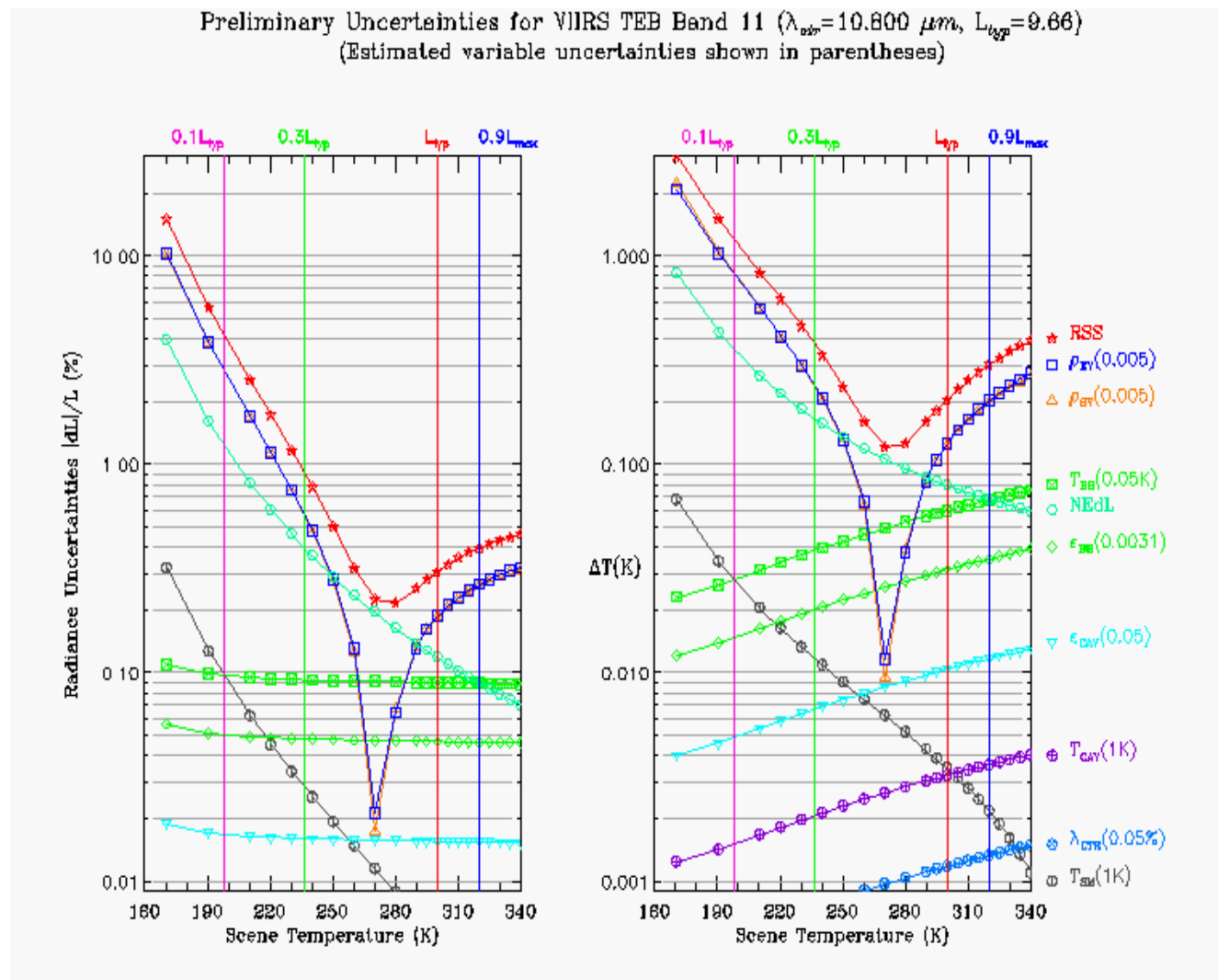
Figure 36. Uncertainties for VIIRS TEB Band 11.

RVS (%) vs AOI
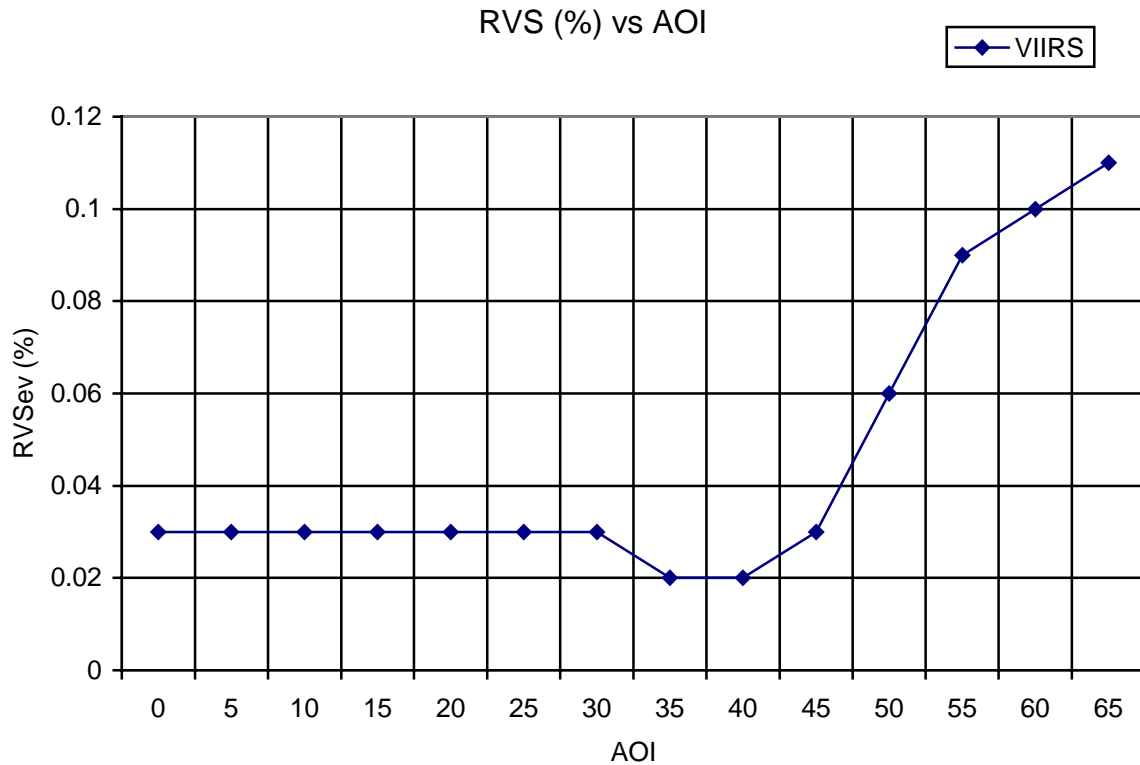
Figure 37 ρ_{ev} as a function of satellite viewing angle.

Results From Young's Data

Figure 38 shows the results of the daytime 4-band solution, assuming the radiometric errors for all bands are positively correlated. The upper panel is the SST accuracy due to the algorithm only. The middle panel shows the total accuracy error. For global data, the mean error is small. The accuracy is dominated by the sensor error. The lower panel is the sensor contribution. In this case, the sensor contribution to the SST accuracy averages 0.14-0.17 K. The requirement can be met for almost all SST ranges. The sensor contribution does not vary with satellite viewing angle since there is no AOI dependent information in Young's data.
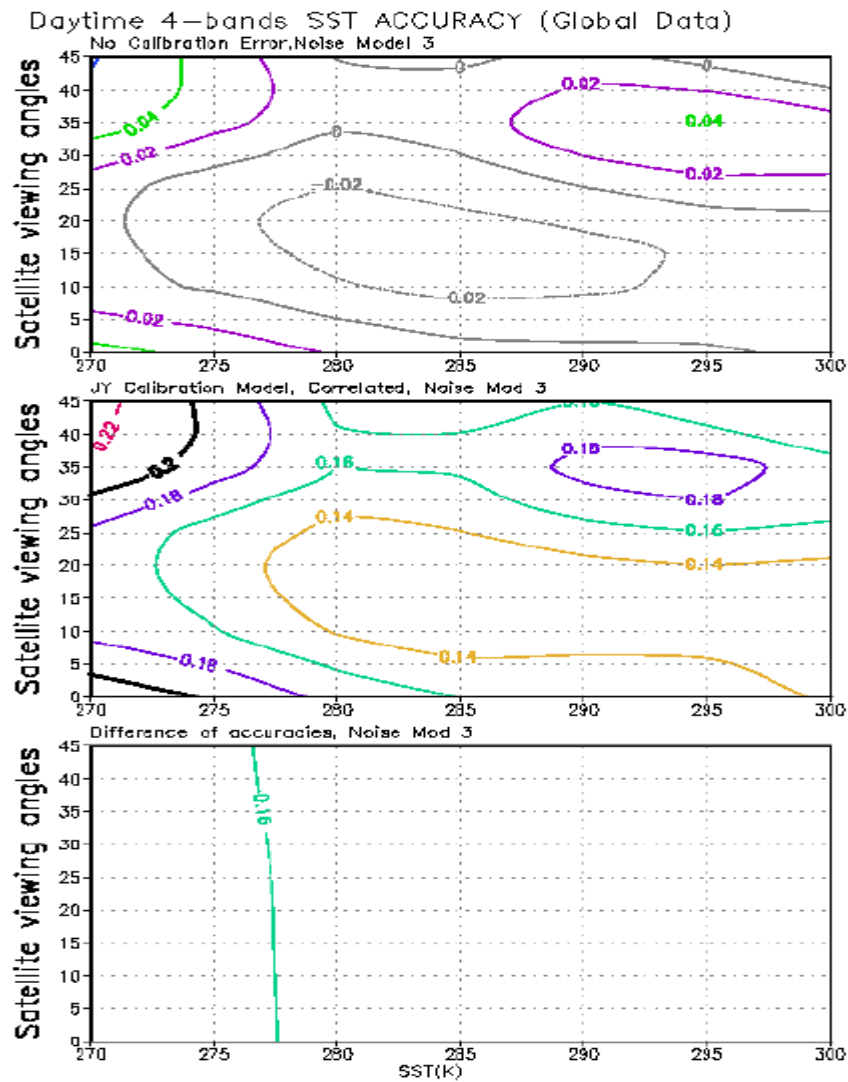
**Figure 38. 4-band SST accuracy derived from Young's flowdown
results, assuming errors for all bands are correlated.**

Figure 39 shows the 4-band daytime SST accuracy, assuming the errors for all bands are not correlated. It indicates that the sensor failed to meet the 0.2 K accuracy requirement for the lower SST fields.
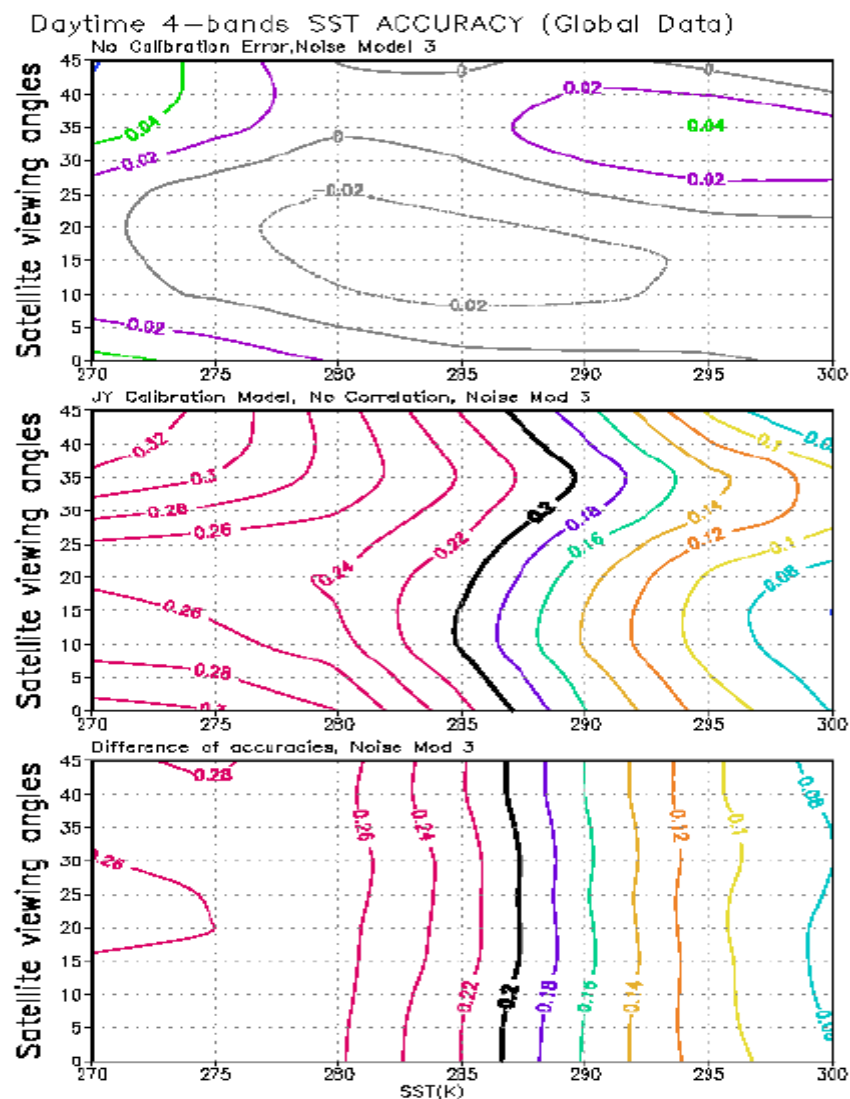
**Figure 39. 4-band SST accuracy derived from Young's
flowdown results, assuming errors for all bands are not correlated.**

Figure 40 shows the results of the daytime 2-band solution, assuming the radiometric error for all bands are positively correlated. In this case, the sensor contribution is < 0.17 K. However, the overall errors over some particular areas are larger than 0.2 K.
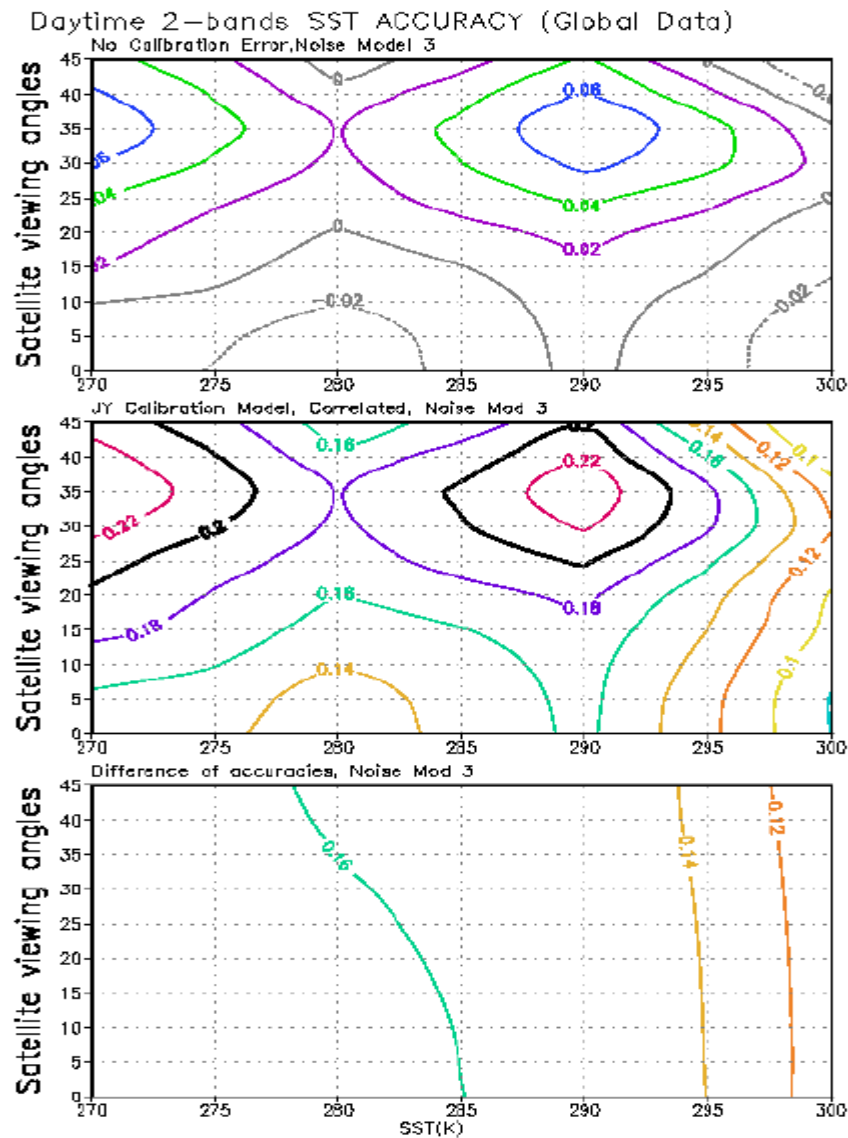
**Figure 40. 2-band SST accuracy derived from Young's
flowdown results, assuming errors for all bands are correlated.**

Figure 41 shows the 2-band daytime SST accuracy, assuming the errors for all bands are not correlated. It indicates that the sensor failed to meet the 0.2 K accuracy requirement for all SST ranges.
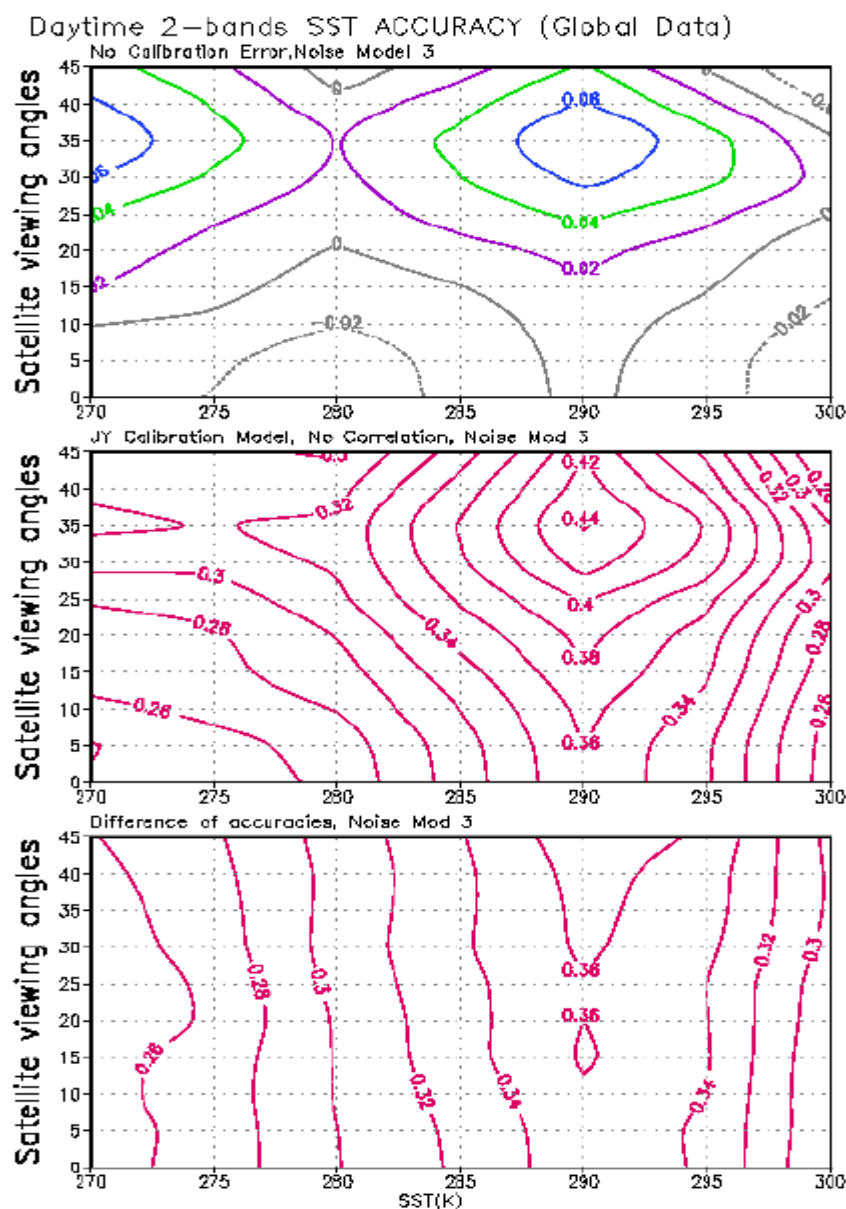
Figure 41. 2-band SST accuracy derived from Young's flowdown results, assuming errors for all bands are not correlated.

SST accuracy from split window algorithm
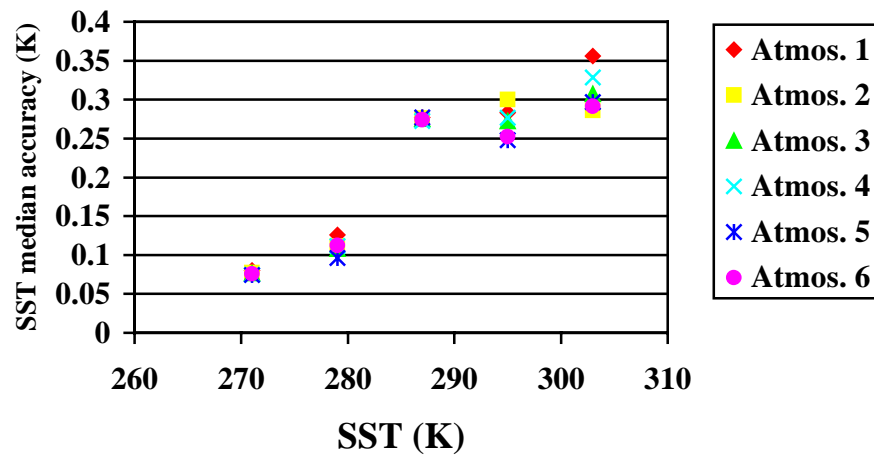
SST accuracy from 4 -bands algorithm
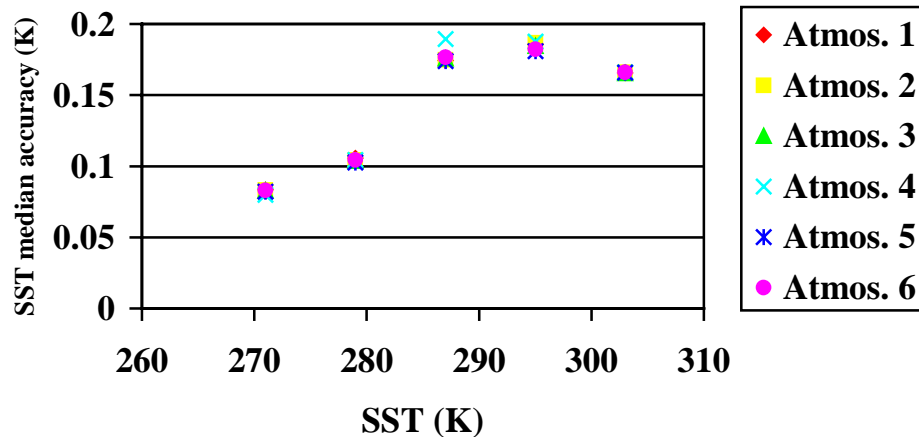
Figure 42. SST rms accuracy from SBRS 32 perturbation

Figure 42 shows the SST retrieval rms accuracy from SBRS 192 calibration perturbation models to the five typical SST at six different atmospheric conditions. Because the retrieved SST bias from random calibration perturbation models may cancel each other, the absolute bias are taken to be averaged as rms accuracy. It is shown that at warmer temperature above 285K, the accuracy from split window algorithm is greater than our specification 0.2K, while the accuracy from our baseline algorithm can be less than 0.2K at all temperature range, even though the error is higher at warmer temperature.

Raytheon
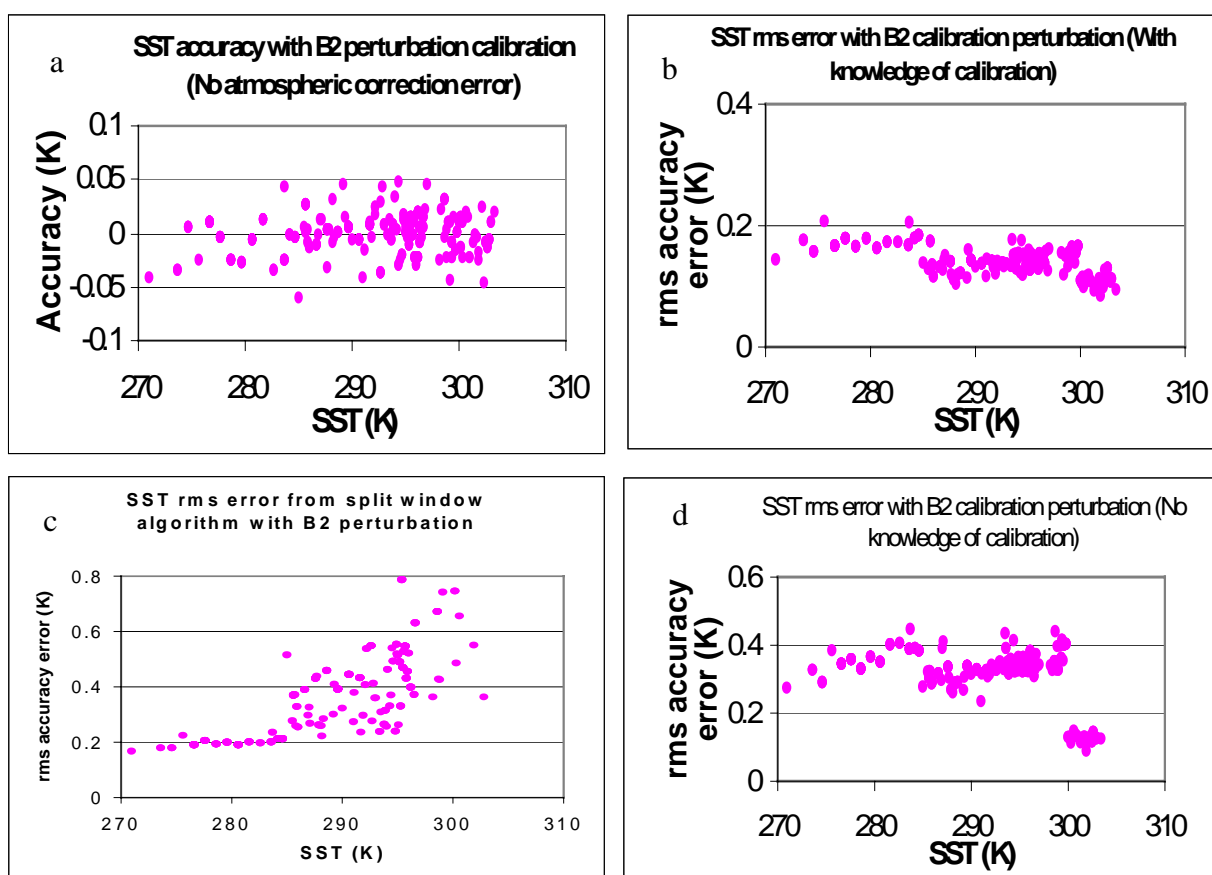
Figure 43. SST rms accuracy (a), accuracy (b) with knowledge of calibration from baseline four-band algorithm, rms accuracy with knowledge of calibration from split window algorithm (c), and rms accuracy without knowledge of calibration from baseline algorithm (d)

In order to test calibration models, Jim Young at SBRS performed random calibration perturbation to 305 profile radiosonde data with solar zenith angle changes from 10 to 60 degree (daytime) and viewing zenith angle changes from 0 to 45 degree. There are a total of 15250 calibration perturbations. The retrieved SST accuracy is shown in figure 43. It shows that the accuracy from our baseline algorithm with knowledge of calibration was only between –0.05 K to 0.05K(figure 43a). This is because random calibration error may cancel each other. The rms accuracy is about 0.17 K (see figure 43b), below the original CAIV target 0.2K. This result is under the condition that the calibration perturbation is known in advance. Even under this condition, the rms accuracy error from the split window algorithm is much larger than 0.2 K at warmer temperature (figure 43c). These results indicate the importance of selecting good algorithms. However, if we don't know the calibration perturbation in advance, the rms accuracy error is above 0.2 K in general (figure 43d).

3.4.3   Band-to-band registration and MTF

Figure 44 shows the influence of band-to-band registration on the algorithm precision. The mis-registration has significant impact on the retrieval precision when the noise is small. When the

sensor noise increases, the influence of band-to-band registration becomes less important. Therefore, the band-to-band registration may not be a critical issue for SST retrieval, especially for the open ocean area where the SST gradient is smaller than that for the off-Florida scene.

Split Window SST Precision
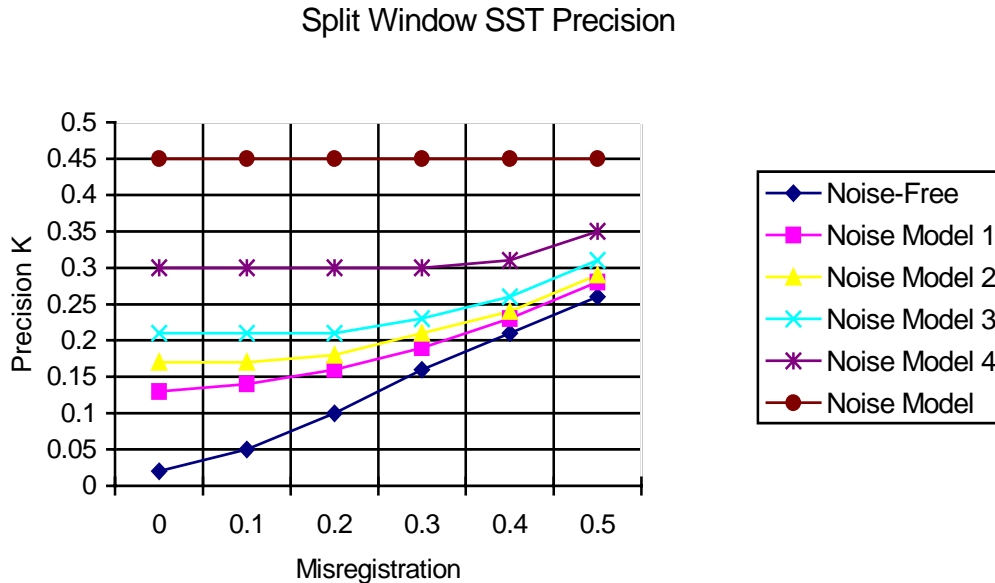
Figure 44. SST precision relevant to band-to-band registration. The misregistration ranges from 0.0 to 0.5 of the pixel area.

Two 1.3-km resolution AVHRR nadir scenes were chosen as SST MTF/band-to-band registration test sides. The VIIRS TOA radiances of all VIIRS thermal bands were simulated using radiative transfer model. Only one atmosphere was used in each scene. Therefore the atmospheric correction is near perfect. The data were interpolated into 450 m resolution and a 9-point smoothing was performed to all the data to eliminate the noise. Figure 45(a) shows the SST contour plots of scene I (open ocean). Figure 45(b) shows the SST contour plots of scene II (Gulf Stream Scene). Seven SBRS MTF models were applied to both scenes. The ground sampling distances vary from 150 m to 1250 m. The HCS is 1.3 km. The tests of band-to-band registration were performed at GSD level. The data were re-sampled to HCS for all GSDs after MTF models were performed.
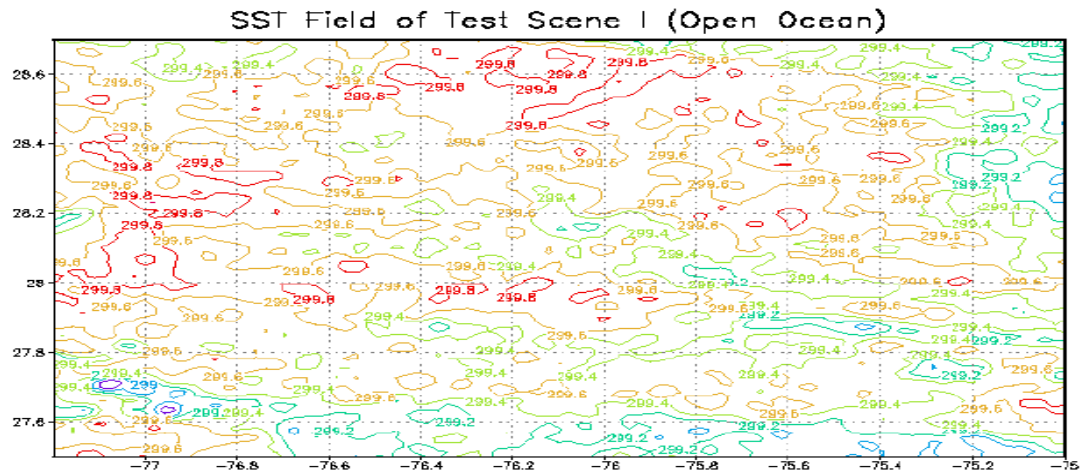
Figure 45a. SST fields of Test Scene I (Open Ocean Scene).
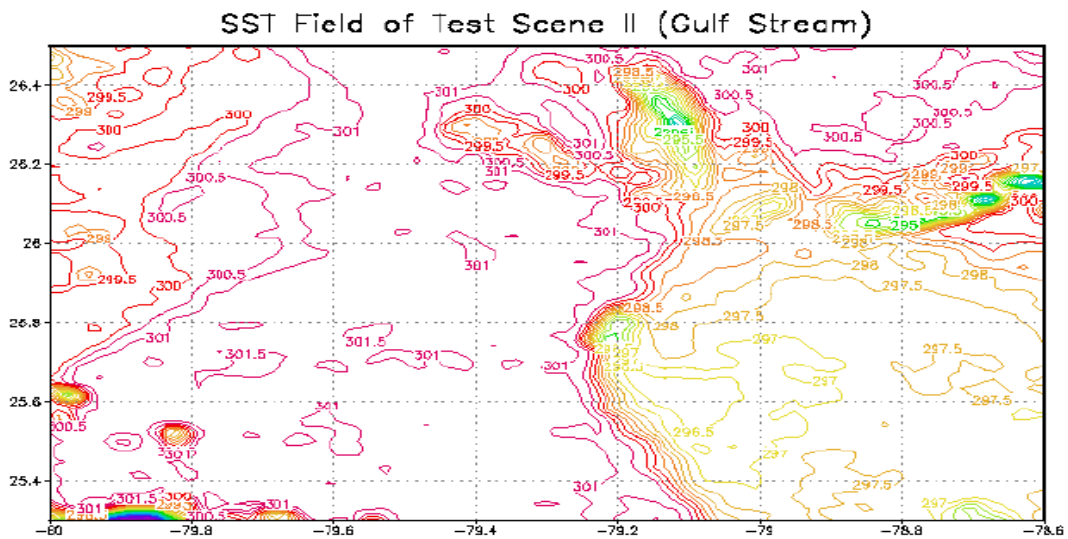
Figure 45b. SST fields of Test Scene II (Gulf Stream off Florida).

Figure 46 shows the 4-band SST precision of the open ocean scene derived from the seven MTF Models. The error is smaller than 0.015 K. The SST EDR threshold precision requirement is 0.45 K. Therefore, for open ocean, the MTF effect may not be important.

SST Precision vs MTF (SCENE I)
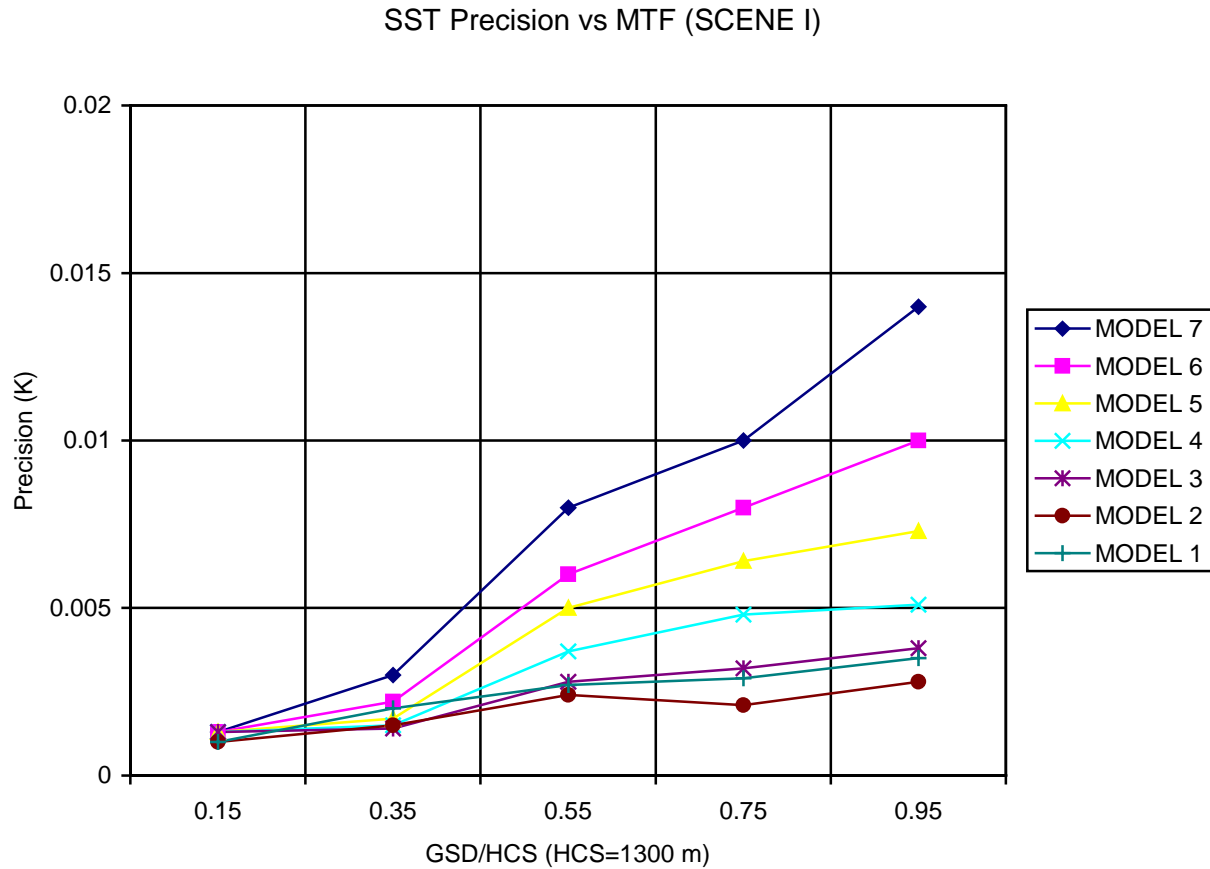
Figure 46. MTF results from open ocean scene.

Figure 47 shows MTF results from the Gulf Stream Scene. The maximum error is 0.05 K for Model 7, the model with the worst noise. This is about half of the NEDT value for band 11. To reduce the MTF effects, models better than model 6 should be adopted for GSD < 600 m.
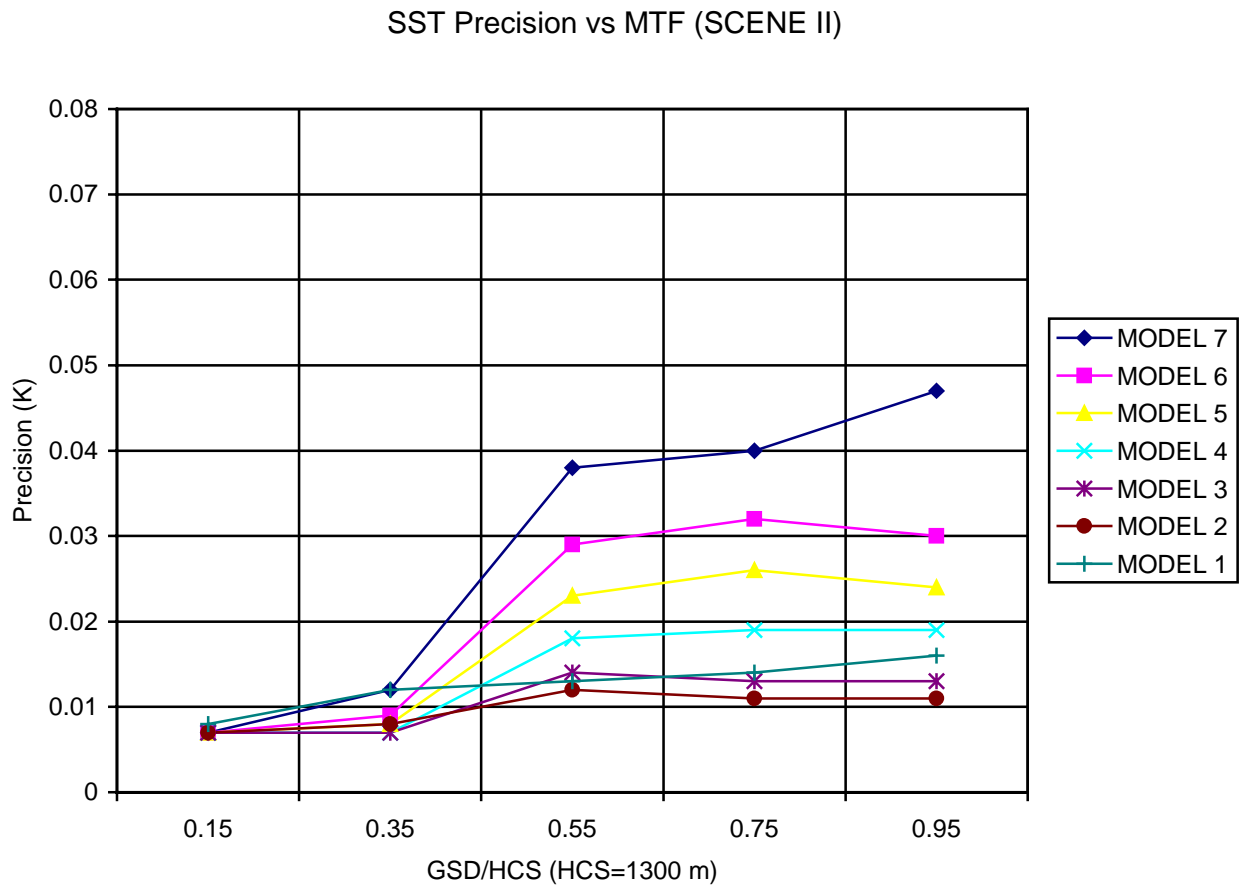
Figure 47. Four-band solution from Gulf Stream Scene.

Figure 48 shows the 2-band MTF results from the Gulf Stream Scene. The results do not substantially differ from the 5-band solution. In this case, the atmospheric correction is near perfectly corrected for both the 2-band and 4-band algorithms.

SST Precision vs MTF (SCENE II)
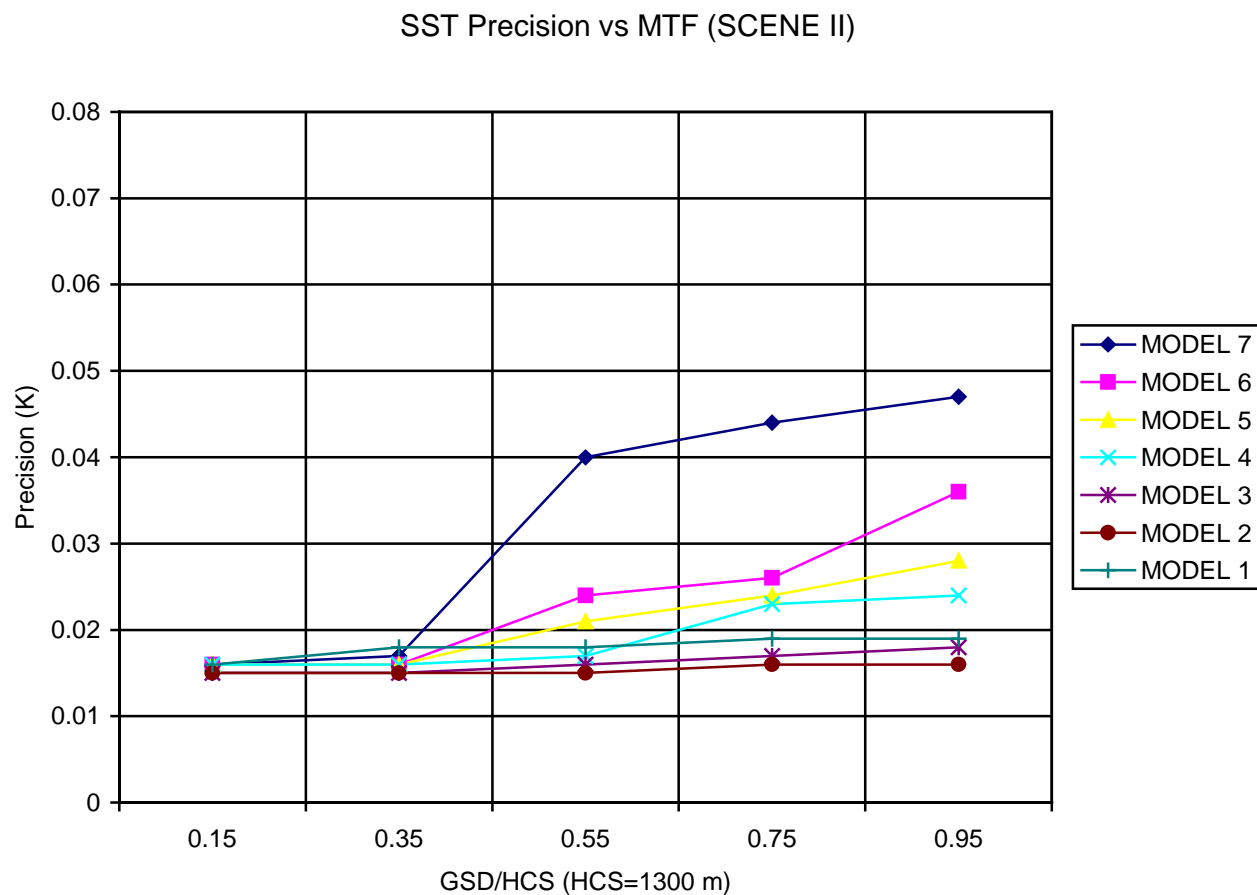
Figure 48. Two-band solution from Gulf Stream Scene.

Raytheon

Figure 49 shows the combined effects of band-to-band registration and MTF effects for the open ocean Scene. The MTF model is SBRS Model 3. The precision at worst case (GSD=HCS, misregistration =50%) is about 0.02 K. The precision is about 0.01 K at GSD/HCS ratio of 0.6 and misregistration of 35%. This result indicates that the open ocean SST does not drive band-to-band registration, not GSD/HCS ratio.
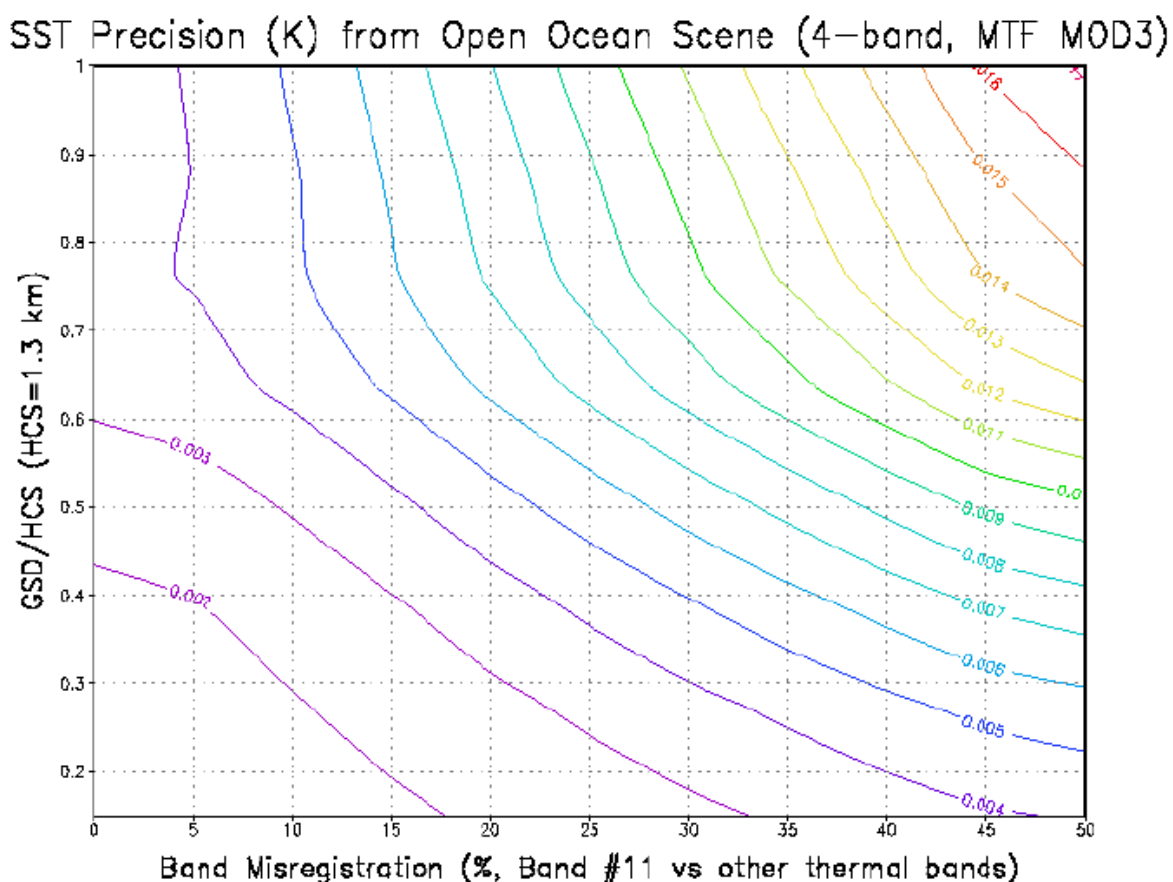
**Figure 49. The combined effects of band-to-band registration
and MTF on 4-band SST algorithm for open ocean scene.**

Figure 50 shows the combined effects of band-to-band registration and MTF effects for the Gulf Stream Scene. The MTF model is SBRS Model 3. The results show that the precision vary from 0.02 K to 0.3 K within a misregistration range of 0% to 50%. The effect of larger misregistration (> 30%) and large GSD/HCS (> 0.6) is significant compared to the total error budget of about 0.3 K for the 5-band solution. The precision is 0.12 K at GSD/HCS=0.6 and misregistration of 30%. The SST error budget for band-to-band registration and MTF effects is 0.1-0.15 K. Therefore, the sensor should meet a minimum requirement for GSD/HCS<0.6 and misregistration < 35%.
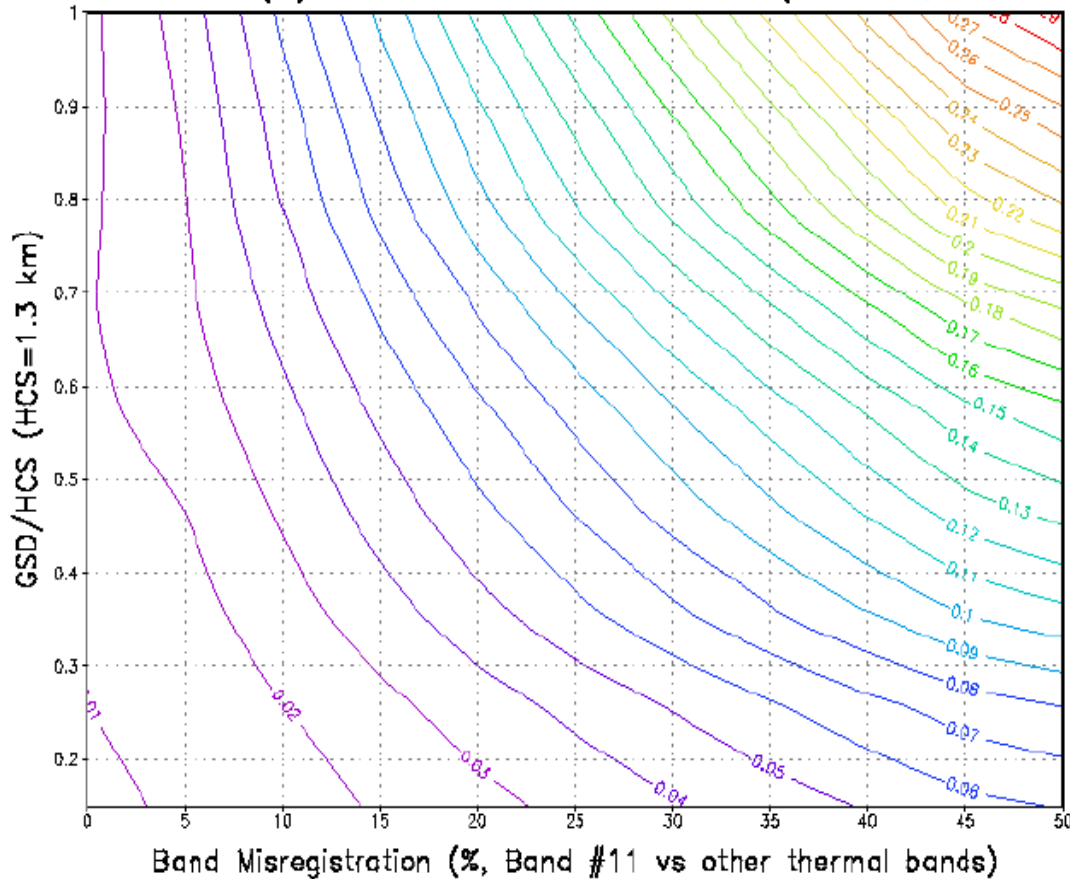
Figure 50. The combined effects of band-to-band registration and MTF on 5-band SST algorithm for Gulf Stream scene.

Figure 51 shows the combined effects of band-to-band registration and MTF effects for the Gulf Stream Scene from the 2-band algorithm. The MTF model is SBRS Model 3. The precision is better for the cases with large misregistration and GSD/HCS ratio.
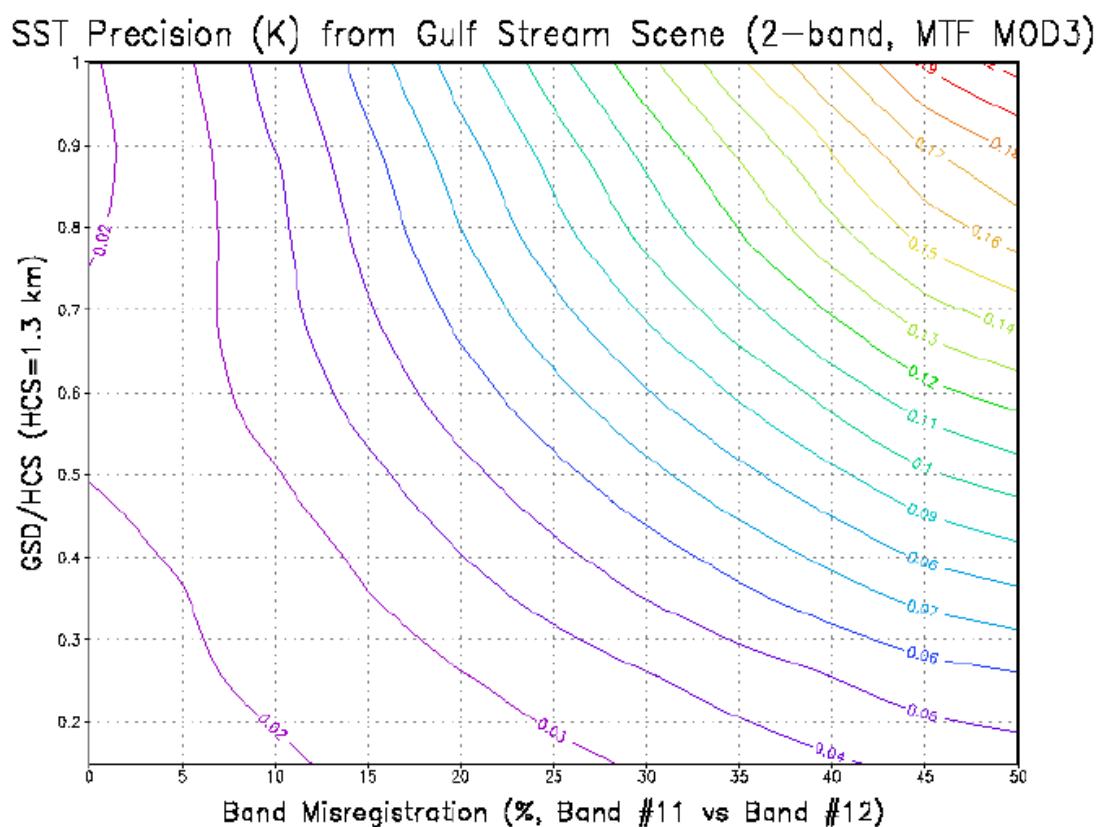
Figure 51. The combined effects of band-to-band registration and MTF on 2-band SST algorithm for Gulf Stream scene.

3.4.4   Aerosol's effect

Aerosols present another problem for SST retrieval. This problem has been discussed by McClain (1985), Griggs (1985), May *et al*. (1992) and others. The basic method in these studies was to find an empirical equation that relates the aerosol optical thickness to the SST change in the retrieval and to correct this change to get a more realistic SST. May *et al*. (1992) found that the correction is well correlated with $\tau\sec(\theta)$, where τ is the optical thickness and θ is the satellite zenith angle. This section evaluates the error contribution due to volcanic eruption. The data used are from MODTRAN simulations using 225 skin SSTs and atmospheric profiles. For each skin SST, we made 225 simulation for 9 satellite zenith angles, 5 solar zenith angles, and 5 aerosol optical thickness values. These simulations were used to establish the relationship between brightness temperatures and aerosol thickness as well as zenith angles. Following the paper by May *et al* (1992), the SST change is linearly related to $\tau\sec(\theta)$. In this work, we assume the change of brightness temperatures are linearly related to $\tau\sec(\theta)$, i.e.

$$T_b = a\, T_{ba} + b\tau\sec(\theta) \tag{27}$$

Where T_{ba} is the brightness temperature when aerosol exits, T_b is the corrected brightness temperature.

The coefficients, a=1.00028,1.00054,1.00050,1.00033 and b=-4.4802, -0.4999, 2.6219, 1.6194 for the four channels in daytime, are derived from training data set for each bands.

The procedure is as follows: calculate brightness temperature for each band, using above equation to correct brightness temperature, using SST algorithm to perform retrieval.

Figure 52 shows three results from the duel split window SST algorithm. The red line shows the accuracy of SST retrieval without correction. The accuracy is ~0.4 K when τ= 0.4 and ~2.2 K at τ=0.8. This indicates that small change of optical thickness will introduce large SST error if without correction. Purple line indicate perfect correction, i.e. the optical thickness in testing data is the same as those in training data. The green line shows the results from our current algorithm described above. The blue line shows the results using SST correction method adopted from may *et al* (1992). The mean bias was almost removed out using both correction methods.
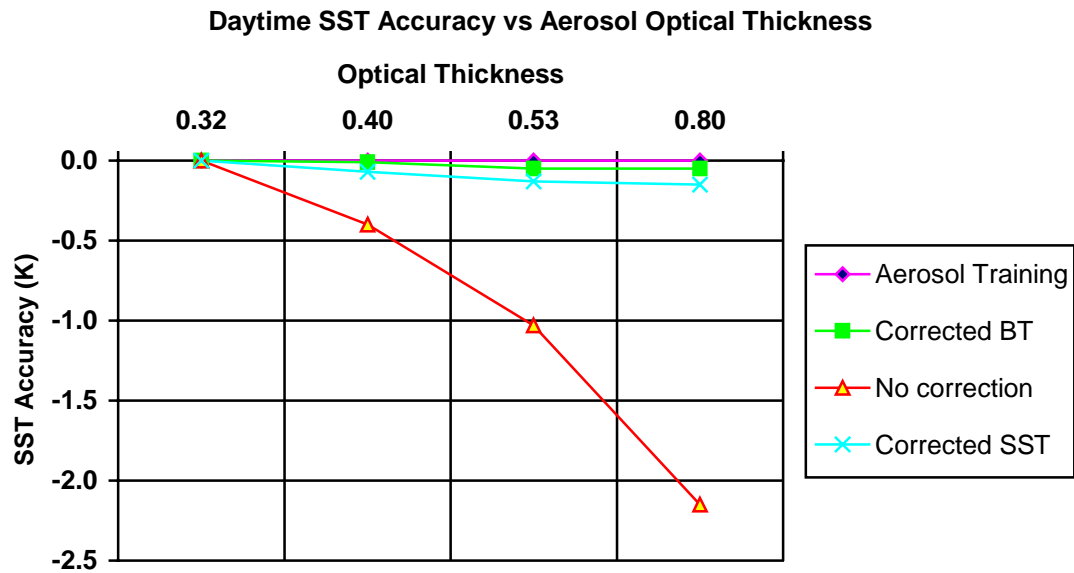
Figure 52a. Daytime SST accuracy as a function of optical thickness in testing data
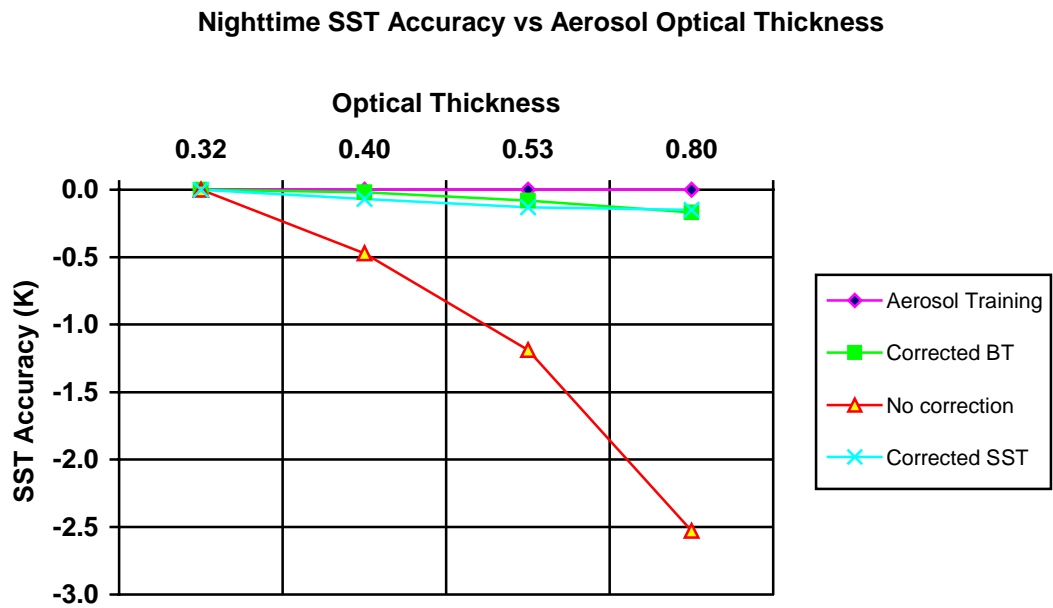
Figure 52b. Nighttime SST accuracy as a function of optical thickness in testing data.

Figure 52 (b) shows the nighttme SST accuracy. Figure 53 shows the precision as a function of optical thickness. The error increases when optical thickness becomes larger even for perfect correction. Using brightness temperature correction method, the error can be reduced to the threshold value (0.45K) when optical thickness is less than 0.53.
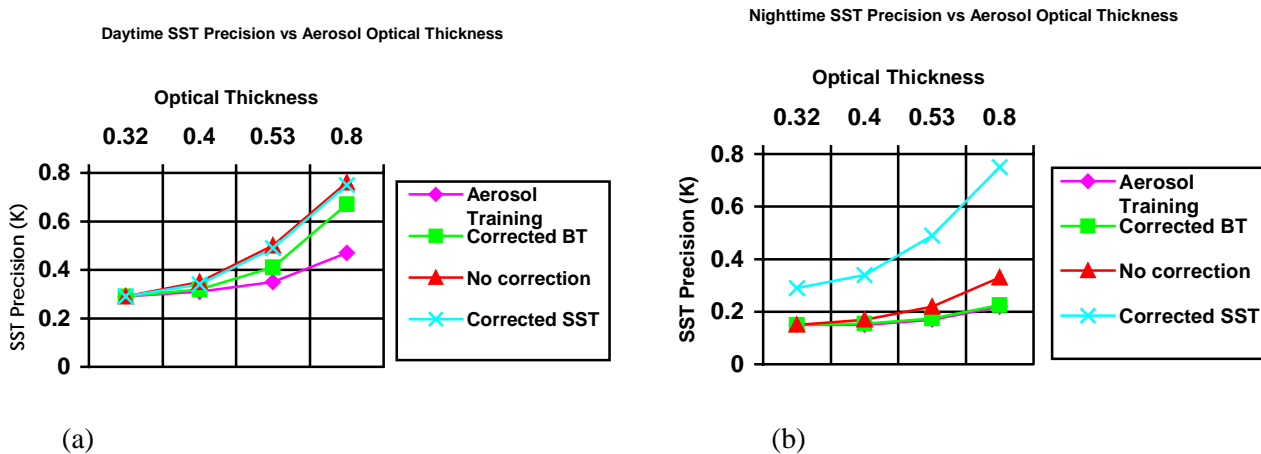
Figure 53. (a) SST precision as a function of aerosol optical thickness. (b) Nighttime SST precision as a function of aerosol optical thickness.

Figure 53 (b) is the nighttime SST precision. The aerosol does not cause large precision error during nighttime.

In above figures, the aerosol height and type do not very. If these parameter change, the error budget can be different. Figure 54 shows the SST accuracy as a function of aerosol optical thickness in two cases. 1. Aerosol concentrated between 0-4 km height, 2. Aerosol concentrated between 4-8 km but the aerosol type is the same as in case 1, The results show that, if only aerosol height changes, the error does not increase significantly. However, if aerosol type changes, the results may be different. The aerosol correction algorithm may need to be developed not only as a function of optical thickness, but also a function of aerosol types. Both aerosol thickness and type can be obtained from NPOESS aerosol algorithms.
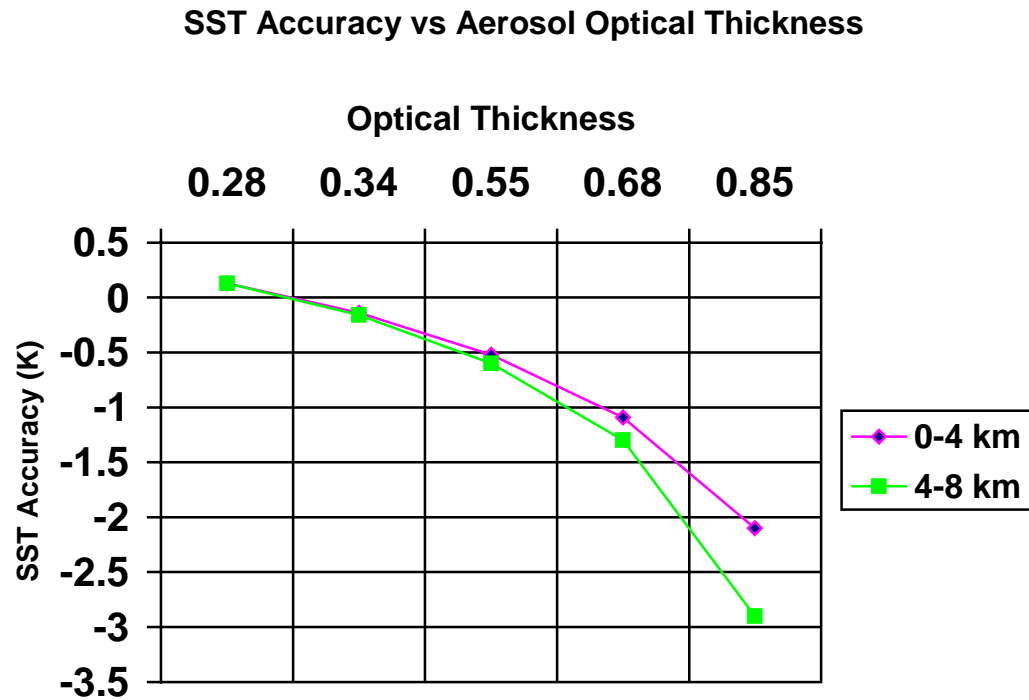
Figure 54 SST accuracy as a function of optical thickness and aerosol heights.

In order to consider the effect of aerosol type in addition to aerosol optical thickness' effect, simulation was performed with NCEP July 1998 reanalyzed data, with four aerosol types specified as rural, urban, maritime, and desert. The aerosol optical thickness is from NESDIS data, derived from the AVHRR data. Figure 55 (a) shows the aerosol optical thickness distribution. 55(b) shows the retrieved SST bias without aerosol correction, 55(c) is the bias distribution after aerosol correction to the brightness temperature, 55(d) shows the bias distribution after perfect correction. SST bias are as large as -0.8K without correction. However, the large bias are reduced significantly after correction (see figure 54 c).
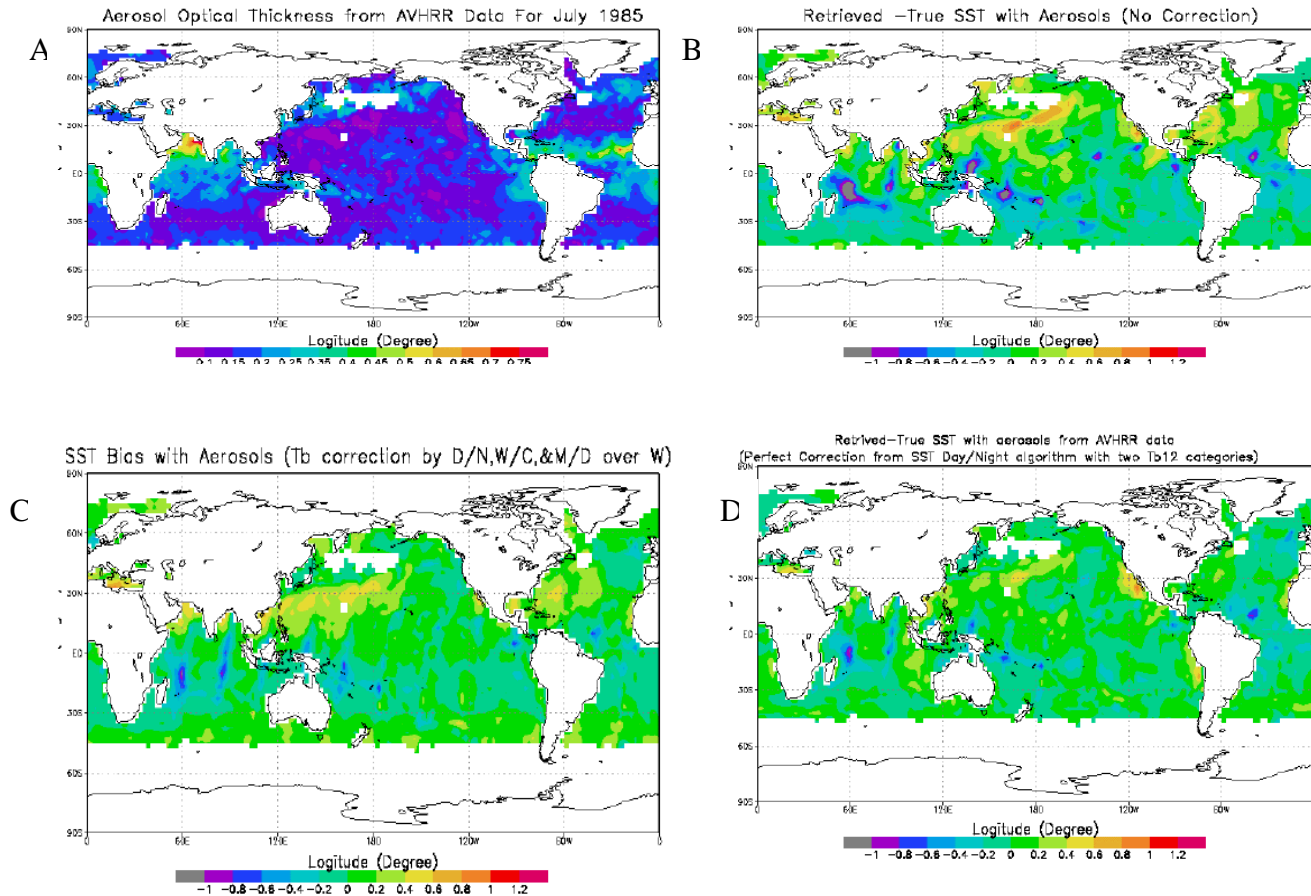
Figure 55 (a) Aerosol optical thickness distribution. (b) Retrieved SST bias without aerosol correction. (c) SST bias after aerosol correction to brightness temperature. (d) SST bias after aerosol correction.

Following a suggestion of Dr. Larry Stow of NOAA, we investigated the effect of aerosol types on SST retrieval in addition to the optical thickness. We put four aerosol types as rural, urban, maritime and desert into the simulation. The SST bias was shown as Figure 56(b). The cloud type in the simulation was shown in figure 56(a), there were five clouds including 1) cumulus, 2) altostratus, 3) stratus, 4) stratus/stratocumulus, and 5) nimbostratus. Figure 56(b) shows that if the effects of aerosol type are not considered, the SST precision error can be as large as 0.9K and the accuracy error can be as large as –0.8 K. After considering the effect of aerosol type, a precision of 0.22K can be obtained and the accuracy error is reduced to < 0.1 K with a few exceptions.

A

Cloud distribution for the simulation

B   C

SST Bias with Aerosols (without correction to the aerosol type)   SST Bias with Aerosols (with correction to the aerosol type)
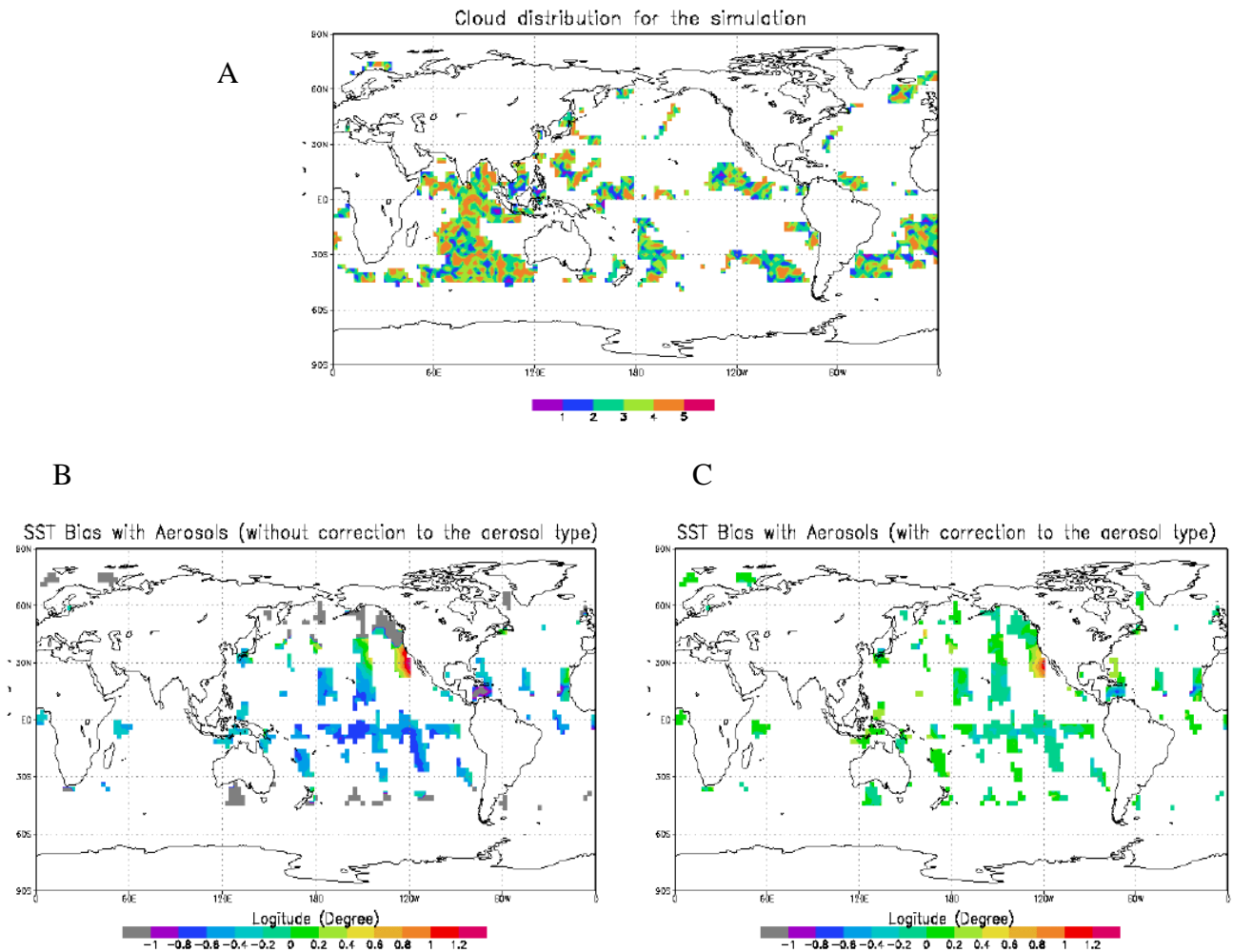
Figure 56 (a) Cloud type distribution in the simulation. (b) SST bias without the consideration of aerosol type. (c) After correction to both of aerosol optical thickness and the aerosol type

3.4.5   Thin or Sub-visible Cirrus Cloud

The VIIRS SST retrieval is required under clear sky condition only. However, under some circumstances, such as thin cirrus, cloud mixed pixels, and volcanic aerosols, it is difficult to determine whether pixels are 'clear' or not. This section evaluates the errors introduced by these factors and discusses the possible solution to reduce these errors. The results are for the nadir view only. Sensor contributors, such as sensor noise, calibration, and band-to-band registration, are not considered.

Figure 57a shows the transmittance of thin cirrus vs. band wavelength at different optical thickness. For thin cirrus, the optical thickness is less than 0.05 and the the transmittance is usually above 0.90. Therefore, much of the surface information is retrievable. But at optical thickness 0.05, thin cirrus can cause SST bias up to a few degrees (see figure 57b) and certain corrections are needed
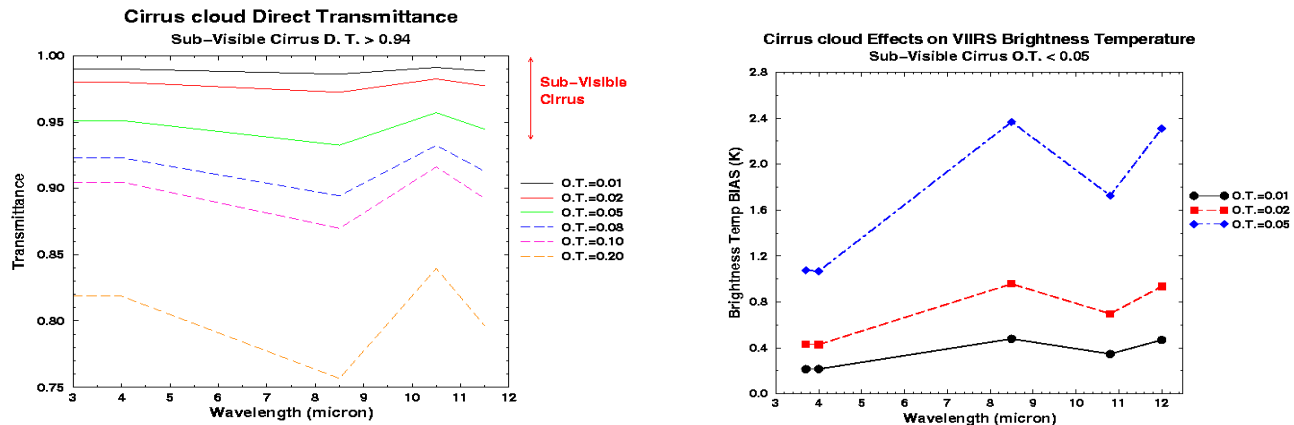
Figure 57 (a) Transmittance vs. band wavelength for cirrus at different optical thickness. (b) The brightness temperature bias cause by thin cirrus vs. band wavelength at different optical thickness

Figure 58(a) shows the brightness temperatures (BT) of the 5 VIIRS thermal bands as functions of optical thickness in daytime at 10° solar zenith angle. The skin SST is 295 K. BTs of far-IR bands decrease as the optical thickness increases. However, the rate of decreasing is different for different bands. The BT of 8.55 μm decreases slower than the 12 μm band and becomes higher than BTs of 12 μm from optical thickness of about 0.025. In daytime, the BTs at 3.75 μm and 4.005 μm do not decrease as optical thickness increases due to the increased solar radiation. The different behavior of each band provides the possibility to detect thin cirrus at certain optical thickness levels and improve the SST retrieval accuracy. It also will provide the possibility to correct the bias for small optical thickness.

Figure 58(b) is similar to Figure 58(a) except that the skin SST is 271 K. The differences between bands are more significant compared to Figure 58(a).
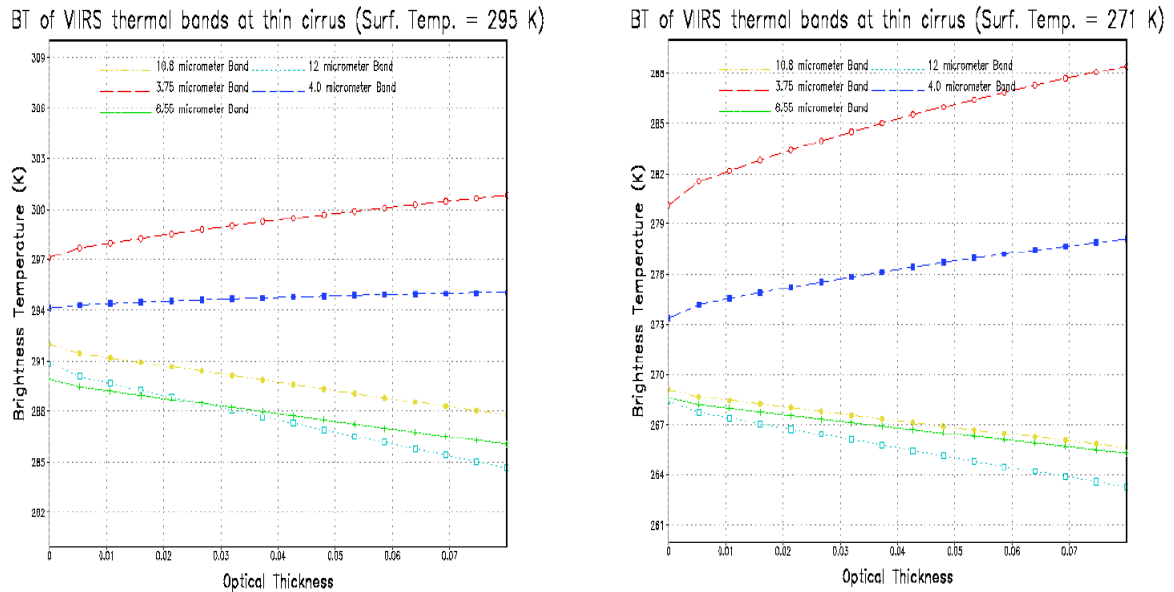
Figure 58 (a). Brightness temperatures of 5 VIIRS thermal bands as functions of optical thickness of thin cirrus. The solar zenith angle is 10°. The surface skin temperature is 295 K. (b) Brightness temperatures of 5 VIIRS thermal bands as functions of optical thickness of thin cirrus. The solar zenith angle is 10°. The surface skin temperature is 271 K.

Figure 59 shows the SST uncertainty, accuracy, and precision distribution before the correction and after correction. It shows that with appropriate correction, the retrieved SST uncertainty and accuracy can still meet our threshold.
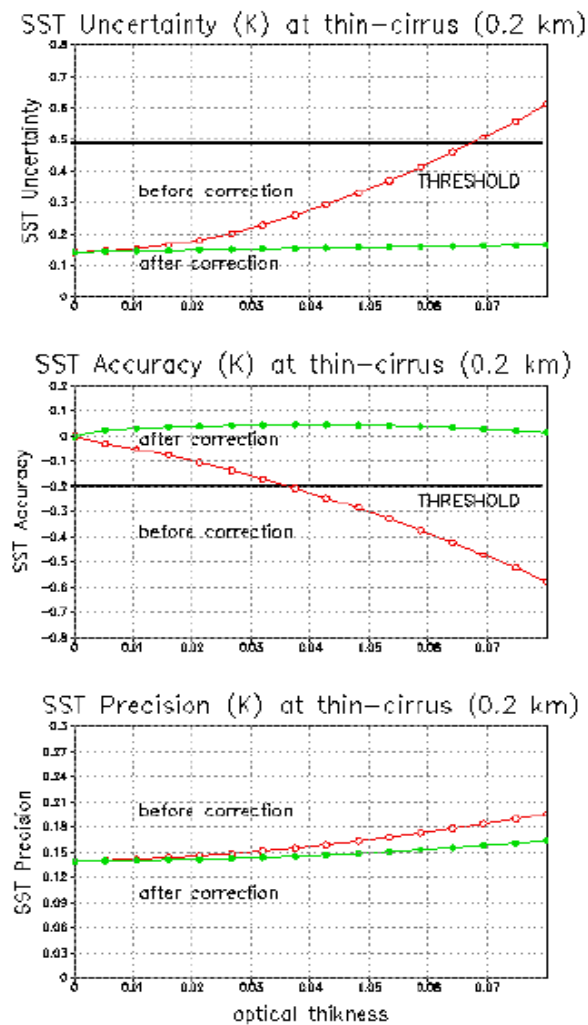
Figure 59. SST retrieval error distribution vs. cirrus optical thickness (upper panel) uncertainty, (middle) accuracy, (bottom) precision)

3.4.6   Cloud Mixed Pixels

If pixels are partly contaminated by clouds, the cloud mask algorithm may not be able to determine whether they are cloud pixels or clear pixels. Current operational SST algorithms throw away almost all pixels near the cloud to ensure retrieval accuracy. However, the space and time coverage may be reduced in this case. This section evaluates the error contribution from cloud contamination.

Figure 60 shows brightness temperatures of three VIIRS thermal bands for the Gulf Stream scene. The panels in the left column are clear scenes and in the right column are cloud scenes (50%). In this test, we assume these 50% pixels are only partly contaminated by clouds. The percentage of cloud for each of these pixels range from 0% to 10%. Over the tropics, the SST is much higher than the cloud top temperature. Therefore the cloud mask algorithm should be able to detect pixels that are highly contaminated by clouds.

Figure 61 shows the SST uncertainty, accuracy, and precision as functions of cloud percentage with these pixels. The coefficients are derived from global data. Therefore, there is bias in algorithm. The cloud contamination affects both accuracy and precision significantly. The cloud contamination contributes a cold bias to the SST retrieval. In order to meet the threshold requirements, the cloud contamination should be less than 5%.
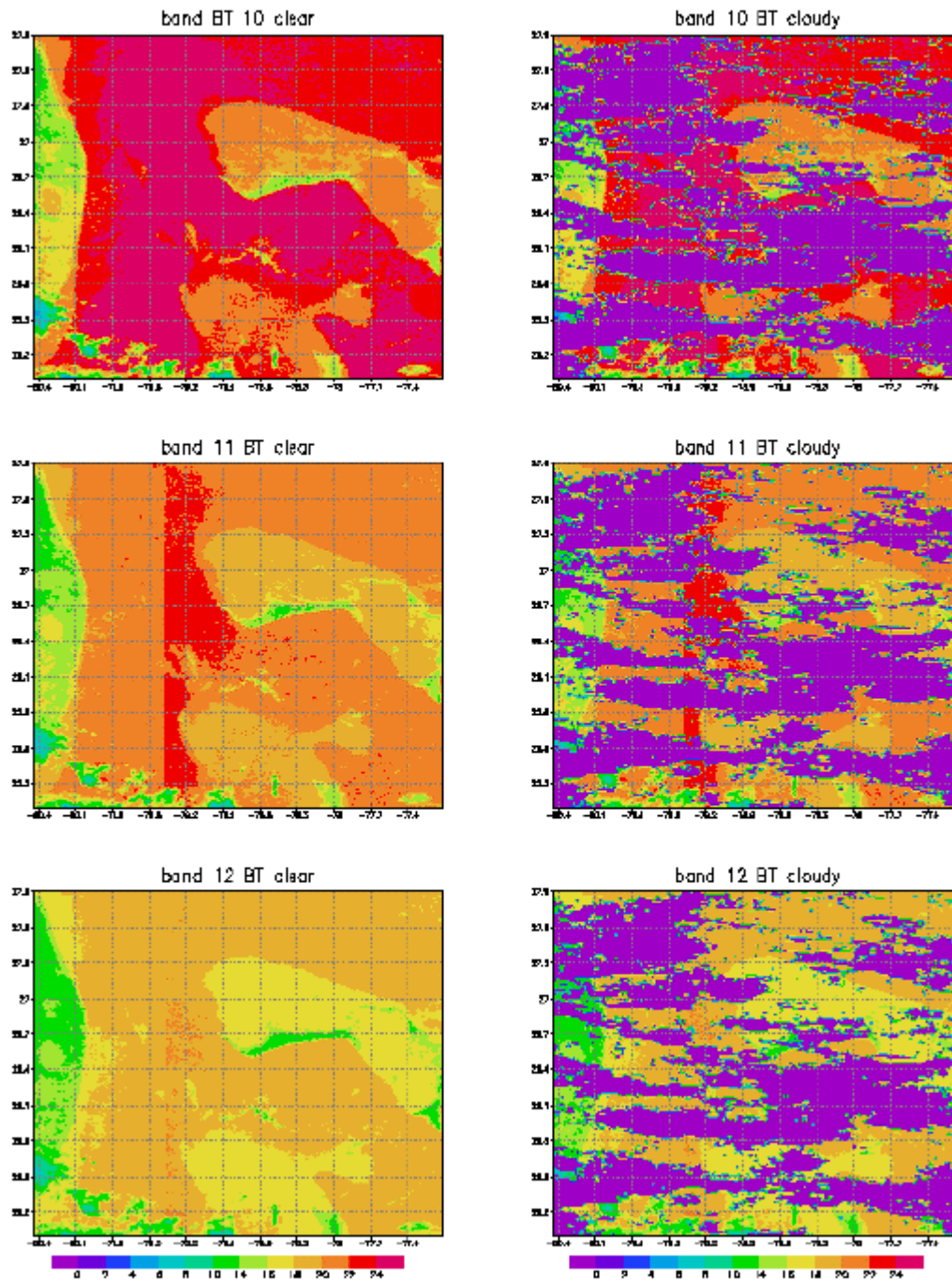
Figure 60. Nighttime brightness temperatures of three VIIRS bands under clear and cloudy conditions.
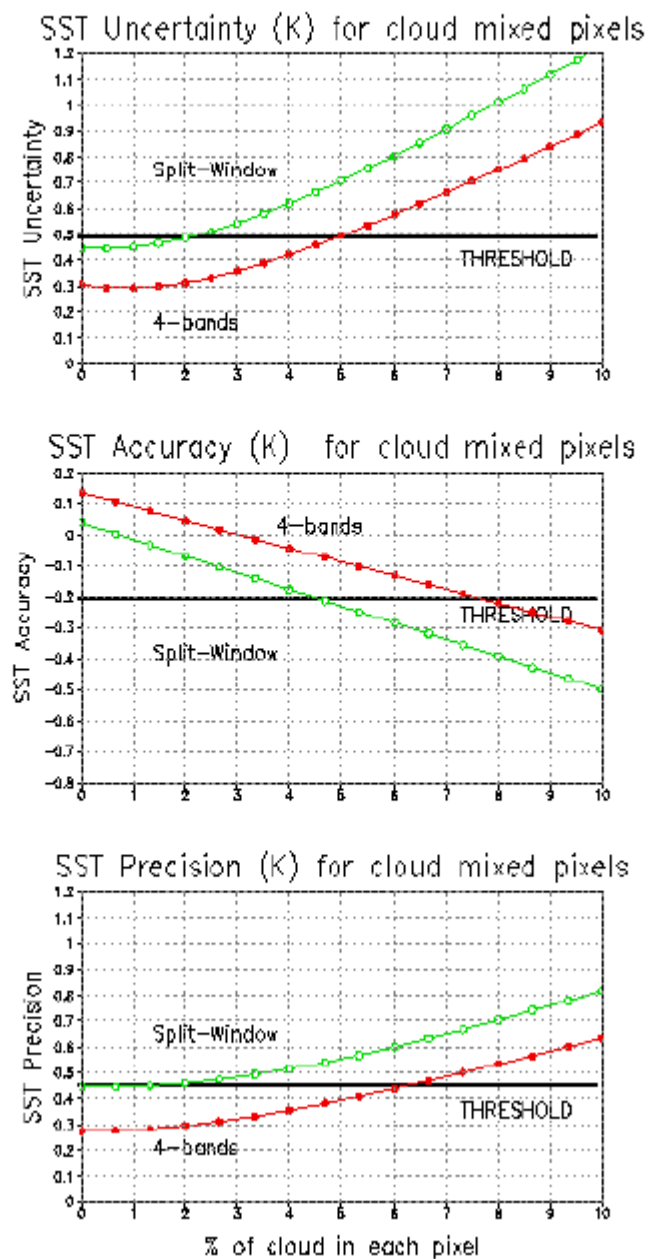
Figure 61. Uncertainty, accuracy, and precision as functions of the percentages of cloud contamination.

3.4.7 Specified and predicted performance

Figure 62 shows the specified and predicted performance from our baseline algorithm with all error sources, including aerosol correction, atmospheric correction, calibration error, sensor noise. The data is for 305 profile data with daytime simulation, the solar zenith angle is between 10 to 60 degree, viewing angle is between 0 to 45 degree. This is the toughest situation. It seems there is not big difference between specified sensor noise and predicted sensor noise. Under most cases, we can achieve 0.29 K precision CAIV target and 0.35K uncertainty objective.
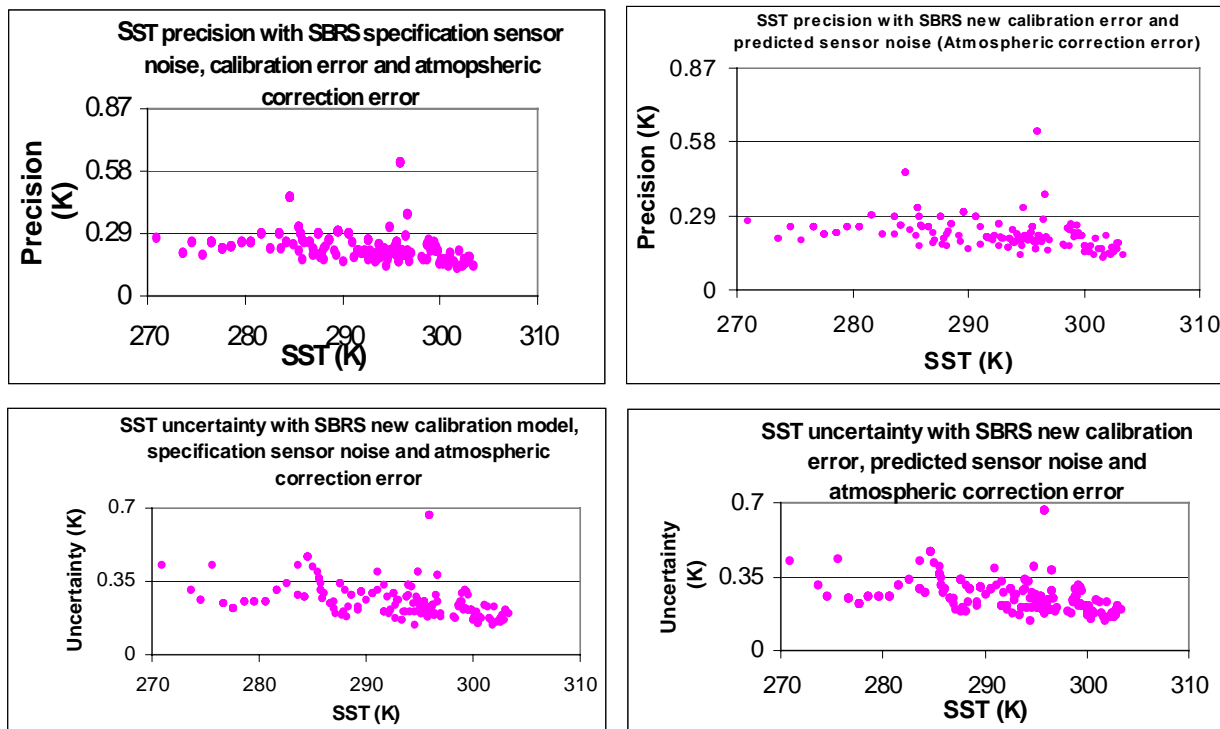
Figure 62. The total accuracy with all kind of error sources including SBRS most recent calibration perturbation, specified and predicted sensor noises. (a) Precision from the specified sensor noise, (b) Precision from the predicted sensor noise, (c) Uncertainty from the specified sensor noise, (d) Uncertainty from the predicted sensor noise.

3.5 PRACTICAL CONSIDERATIONS

3.5.1 Numerical Computation Consideration

In order to stay current, an average processing of 10,000 pixels per second must be applied. Specific aspects of the implementation include calculation of the black body temperature. A

Raytheon

counts-to-temperature look-up table will be used to speed the process. The physical retrieval method needs to run a radiative transfer model. The current method may only process a few pixels per second. In the future, the physical method will be based on a pre-calculated look-up table.

3.5.2 Programming and Procedural Considerations

Look-up tables will be used to increase the computational efficiency. Registration and re-sampling into horizontal cell size will be made after the level-2 SST processing. Parallel processing is allowed for the SST retrieval. All procedures will be automatic.

3.5.3 Configuration of Retrievals

A SST retrieval configuration is used to establish the numerical values of adjustable parameters used in the retrievals. This avoids hard-wiring specific values into the software.

3.5.4 Quality Assessment and Diagnostics

A number of parameters and indicators will be reported in the SST product as retrieval diagnostics. SST maps and statistical information will be reviewed for quality assessment. Quality flags which indicate the confidence in SST processing will be provided. They will be determined by comparing SST values from different algorithms (e.g., regression and physical retrievals, or different regression methods).

3.5.5 Exception Handling

Cloud pixels identified by the cloud mask will be skipped. Pixels with bad data will also be skipped and flagged.

3.6 ALGORITHM VALIDATION

3.6.1 Pre-Launch Validation

The atmospheric correction algorithm will be derived pre-launch by radiative transfer modeling to simulate the VIIRS infrared channel measurements. Selected radiosoundings from the operational network stations or field campaigns will be used in the VIIRS simulations for the development of the atmospheric correction algorithm. Measurements from the operational surface drifting and fixed buoy programs will be used to characterize the surface temperature fields and to validate the atmospheric correction algorithms. The assimilated meteorological fields provided by NCEP and ECMWF provide a valuable description of the marine atmosphere and surface temperature. These fields will be used in conjunction with the radiative transfer modeling to simulate the VIIRS measurements in order to validate the radiosounding data and to provide direct input to the radiative transfer modeling process.

Measurements from AVHRR and ATSR will be used in the pre-launch phase to study the error characteristics of the SST retrieval.

3.6.2 Post-Launch Calibration and Validation

It is important to recognize that the definition of sea surface temperature has changed over the years. In the days of sailing ships temperature was measured by suspending a traditional thermometer over the side of the ship. Ben Franklin used this method to map the "cold wall" of the Gulf Stream. These thermometers turned out to be fragile and the logistics of getting a good sample of the surface temperature prompted people to instead collect a sample of sea water where the temperature could be measured out on deck. Because this was typically done using some type of bucket, this became known as bucket SSTs. Care had to be exercised even in this method as metal buckets would heat with the sunshine and a thermometer touching the metal surface would give a very erroneous reading. Years later, plastic buckets were designed and built to house thermometers in a bucket with a shallow draft and a small catchment volume. These special bucket samplers became the standard for many years and are still found to give very accurate measurements of what we now call "bulk SST."

Taking bucket samples was quite satisfactory when the ships could not make more than a few knots. As the speeds of ships increased the difficulty of collecting bucket samples led to the development of other ways of sampling the SST. By far the most popular is known today as "ship injection" SST, which is a measure again of the bulk SST. In this measurement the temperature of the sea water used to cool the ship's engines was used as a measure of the bulk SST. This measurement was usually made by a sensor "injected" into the cooling water flow; hence, the name injection temperature. Because different ships had the intake for this cooling water located at different depths, it is not possible to associate a depth with the cooling water temperature. Clearly none of the intake ports was actually located at the surface and it must be acknowledged that the injection temperature is a measure of the temperature at some upper layer depth. Another problem with the injection temperature was the fact that these were located in the engine room and were therefore subject to heating by the surrounding environment. This is and was the case, and ship injection temperatures were found to be high by a few tenths of a degree.

All of the SSTs mentioned so far are measures of some temperature that is near the ocean's surface but really do not correspond to the temperature of the sea surface emitting radiation into space. The assumption must be made that the upper layer temperature is at least close to if not exactly the same as the SST. This SST measurement has become known as the "bulk SST" because it really represents something that corresponds to the temperature of the upper layer of the ocean. It is this bulk SST that has been used in the development of air-sea heat exchange formulae generally known as the "bulk formulae." It is important to recognize that this bulk temperature is not the actual SST.

In the mid 1970s it became apparent that it would be possible to use the infrared imagery from satellite radiometers to estimate SST. In spite of the existence of studies made in the 1960s and early 1970s indicating that the skin SST was actually different than the bulk SST, researchers working with satellite infrared data decided to use ship injection SSTs to "calibrate" the satellite SSTs. The satellite radiometers did improve in terms of thermal infrared calibration, but there were always problems with sensor drift and changes in the atmospheric correction leading to the need for some *in situ* data to calibrate and validate the satellite infrared SSTs. Later it became clear that the ship SSTs were too noisy to use for calibration. Drifting buoys on the other hand

Raytheon

provided a more uniform and less noisy data set, and it was decided to only use SSTs measured by drifting buoys. Another advantage of the drifting buoy SSTs was the fact that all of the buoys transmitted their data in a near real-time fashion.

Although it was clear that the buoys produced better-behaved SST data, no effort was made to determine the different effects that the buoy configuration could have on the SST. Again the SST is not measured at the sea surface; instead, thermistors protrude in the water column from the buoy hull. Also, the buoy does not float at a fixed level but instead moves up and down with the local wave field making vertical excursions of many meters. Different buoys place the thermistors at different locations and use different thermistors with differing calibrations.

As a consequence of this practice the SST that has been used for many years and is still in use today is a mixture between the skin SST measured by the infrared satellite sensor and the bulk SST measured by the drifting buoys. Because the same buoy measurements are used for validation, this approach seems to work very well. The problem is that when one looks at different times and places and compares them with an independent data set, the satellite SSTs appear to have both a bias and an RMS error. This calibration procedure error continues today primarily due to the fact that we have no alternative data available for the calibration of skin SST. What is needed is a large number of thermal infrared radiometers installed on moored buoys and ships of opportunity that routinely collect skin SST measurements. Along with these radiometric skin SSTs we need to collect a range of other supporting parameters. We need to measure the simultaneous bulk SST, which can be done with a thermistor attached to the inside of the ships's hull. In addition, it is useful to record as many of the standard parameters of the bulk fluxes such as wet-bulb temperature, air temperature, wind speed, and cloud cover.

It is important to acknowledge the present situation and define what is needed to overcome the errors introduced by "calibrating" the satellite skin SST with *in situ* measures of bulk SST. Studies have shown how this practice results in SSTs in error by 0.3 - 1.0 °C. Although it is true that errors due to atmospheric effects can overwhelm this error, it is one that is well known and easy to correct for. The atmosphere errors change considerably in both time and space, and methods are still being invented to improve on these corrections. For the skin SST the water vapor attenuation of the infrared signal is the most important effect to correct for. This can be done with coincident measurements of the total column atmospheric moisture, which can be made by passive microwave instruments.

We must distinguish between calibration and validation procedures. In the calibration process we acknowledge that the infrared sensor will drift, and that there are problems with atmospheric corrections driving us to provide for coincident *in situ* measures of the SST so that we can compute the SST algorithm coefficients by comparison to these "truth" measurements. At the present time, we do not have sufficient *in situ* skin SST measurements to calibrate the skin SST algorithm coefficients. In the future we hope to have enough data that there will be no doubt about the character of the skin SST and the associated error. At present we use "atmospheric simulations" to compute the coefficients for the skin SST algorithms. Here we use a selected set of radiosonde and a radiative transfer model to "synthesize" the skin SST as the lowest layer temperature in our model. Recent experience with these types of skin SST has demonstrated that the skin SST is too warm by a significant amount. Only *in situ* skin SST measurements will

eradicate the uncertainty of dealing with skin SST. The following validation plan is based on the fact that the future VIIRS thermal infrared channels will only measure the skin SST.

Various groups are now developing radiometer systems that can be installed on ships of opportunity or on moored buoys. These systems are being designed to operate autonomously and report by satellite, giving us a real time set of skin SST measurements. All of these buoy and ship installations will also provide us with bulk SST and most of the heat flux parameters. It is not yet clear what these instruments will cost, and this uncertainty makes it difficult to estimate the cost of operating these units. At present the best guess is that the ship-of-opportunity units will cost about $10,000, and that the buoy units will probably cost about $25,000. Research versions of these instruments run between $50,000 and $250,000 depending on the overall character of the instruments.

Because NPOESS is a global sampling platform, it is necessary to collect measurements over the entire globe. For this discussion it will be assumed that the United States must be responsible for the collection and reduction of these measurements. It may prove possible to distribute this responsibility among the various nations using data from the NPOESS system. It is easier for these other countries to maintain a measurement network located in their region. To start with, we need to select ship-of-opportunity routes that cover large parts of the ocean. Typical are the ships that travel regularly between the West Coast of the United States and Australia/New Zealand. Other ships go from the East Coast (i.e., Boston) and travel through the Panama Canal to Japan and China. In the Atlantic, there are ships that travel from Europe and the United Kingdom down to South America and the Falkland Islands. Other long shipping lines crisscross the Indian Ocean and the South Atlantic. Data from these long lines must be transferred back via satellite to be useful for the routine calibration of the satellite radiance data. This can be done either via the DCS system on NPOESS or by using geostationary weather satellites.

For NPOESS to start its own moored buoy program would be expensive and logistically difficult, and at present a number of buoys are already being operated by various Government agencies. These existing moored buoys should be the primary target of the NPOESS SST validation effort. The deployment of moored buoy skin SST radiometers should be made so as to optimize the spatial distribution of skin SST measurements. Here again, it should prove useful to work with other countries that are likely to operate their own suite of moored buoys for various reasons. It is a challenge to start a new moored buoy activity, and everything possible should be done to marry the NPOESS effort with existing projects.

We need to be very clear on the differences between calibration and validation. The former is used to correct errors in the sensor and the corrections. The assumption is that the *in situ* measurements are "correct" and that the VIIRS radiance measurement must be adjusted to fit the *in situ* data. It is important to have some idea as to how representative the *in situ* data are of the true skin SST. The validation data, on the other hand, are intended to demonstrate how well the sensor and algorithms have performed up to the specifications given for the VIIRS. It is critically important to use a different set of data for calibration and validation. That is not to say that they shouldn't be the same kind of data but that they should be different individual measurements. Thus, the calibration data can be from one period of measurements while the validation data are from a completely different period. There is some danger that longer time-scale variability will

Raytheon

influence this comparison, but this is generally not a problem. It is assumed that the data used for validation are statistically independent of the calibration measurements, which in the past was not always true with SST. It is important to have sufficient calibration measurements to have statistically significant results. There must also be sufficient validation measurements to yield usefully significant results. Unlike the calibration measurements, the validation system must operate continuously to be able to assess and update the satellite data. For this reason we propose a plan that can be continuously maintained to provide validation information over the life of NPOESS. Whether the operation of this validation network is maintained by the NPOESS operators or by an independent contractor must be decided before the system is initiated.

It is assumed that NPOESS and its instruments represent the latest in technology at the time of creation. Thus, we can expect greater precision and accuracy with all of the instruments including the VIIRS. One might think that with these greater accuracies it should be possible to reduce or perhaps eliminate the *in situ* cal/val part of the project. Experience has shown us, however, that all new instruments behave slightly differently than expected, making the need for *in situ* cal/val data even greater than it has been with previous programs. In fact, the higher accuracies of the NPOESS instruments dictate that the *in situ* measurements yield an even higher accuracy themselves in order to act as a reference for the satellite data. This means that the *in situ* measurements have to be more accurate, requiring better instruments and much greater care in their operation. Thus, the NPOESS era cal/val measurements must be considerably better than our present capabilities. Present work in infrared detectors and in instrument cooling systems suggest that these accuracies and reliabilities should be available in the next 4 or 5 years. These new capabilities should make it possible to have *in situ* reference measurements accurate to about 0.05 K.

Ship-of-opportunity measurements are based on known shipping routes where measurements of bulk SST were made using hull-mounted sensors. No sampling was done in the Indian Ocean, but there are similar shipping routes that have been used for other routine sampling operations. There are also other routes that have not been used in the past which might be used to provide a greater global sampling coverage. The important thing is to get representative *in situ* samples for calibration. This means that the *in situ* sampling must adequately cover the different zonal climate regimes and also resolve some very important east-west differences such as the surface currents of the large-scale ocean circulation.

There are a number of large buoys deployed around the U.S. to monitor weather changes constantly and assist in such operations as the shipment of oil from Alaska to the lower states. There are also buoys in the so-called TAO array marked by a rectangle around the equator. The buoys in the TAO array and other moored buoys relay their information by satellite providing realtime access to these data. Skin SST radiometers are being developed to operate autonomously from these buoys. Thus we include them in our validation sampling plan. Between now and the implementation of NPOESS, this buoy array may have changed considerably, but the expectation is that it will only increase the number of buoys deployed and operated. It is hoped that many of these buoys will operate in regions where ship-of-opportunity measurements are relatively few.

3.7   ALGORITHM DEVELOPMENT SCHEDULE

During this period, SST algorithms are mainly used to flowdown the sensor requirements. It is expected that this algorithm will be completed within 2-3 years.

4.0   ASSUMPTIONS AND LIMITATIONS

4.1   SENSOR PERFORMANCE

A major limitation of the VIIRS SST retrieval is that it can only be done under clear sky conditions. The algorithm is based on this basic assumption. Another limitation is the limitation of swath angle. As discussed in section 3.3.4, the retrieval uncertainty becomes much larger at swath angles larger than 40°. The swath width used for SST retrieval will be only 1,700 km (half of the orbit). Therefore, the 6-hourly SST data can only be obtained for some particular regions. The weekly global coverage will be obtained by merging VIIRS SST and global analyses.

4.2   SKIN AND BULK SST

Most of this document discusses the skin SSTs. However, the validation of skin SST retrieval will be a big challenge since the available *in situ* observations are bulk SSTs. We assume that we will be able to obtain skin temperatures from ship measurements, such as boat-mounted infrared radiometer measurements (Barton, 1985). The bulk-skin temperature difference is subject to both net surface heat flux and the momentum flux (Saunders, 1967). A number of equations have been used to find the bulk-skin temperature difference (e.g., Hasse, 1971, Schluessel *et al.*, 1990). For example, Schluessel *et al.* used following equations to find the ΔT:

Nighttime:

$$\Delta T = a_0 + a_1 u(T_s - T_a) + a_2 u(Q_s - Q_a) + a_3 L \tag{28}$$

Daytime:

$$\Delta T = a_0 + a_1 S / u + a_2(Q_s - Q_a) + a_3 L \tag{29}$$

where, T_s and T_a are temperatures of surface and air, Q_s and Q_a are water vapor mixing ratios of surface and air, L is the net longwave radiative flux, S the net solar radiative flux, and u the mean wind velocity.

The ΔT can be predicted to an accuracy of approximately 0.2 K provided there are known atmospheric properties. Figure 63 shows the bulk-skin difference from preliminary calculation using NCEP assimilated data. The bulk-skin differences are smaller than 2 K over the region.
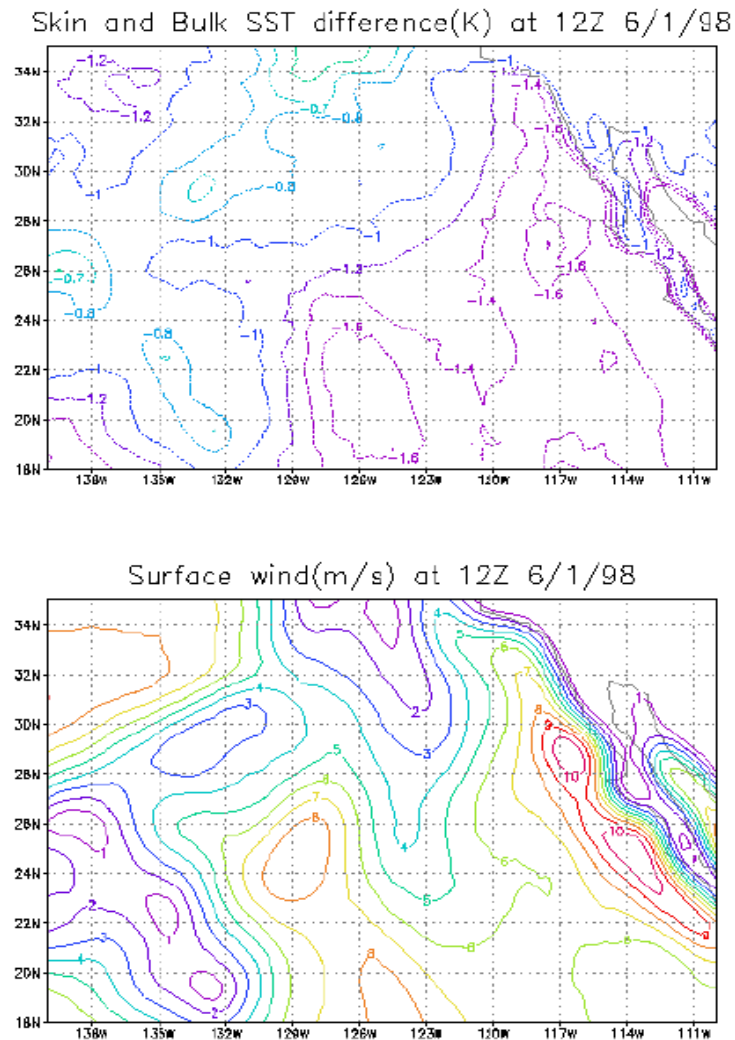
**Figure 63. Bulk-skin SST difference (upper panel),
and the surface wind field at the same time (lower panel).**

5.0 REFERENCES

Barton, I. J. (1985). Transmission model and ground truth investigation of satellite-derived sea surface temperatures. *J. of Clim and Appl. Meteo*., 24, 508-516.

Barton, I. J., A. J. Prata, and D. T. Llewellyn-Jones (1993). The Along Track Scanning Radiometer – an Analysis of coincident ship and satellite measurements. *Adv. Space Res*., 13, 69.

Berk, A., L. S. Bemstein, and D. C. Robertson (1989). MODTRAN: A moderate resolution model for LOWTRAN 7, Rep. GLTR-89-0122. Burlington, MA: Spectral Sciences, Inc.

Brown, O. B., and P. J. Monnett (1996). MODIS Infrared Sea Surface Temperature ATBD.

Cornette, W. M., P. K. Acharya, D. C. Robertson, and G. P. Anderson (1994). Moderate spectral atmospheric radiance and transmittance code (MODSART), Rep. R-057-94 (11-30). La Jolla, CA: Photon Research Associates, Inc.

Emery, W. J., Y. Yu, G. A. Wick, P. Schluessel, and R. W. Reynolds (1994). Correcting infrared satellite estimates of sea surface temperature for atmospheric water vapor attenuation. *J. Geophys. Res*., 99, 5219-5236.

Griggs, M. (1985), A method to correct satellite measurements of sea surface temperature for the effects of atmospheric aerosols. *J. Geophys. Res*., 90, 12951-12959.

Hasse, L. (1971). The sea surface temperature derivation and the heat flow at the sea-air interface. *Boundary Layer Meteor*., 1, 368-379

Ji, Y., and A. D. Vernekar (1997). Simulation of the Asian summer monsoon of 1987 and 1988 with a regional model nested in a global GCM. *J. Climate*, 10, 1965-1979.

Kalnay, E., M. Kanamitsu, R. Kistler, W. Collins, D. Deaven, L. Gandin, M. Iredell, S. Saha, G. White, J. Woollen, Y. Zhu, M. Chelliah, W. Ebisuzaki, W. Higgins, J. Janowiak, K. C. Mo, C. Ropelewski, J. Wang, A. Leetmaa, R. Reynolds, R. Jenne, and D. Joseph, 1996: The NMC/NCAR 40-Year Reanalysis Project". *Bull. Amer. Meteor. Soc.*, 77, 437-471.

Kneizys, F. X., E. P. Shettle, L. W. Abreu, J. H. Chetwynd, G. P. Anderson, W. O. Gallery, J. E. A. Selby, and S. A. Clough (1988). Users Guide to LOWTRAN 7, Rep. AFGL-TR-88-0177. Bedford, MA: Air Force Geophys. Lab.

Legeckis, R., and T. Zhu (1997). Sea surface temperature from the GEOS-8 geostationary satellite. *Bull. Amer. Meteor*. Soc., 78, 1971-1983.

May, D. A., L. L. Stowe, J. D. Hawkins, and E. P. McClain (1992), A correction for Saharan dut effects on satellite sea surface temperature measurements. *J. Geophys. Res*., 97, 3611-3619.

May, D. A., M. M. Parmeter, D. S. Olszewski, and B. D. Mckenzie (1998). Operational processing of satellite sea surface temperature retrievals at the Naval Oceanographic Office. *Bull. Amer. Meteor. Soc*., 79, 397-407.

McClain. E. P., W. Pichel, and C. Walton (1985). Comparative performance of AVHRR-based multichannel sea surface temperature. *J. Geophys. Res*., 89, 11587-11601.

McClain, E. P., W. G. Pichel, C. C. Walton, Z. Ahmed, and J. Sutton (1983). Multi-channel improvements to satellite derived global sea surface temperatures. Proc. XXIV COSPAR, *Advances Apace Res*., 2(6), 43-47.

McClain, E. P. (1995). Global sea surface temperature and cloud clearing for aerosol optical depth estimates. *Int. J. Remote Sensing*, 10, 763-769.

McMillin, L., and D. Crosby (1984). Theory and validation of the multiple window sea surface temperature technique. *J. Geophys. Res*., 89, 3655-3661.

Minnett, P. J. (1990). The regional optimization of infrared measurements of sea-surface temperature from space. *J. Geophys. Res*., 95, 13497-13510.

Reynolds, R. W. (1988). A real-time global sea surface temperature analysis. *J. Climate*, 1, 75-86.

Reynolds, R. W., and T. Smith (1994). Improved global sea surface temperature analysis using optimum interpolation. *J. Climate*, 7, 929-948.

Saunders, P. (1967). The temperature at the ocean-air interface. *J. Atmos. Sci*., 24, 269-273.

Schluessel, P., W. J. Emery, H. Grassl, and T. Mammen (1990). On the bulk-skin temperature differences and its impact on satellite remote sensing of sea surface temperatures. *J.*

Raytheon